TECHNISCHE UNIVERSITÄT DARMSTADT

Karlsruher Institut für Technologie

Waveguide-Integrated Electrically Driven Light-Emitting Carbon Nanotubes

by

Felix Pyatkov

Dissertation

Approved in Fulfillment of the Requirements

for the Degree of

Doctor of Natural Sciences

Department of Material and Geosciences

Technical University of Darmstadt

Waveguide-Integrated Electrically Driven Light-Emitting Carbon Nanotubes

DISSERTATION

Approved by the Department of Material and Geosciences, TU Darmstadt

In fulfillment of the requirements for the degree of Doctor of Natural Sciences

By M.Sc. Felix Pyatkov from Lipetsk, Russia

Supervisor: Prof. Dr. Ralph Krupke

Co-supervisor: Prof. Dr. Wolfram H. P. Pernice

Examiner: Prof. Dr. Wolfram Jaegermann

Examiner: Prof. Dr. Wolfgang Ensinger

Date of submission: 30. 08. 2016

Date of disputation: 07. 11. 2016

Darmstadt 2017 – D17

Ehrenwörtliche Erklärung

Gemäß § 9 der Promotionsordnung zur Erlangung des akademischen Grades eines Doktors der Naturwissenschaften (Dr. rer. nat.) der Technischen Universität Darmstadt.

Hiermit erkläre ich, dass ich die beigefügte Dissertation selbstständig verfasst und keine anderen als die angegebenen Hilfsmittel genutzt habe. Alle wörtlich oder inhaltlich übernommenen Stellen habe ich als solche gekennzeichnet.

Ich versichere außerdem, dass ich die beigefügte Dissertation nur in diesem und keinem anderen Promotionsverfahren eingereicht habe und, dass diesem Promotionsverfahren keine endgültig gescheiterten Promotionsverfahren vorausgegangen sind.

Abstract

In this work proof-of-concept devices with light-emitting electrically driven carbon nanotubes (CNTs) integrated in nanophotonic environments are presented.

Electroluminescent and incandescent CNTs can be envisioned as waveguide-integrated light sources for future on-chip data communication due to their unique structural, electrical and optical properties. The challenge thereby is to integrate and electrically contact solution processed CNTs across CMOS compatible waveguide structures and to enforce efficient coupling of light from the CNT into the waveguide.

Various nanophotonic devices with versatile functionalities were fabricated and equipped with CNTs by means of site-selective dielectrophoresis. The realized electrically driven CNT-based light emitters integrated with nanophotonic circuits allow for efficient coupling and propagation of light in waveguides over centimeter distances. Furthermore, in scope of the thesis it was demonstrated how spectral properties of a CNT emitter can be controlled directly on a chip with passive devices using grating structures, Mach-Zehnder interferometers and directional couplers. Moreover, it was observed that in combination with a one-dimensional photonic crystal cavity CNT becomes an emitter with exceptionally narrow linewidths at desired adjustable wavelength. Finally, the usage of electrically driven CNTs as fast waveguide-integrated light emitters with Gbit/s response speed was shown.

Therefore direct, near-field coupling of electrically generated CNT-emitted light into a waveguide, opposed to far-field fiber coupling of external light sources, opens new avenues for scalable nanoscale optoelectronic systems in a CMOS compatible framework.

Zusammenfassung

Im Rahmen dieser Arbeit wird eine Machbarkeitsstudie zu licht-erzeugenden, elektrisch betriebenen und in eine nanophotonische Umgebung integrierten Kohlenstoffnanoröhren (CNTs) vorgestellt.

CNTs weisen einzigartige strukturelle, elektrische und optische Eigenschaften auf und sind somit als Wellenleiter-integrierbare CMOS-kompatible elektrolumineszente und thermische Lichtquellen von großem Interesse für zukünftige On-Chip Datenkommunikation. Die Herausforderung besteht dabei in der gezielten Integration und der elektrischen Kontaktierung von zuvor suspendierten CNTs über die Wellenleiterstrukturen, sowie in der Gewährleistung einer effizienten Lichteinkopplung in einen optischen Wellenleiter.

Eine Vielfalt von nanophotonischen Bauteilen mit diversen Funktionen wurde entwickelt und hergestellt. Dielektrophorese wurde für die skalierbare ortsselektive Integration von CNTs in optische Schaltkreise eingesetzt. CNT-basierten Lichtquellen demonstrierten eine effiziente Einkopplung und Ausbreitung von emittiertem Licht in Wellenleiter über Zentimeter-Entfernungen. Die spektralen Eigenschaften des Lichts im Wellenleiter wurden durch passive Bauteile wie Gitterkoppler, Richtkoppler sowie Mach-Zehnder Interferometer kontrolliert. Insbesondere wurde die CNT in Kombination mit einem eindimensionalen Wellenleiter-basierten Resonator zu einem besonders schmalbandigen Emitter bei einer gewünschten Wellenlänge. Darüber hinaus ließen sich die elektrisch betriebenen CNT-Lichtquellen im Gigahertz-Frequenzbereich modulieren.

Somit bietet die Nahfeldkopplung des elektrisch generierten von CNTs emittierten Lichts in den Wellenleiter eine aussichtsreiche Alternative zur Faserkopplung mit externen Lichtquellen. Neue Wege für die Herstellung von skalierbaren optoelektronischen CMOS-kompatiblen Nanosystemen werden dadurch eröffnet.

Contents

1. Introduction

The „who owns the information, he owns the world“ old maxim was never so true as in our „Information Age“. The amount of data is rapidly growing, and thus one of the ultimate goals of engineering and science is optimization of information transfer. While the wired communication was predominated by the electrical transmission in the 20th century, the leading technology nowadays is the fiber-optics communication. Thanks to much higher bandwidth and exceptionally low losses (1), fibers supersede electrical wires in long-distance communication. Also for short-distance applications at chip-to-chip or on-chip levels higher transfer rates and novel capabilities can be realized by replacement of electrical interconnects by optical waveguides (2). Currently, light is injected into waveguided structures mainly by means of fiber-coupling techniques (3,4) in combination with external sources (5–7). Alternatively, scalable integration of light emitters in otherwise passive nanophotonic circuits enables realization of active wafer-scale optical modules for data transfer with economy of scale and versatile functionalities. Carbon nanotubes (CNTs) exhibit a direct structure-dependent bandgap and exceptionally high thermal conductivity (8), which confer them a great potential for future active photonic devices. In combination with a well-established quick and low-cost dielectrophoretic deposition (9), CNTs emerge as a promising candidate for a scalable waveguide-integrated on-chip light source.

In this thesis the light emitting properties of electrically driven CNTs and their integration in nanophotonic environment were investigated. The design of the CNT-based emitters shown here provides a scalable, wavelength-controlled implementation for the realization of photonic networks on chip where light is generated locally and distributed across the circuits via low-loss optical waveguides.

The presented work was performed in close collaboration with research group „Integrated Quantum-Optics and Optomechanics“ of Prof. Dr. W. H. P. Pernice, S. Khasminskaya, R. G. Fechner, and V. Fütterling.

The remainder of the thesis is organized as follows.

Chapter 2 summarizes the theoretical background of the thesis in context of the subsequent Chapter. CNTs are introduced and their optoelectronic properties are shortly described. Finally, integration of CNTs in nanophotonic environments is discussed.

Chapter 3 demonstrates electrically driven waveguide-integrated light emitting CNT-based devices. First, the concept of the structure, following by the description of fabrication process and measurement techniques are provided. Then device performance, coupling efficiency and propagation losses are discussed (10). Afterwards, the following CNT-based light emitting structures with different functionalities are considered:

- Mach-Zehnder interferometer (10)
- Directional coupler (11)
- Photonic crystal beam cavity with adjustable narrow-line bandwidth (12)
- High-speed light emitter with repetition time up to 2 GHz (13)

Finally, in **Chapter 4**, ongoing research projects including CNT-based emitters operating in telecommunication wavelength range (14) as well as in single photon emission regime (15) are presented, the work done in the thesis is summarized and an overview of the future research directions is provided.

2. Theory

2.1 Carbon-Based Nanostructures

In the big world of nanostructures carbon-based materials take a prominent place due to the almost unique variety of forms and properties. Alone their morphology ranges from 3D-structures (graphite and diamond) over two-dimensional graphene and one-dimensional CNTs to zero-dimensional fullerenes. Accordingly strongly vary the mechanical, optical and electrical properties (8), achieving in some cases exceptional high values that makes carbon-based structures a desirable research object for both fundamental and applied sciences.

The discovery of CNTs was reported a quarter of century ago by S. Iijima (16). Single-walled CNTs (SWCNTs) are cylinder-shaped nanostructures and can be visualized as a rolled graphene sheet. As depicted in Figure 2.1a, the honeycomb lattice of graphene with the lattice vector $a = 0.246\ nm$ can be wrapped in different ways along the chiral vector $\overrightarrow{C_h} = n\overrightarrow{a_1} + m\overrightarrow{a_2}$ with translational vectors $a_{1,2}$. The unambiguously description of CNT structure is given by chiral indices (n, m) that determine type and diameter of nanotube:

$$d_{CNT} = \frac{|\overrightarrow{C_h}|}{\pi} = \frac{0.246\ nm}{\pi}\sqrt{n^2 + nm + m^2} \qquad (2.1)$$

With d_{CNT} of about 1 nm and an arbitrary length, which can exceed 0.5 m but typically is in the range of 1 µm, SWCNTs have the largest length-to-diameter ratio among all known materials.

There are three geometrical classes of SWCNTs, shown in Figure 2.1b. (n, n)-armchair and $(n, 0)$-zigzag SWCNTs were named so because of the corresponding pattern that carbon atoms form along the circumference, other SWCNTs with $n \neq m \neq 0$ are called chiral. As described in the next section in more detail, one third of SWCNTs that fulfill the requirement $(n - m) = 3i,\ i \in Z$ demonstrates metallic properties (MeCNTs), while all other SWCNTs are semiconducting (SCCNT).

SWCNTs typically have very low defect density and high chemical purity, so that their properties can be well described with theoretical models.

It should be mentioned that the variety of CNT materials is not restricted to the cases shown in Figure 2.1. These are just the most common ones. Besides of SWCNTs there are double-walled (DWCNT) and multi-walled CNTs, consisting of multiple coaxially aligned rolled layers of graphene (Russian Doll model). An important feature of DWCNTs is a small chemical reactivity of the inner CNT that is shielded from the environmental influences by the outer CNT. In a similar way CNT can serve as container for molecules, nanoribbons, dyes or fullerenes filled inside the tube (17). By introducing of defects or doping a functionalization of CNTs can be achieved that allow for tuning not only their chemical reactivity, but also mechanical, thermal, optical and transport properties (8,18,19).

However, SWCNTs are by far the best investigated type of CNTs, since the controllable synthesis, sorting and characterization of multi-walled CNTs is much more problematic. This work is focused on the properties of undoped SWCNT, hereafter referred to as just CNTs.

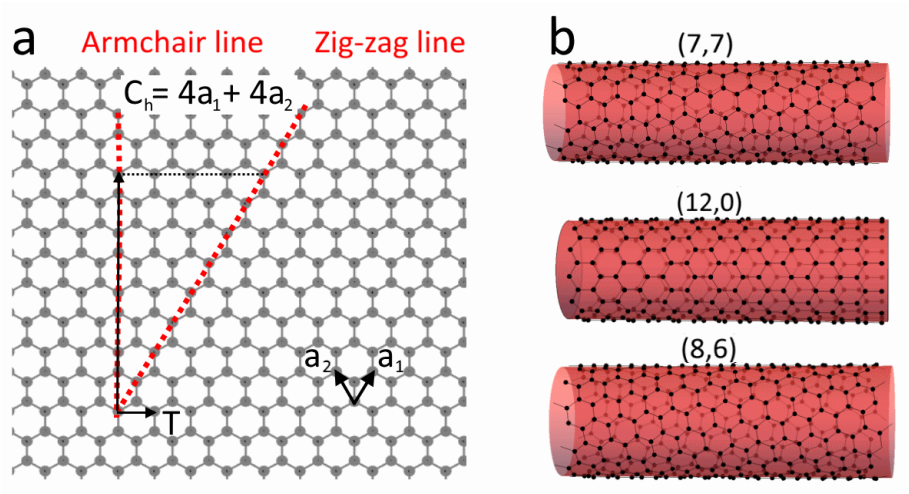

Figure 2.1 | Structure of SWCNT.

(a) Illustration of folding of a (4,4)-SWCNT from a graphene layer. $a_{1,2}$ are the unit vectors of the graphene cell. The SWCNT unit cell is spanned by the transition vector T (tube axis) and the chiral vector C_h.
(b) Atomic structure of (7,7)-armchair, (12,0)-zigzag and (8,6)-chiral SWCNTs.
Plotted using (20).

There are three well-established categories of methods for CNT synthesis (8) including arc discharge between carbon electrodes, laser ablation of carbon target and chemical vapor deposition (CVD):

- In the first case, high electrical current between two carbon electrodes in the presence of metal catalysts generates carbon plasma that induces synthesis of short, low-defect CNTs with larger diameter, deposited on cathode (21). It was the first method developed for CNT synthesis.
- Alternatively, CNTs can be synthesized due to the vaporization of graphite rod under intense laser pulses (22). The CNTs produced in this way demonstrate low number of defects and impurities and narrow diameter distribution, but often form bundles.
- Lastly, CVD-based techniques involve continuous flow of some carbon-containing gas and some process gas over the heated substrate with metal catalysts nanoparticles (23). CNTs nucleate and grow on the catalyst clusters. With relatively high yield and low costs, CVD is the most widely used technique for CNT synthesis. The chirality and diameter distribution can be influenced by the reaction parameters. There are several CVD-based approaches for large-scale and chirality-selected synthesis of CNTs, such as HiPco (High Pressure disproportionation of carbon monoxide CO), CoMoCat (Cobald Molybdenum Catalyst) and PECVD (plasma-enhanced CVD) methods. The HiPco process yields the highest amount of CNTs that typically have significantly smaller diameter than those produced using other approaches. CoMoCat-CNTs have narrow chirality and diameter distribution, while PECVD technique promises a structure-specific CNT synthesis with 95% selectivity (24). An important advantage of CVD-approach is the controlled growth of CNTs with ordered structure on substrate that is not possible with other methods. CVD-grown well-separated individual CNTs can be directly used for fabrication of integrated electronic and photonic circuits.

All synthesis techniques require high temperatures in the range of 700 °C to 1700 °C and yield a mixture of CNTs with different chiralities.

Quality and purity of CNT materials are essential for the development of CNT-based applications. Suspensions with minimal amount of MeCNTs are required for the large-

scale fabrication of CNT-based transistors, while for the production of solar cells monochiral CNT networks are desirable. There are a number of post-synthetic techniques including chromatographic, electrophoretic, fluid-based and chemical methods (25) used for the purification, filtration, separation and sorting of CNTs. Differences in geometry (26) and oxidation reaction (27) between CNTs and impurities are employed to remove catalytic and amorphous particles, sonication helps to untangle CNT bundles. Furthermore, SCCNTs can be separated by length, metallicity and chirality using polymer wrapping (polyfluorene assisted ultra-centrifugation, PFO (28)) and structure discriminating surfactant (density gradient ultracentrifugation, DGU (29) and gel permeation chromatography (30)). These techniques are based on the different buoyant densities of CNTs and on the structure-dependent interaction strength of CNTs with the gel in the latter case. PFO-assisted sorting technique utilizes (n,m)-specific wrapping of polymers around a nanotube. Similarly, CNT encapsulation inside surfactants leads to the change of nanotube density and therefore to the diameter-specific or electronic-specific sorting. As a result, CNTs can be separated in fractions with different properties. In particular, PFO-assisted sorting provides suspensions with less than 0.3% of MeCNTs (31), while using gel permeation chromatography monochiral suspensions with over 95% selectivity can be prepared (30). It is important to mention that even a few per mill of remaining impurities and residual MeCNTs may strongly reduce the luminescence and transport properties of CNT network.

In the following, electronic and optical properties of CNTs are discussed in detail.

2.2 Electronic Properties of CNTs

The CNT band structure can be described based on the electronic structure of grapheme (32). Each carbon atom has 4 electrons in the outer shell. Three of them form σ bonds to neighbor atoms in the honeycomb lattice, as shown in Figure 2.1a. The last p_z electron remains free and forms π bond perpendicular to the graphene surface. p_z orbitals overlap each other and help to enhance the carbon to carbon bonds. Since σ bonds are too far away from the Fermi level, only π bonds significantly influence the electronic transport and optical absorption in graphene and CNTs. Under assumption that atomic wave functions are well localized at the atomic positions, the electronic structure of graphene can be modeled using first-order tight-bindiing approximation as linear combination of p_z orbitals. It follows the dispersion relation:

$$E(k_x, k_y) = \pm\gamma_0\sqrt{1 + 4\cos\left(\frac{\sqrt{3}ak_y}{2}\right)\cos\left(\frac{ak_x}{2}\right) + 4\cos^2\left(\frac{ak_x}{2}\right)} \qquad (2.2)$$

with the wave vectors $\vec{k}$ and tight-binding integral γ_0 for the carbon-carbon interaction energy (32). The π band structure of graphene is shown in Figure 2.2a. The valence and conductance bands are connected at the K-point ($^1/_3\,\vec{k}_x$ / $-\,^1/_3\,\vec{k}_y$). This gives graphene its semi-metallic behavior.

According to the zone-folding approximation, the electronic band structure of CNT is given by the graphene electronic energies E along the allowed k lines. Considering the tube geometry, $\overrightarrow{k_{\parallel}}$ along the CNT axis are continuous, while $\overrightarrow{k_{\perp}}$ around the circumference are quantized and can have only discrete values. Therefore, the allowed electronic states are restricted to wave vectors that fulfill the Bloch condition (33) $\overrightarrow{k}\cdot\overrightarrow{C_h} = 2\pi i,\ i \in Z$. CNT is metallic if K-point belongs to the allowed states, namely in the case $(n - m) = 3i$. According to that two thirds of CNTs are semiconducting. The wave vectors for a MeCNT and SCCNT are shown as black lines in Figure 2.2a.

Electronic density of states (DOS) can be calculated for MeCNT and CNT based on the energy dispersion relation, shown in Figure 2.2b. The spikes in the DOS are known as van Hove singularities, resulting from the confinement along the circumference of a CNT. In contrast to MeCNTs, SCCNTs have the chirality-dependent energy gap between the pair of van Hove singularities closest to Fermi level.

Transport and optical properties of CNTs are intimately related to their electronic band structure. Both metallic and semiconducting CNTs could be a promising alternative to the traditional semiconductor electronics. While low-ohmic MeCNTs can serve as interconnects, SCCNTs are more interesting as transistors and light sources because of their chirality-dependent bandgap. In response to optical or electrical stimulation semiconducting CNTs act as photoluminescent (PL) or electroluminescent (EL) emitters, as discussed in the following section.

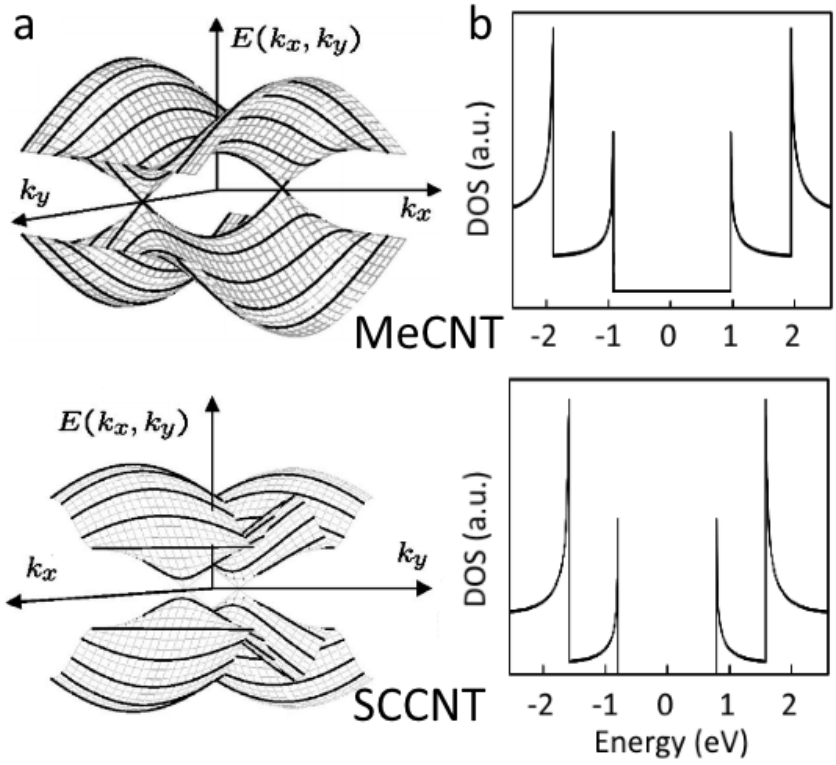

Figure 2.2 | Electronic properties of CNTs.

(a) Dispersion relation for the graphene plane together with that of an armchair MeCNT (top image, bold line) and zigzag SCCNTs (bottom image). Adapted with permission from (33).
(b) Density of states for a MeCNT and a SCCNT.

2.3 Optical Properties of CNTs

2.3.1 Photoluminescence

In the first approximation, optical properties of CNTs can be described with the help of the tight-binding model discussed in the previous section. Density of states diagram in Figure 2.3a illustrates PL process in SCCNT. Optical transitions mainly occur between valence and conductive subbands of the same indices $v_i - c_i$ and are labeled as E_{ii}. These transitions are allowed for the light polarized along the CNT axis. Crossover transitions E_{ij} with $i \neq j$ are very weak, since they require the light polarized perpendicular to the tube axis, and in this case the incident excitation is screened by charges on the CNT wall. In PL experiment light is absorbed by the E_{22}-transition, followed by fast relaxation and luminescent emission from the E_{11}-transition.

However, according to the tight-binding model, for large diameter CNTs $\frac{E_{22}}{E_{11}} \approx 2$ is expected (see Figure 2.3a), in contrast to the experimental results with $\frac{E_{22}}{E_{11}} \approx 1.8$ (34). This so-called ratio problem was solved using *ab initio* many-electron Green's function approach (35) by taking into account electron-electron and electron-hole interactions. Both contributions partially compensate each other, resulting in a shift (Figure 2.3b) and a broadening of van Hove singularities in the density of states diagram. In one-dimensional nanotubes both the dielectric screening and the average distances between the charge carriers are reduced, so that the optically produced electron-hole pairs are strongly bounded by electrostatic Coulomb force. These bound states are called excitons. With binding energies $E_b \sim \frac{1}{d_{CNT}}$ of hundreds of meV, excitons are stable even at room temperature. Formation and annihilation of excitons lead to Lorentzian-shaped maxima in absorption and PL spectra of CNTs. Besides of excitons there are also trions (charged excitons (36)) that appear 100 to 200 meV below corresponding excitonic transitions (E_{11}, E_{22} ...) preferentially in PL spectra of chemically or electrostatically doped SCCNTs.

Excitonic transitions are structure-dependent and rather sharp that makes possible optical detection and identifying of CNTs using absorption spectroscopy (37), photoluminescence (34,38) and Raman spectroscopy (39). The relation between

diameter and energy gap of different SCCNT species was summarized by H. Kataura (37). For a (n,m)-assignment typically an empirical Kataura plot is used (40). As shown in Figure 2.3b, the energy of electronic transitions decreases with the increase of CNT diameter $E_{ii} \sim \frac{1}{d_{CNT}}$. PL measurements provide information about excitation E_{22} and emission energies E_{11} for every SCCNT-species, and therefore allow for unambiguous and fast chirality identification. In contrast, MeCNTs are not accessible for the PL characterization due to the missing bandgap. The inset of Figure 2.3b exemplarily shows a PL map of a SCCNT suspension with the assigned emission spots (41).

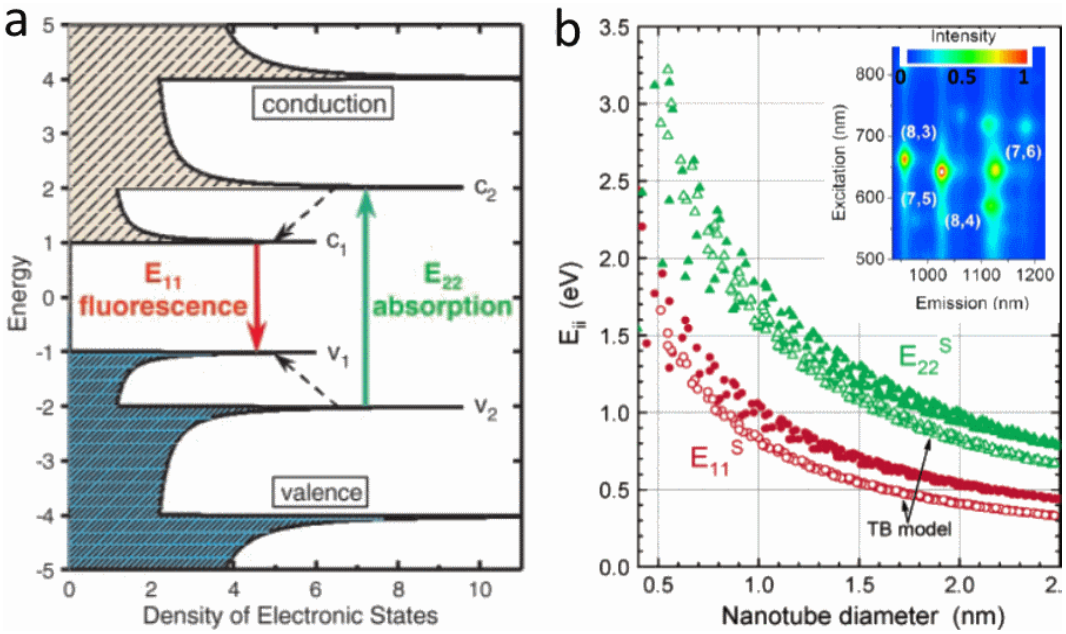

Figure 2.3 | Photoluminescence of CNTs.

(a) Schematic density of states for a SCCNT according to the tight-binding approximation. Optical transitions between van Hove singularities are depicted with green (absorption) and red (fluorescence) arrows. Dashed arrows illustrate the relaxation of the electron and the hole in the conduction and valence band before emission, respectively (34).

(b) Kataura plot. Comparison between tight-binding model and empirical values of $E_{ii} \sim \frac{1}{d_{CNT}}$ (40).

Inset: Photoluminescence contour map of a multichiral SCCNT suspension (41).

Adapted with permission from (34,40,41).

PL measurements can be also performed on SCCNT films and single tubes. Both intensity and efficiency of PL strongly depend on the defect density, nanotube length (42,43), temperature (44) and sample surface (45). The intensity is significantly higher in the case of suspended SCCNTs, since the direct interaction with the substrate typically quenches emission (46).

2.3.2 Electroluminescence and Incandescence

Similarly to PL, SCCNT can emit luminescent light in response to electrical excitation (47). EL measurements are typically performed in a field-effect transistor (FET) configuration where electrically contacted SCCNTs are grown or deposited on insulating substrates with capacitively coupled gate (47). As discussed below, EL in ambipolar FETs involves carrier recombination, while in unipolar FETs impact excitation is considered as the dominant emission mechanism.

In an ambipolar FET electrons and holes are injected from opposite contacts and radiatively recombine in a SCCNT. This process is depicted in Figure 2.4a. The efficiency of the carrier recombination is maximal, if the electron and hole currents are equal. For symmetrical contacts this requirement is fulfilled at $V_G = 0.5\, V_{SD}$ (48). The typical quantum yield of EL $\eta_{EL} = 10^{-7} \dots 10^{-6} \frac{photon}{e^- - hole\ pair}$ is relatively low, the emission is more efficient in the case of longer CNTs (49). Higher η_{EL} of up to 10^{-4} were measured on the devices with asymmetric contacts that form p-n-junctions (50). Alternatively, split gate device geometry allows for modification of SCCNT band profile and relatively strong EL emission (51,52).

EL can be also observed in unipolar FETs operating at higher source-drain voltages (53,54). In this case, energetic “hot” carriers generate electron-hole pairs that radiatively relax, as schematically shown in Figure 2.4b. The emission occurs at defects or such inhomogeneities as Schottky or CNT-CNT contacts, where the local electric fields are large enough to accelerate the carriers for exciton generation. With $\eta_{EL} = 10^{-5} \dots 10^{-3}$ the impact excitation can be even more efficient than carrier recombination process. However, electroluminescent devices of both types demonstrate significantly lower efficiency in comparison to photoluminescent emission with $\eta_{PL} = 10^{-2} \dots 10^{-1}$ (55,56). Considering the theoretical limit for efficiency of luminescence of 15-20% (57), there is a scope for optimization that could be achieved

both in fabrication and operation of EL-devices.

By comparison between PL- and EL-based applications, one important aspect is the efficiency of the device itself. While PL has higher quantum yield, its significant drawback is the law fraction of photons absorbed by CNT due to the small absorption cross section. In fact, a suspended CNT absorbs less than 1% of photons (55) that makes less effective EL process quite compatible with PL.

EL measurements demonstrate many fundamental similarities with PL experiments. In the both cases the emission maxima occur at similar energies close to E_{11} and E_{22} although PL emission is typically more narrow-line (58). Due to the one-dimensionality of CNTs, both PL (59) and EL (48) are polarized along the tube axis. Trionic emission, first measured in PL, was recently observed also in EL spectra of CNT films (60,61). Electrostatic doping can be used for switching and control over PL and EL emission intensity (62).

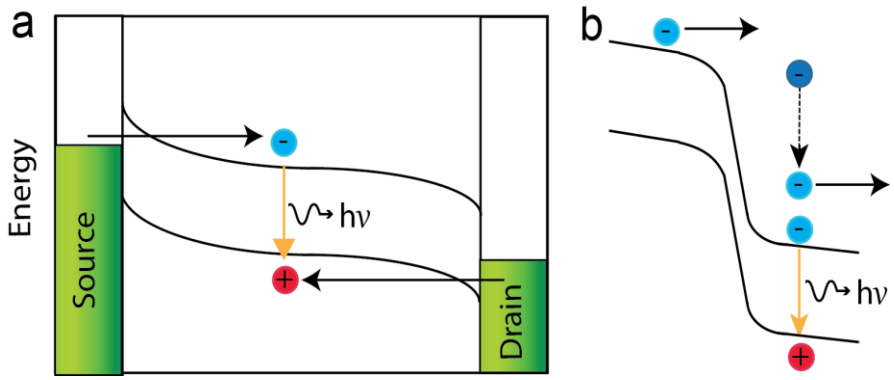

Figure 2.4 | Mechanisms of electroluminescence.

(a) Ambipolar emission mechanism (carrier recombination). Electrons and holes are injected from metal contacts and radiatively recombine in channel.
(b) Unipolar emission mechanism (impact excitation). A majority carrier (here an electron) is accelerated by the band bending and excites another electron-hole pair that radiatively recombines.

Besides of EL, both MeCNTs and SCCNTs can serve as incandescent light sources (10,63,64). Current flow through a CNT induces a significant self-heating of the tube, resulting in the broadband light emission. In the case of suspended CNTs the electron temperature increases stronger and the light emission occurs at lower voltages due to the inhibited thermal dissipation (63). Electron scattering by optical phonons leads to a high temperature $T_{op} \approx T_{el}$ and an increased non-equilibrium population of optical phonons that cannot relax into substrate. The temperature of acoustic phonons (CNT lattice) T_{ap} in suspended tubes is typically appreciably lower than T_{op}. Heat dissipation at contacts and by radiation is estimated to be below 5% (65), while the latter increases with the temperature. The temperature of electrically driven CNT can be extracted from its broadband thermal emission spectra according to the Planck's law (63,66), as shown in the experimental part (Subsection 3.4.1). In the case of suspended CNTs the determined temperature corresponds not to the temperature of CNT lattice, but is equivalent to T_{el} (65). The emission temperature typically ranges from 500 to 1500 K (63,64,67). The upper cut-off is strongly influenced by the measurement conditions as unprotected CNTs oxidize at the lattice temperatures above 800 K (68). For that reason the emission measurements are often performed under inert gas flow or in vacuum.

CNTs combine extraordinary high thermal conductivity of around 3 kW/Km (69) along the tube axis with small heat capacity (70) and ability to carry current densities of $10^9 A/cm^2$ (71). Although very uncommon, these properties attest CNT as a nanoscale thermal emitter with very fast response speed. Indeed, the electrical modulation of incandescent CNTs in Gbit/s range has been recently demonstrated (66).

Therefore, electrically driven CNTs emerge as both thermal and electroluminescent light sources. Incandescent CNTs, as broadband thermal emitters with ultra-fast response, appear as promising research object. Nevertheless, EL is often considered as more appreciated emission mechanism due to the narrower emission profile and chiralality-dependent direct bandgap of SCCNTs. Moreover, electroluminescent SCCNTs can operate in a single photon regime as discussed in the next subsection.

2.3.3 Single-Photon Emission

One of the sought-after topics in the modern photonics is the investigation of single-photon emitters. This kind of light sources produces only one photon at a time, demonstrating antibunched non-classical light emission. Such photonic qubits can be implemented for unconditionally secure communication (72). The realization of quantum computers, quantum cryptography and quantum simulators based on the single photon sources is being discussed (73–75).

There are several types of light sources (atoms, molecules, nanovacancies and nanostructures (76)) operating in a single-photon regime. At suitable conditions luminescent SCCNTs also reveal as quantum emitters (77–83) that is highly promising for both fundamental research and applied science. SCCNTs with their structure-dependent emission properties are good candidates for scalable integration into nanophotonic devices, while their relatively low efficiency becomes less important in the single photon emission regime. Additionally, SCCNTs belong to very few single-photon sources operating in the telecommunication wavelength range and can be electrically stimulated to light emission that has many advantages in comparison to optical pumping. However, till now no observations of single-photon emission from electrically driven SCCNTs have been reported.

The mechanism of single-photon emission in SCCNTs is not completely understood so far. In most studies localization of band-edge excitons at zero-dimensional structural defects or charge impurities is considered as the reason for antibunching (78,79,84) as schematically shown in Figure 2.5a. Since the localization potential is typically few meV deep, the antibunched emission from SCCNTs was observed only at cryogenic conditions until recently. Due to the oxygen doping, trap states with much deeper localizations and tunable emission wavelength can be realized. In this way, the room-temperature single-photon emission from SCCNTs incorporated in SiO_2 matrix was demonstrated for the first time (79).

Single-photon emission experiments are usually executed in a Hanbury Brown-Twiss configuration (85), in which the emitted narrow-line PL light is 50/50 splitted and guided to two single-photon detectors (Figures 2.5b,c). The time differences between photon arrivals to the detectors are measured and histogramed. The second-order delay

correlation function $g_2(t)$ describes the quality of quantum emitter. So called antibunching dip at zero delay time $g_2(0)$ in histogram serves as a signature of single-photon emission; for an ideal single-photon source $g_2(0) = 0$, while a classical emitter has $g_2(0) = 1$.

In PL experiments (77,78) performed in pulsed laser regime on both supported (Figure 2.5d) and suspended SCCNTs (Figures 2.5, e and f), $g_2(0)$ is close to zero (Figure 2.5g). Both the degree of antibunching (77) and PL-lifetimes (79) decrease with the higher temperatures and weaker exciton localization. As illustrated in Figure 2.5h, PL-lifetimes of suspended SCCNTs are typically between 1 and 10 ns, which is more than an order of magnitude longer in comparison to supported surfactant-encapsulated CoMoCAT-nanotubes (78,83). The emission count rates of PL-antibunching increase with the excitation power and saturate in the range of 1 kcps (Figure 2.5i, (77)).

Thus, SCCNTs can be used as single photon sources in the visible and NIR. The integration of electrically driven CNTs into photonic environment provides a necessary framework for study and application of their properties in both classical and single photon emission regimes. In the following the methods for CNT placement are overviewed.

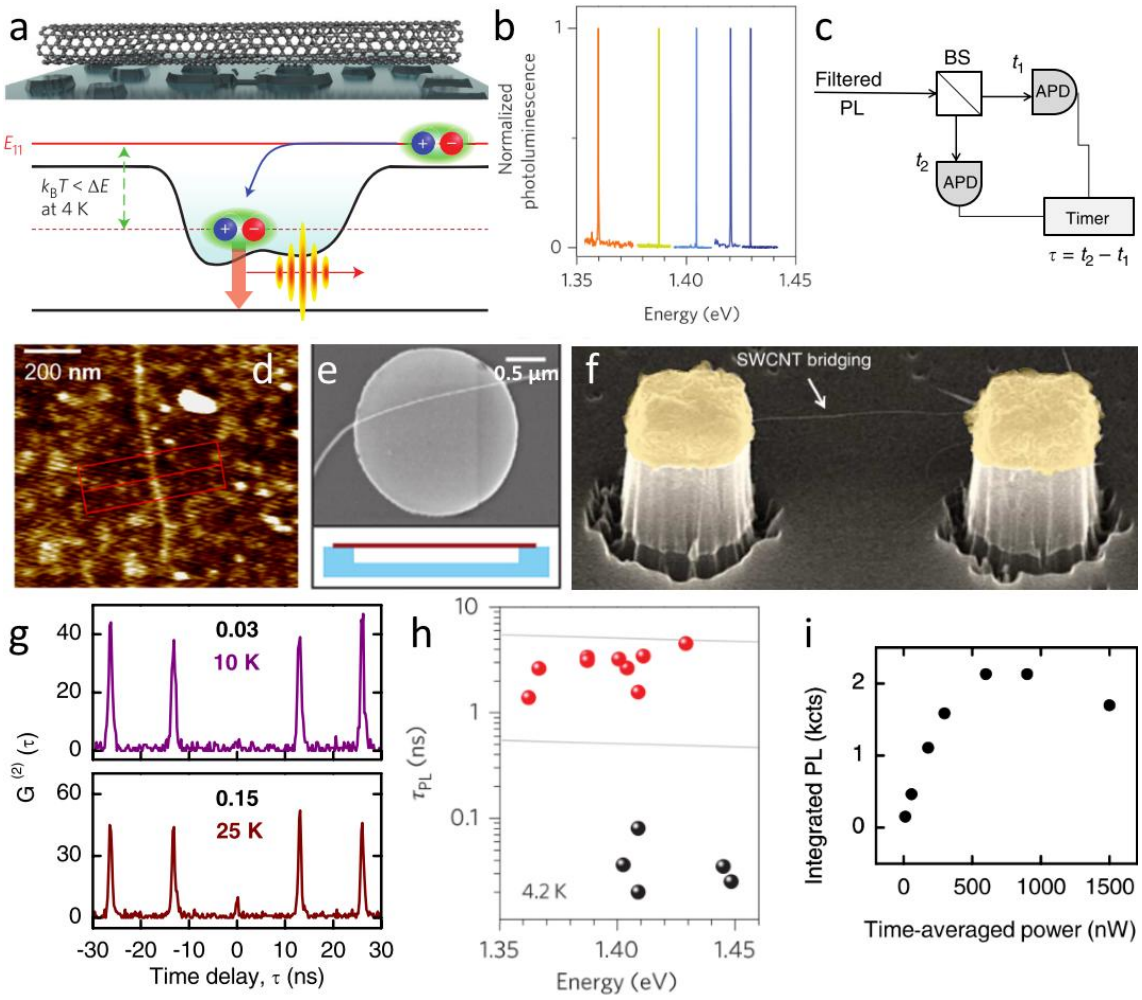

Figure 2.5 | SCCNTs as photoluminescent single-photon emitters.

(a) Schematics of photon antibunching mechanism in undoped SCCNT at cryogenic temperature. Excitons are localized in zero-dimensional trap states (red dotted line) a few meV (ΔE, green arrow) below the E_{11} state (79).
(b) PL emission from individual SCCNTs of different chiralities at cryogenic conditions (78).
(c) Schematics of Hanbury Brown-Twiss setup. Spectrally filtered light was 50/50 splitted using beam splitter (BS), time-correlated measurement was performed using two single-photon detectors (avalanche photodiode, APD) (83).
(d) Atomic force microscopy (AFM) image of a supported CoMoCat-SCCNT (77).
(e,f) Scanning electron microscopy (SEM) images of individual ac-grown SCCNTs suspended over SiO_2 crater with 200 nm depth (78) and between two pillar posts separated by 3 µm (83).
(g) Photon correlation spectrum measured at 10 K reveals $g_2(0) = 0.03$ indicative for a single-photon emission (pink line). The degree of antibunching decreases at higher temperatures with $g_2(0) = 0.15$ at 25 K (red line) (77).
(h) PL-lifetimes of supported surfactant-encapsulated SCCNTs in the range of 20 ps to 100 ps (black circles) are an order of magnitude lower than for suspended ac-grown SCCNTs (red circles) (78).
(i) Intensity of PL single-photon emission saturates with increasing excitation power (77).
Adapted with permission from (77–79,83).

2.4 CNTs in Nanophotonic Environment

2.4.1 Integration Techniques

There are a number of methods for organization of individual CNTs on substrates, involving growth, transfer and deposition techniques (8). CVD synthesis in combination with lithographically patterning of catalysts islands allows for a scalable site-selective CNT growth. An example of a CVD-grown SCCNT is provided in Figure 2.5f. This method is used for fabrication of CNT-based electronic (86,87) and photonic nanodevices (88). However it has a drawback that the synthesis is performed at high temperatures over 1000 K with only partially control over chirality and metallicity of the grown CNTs.

Alternatively, CNTs can be deposited on surfaces from purified and sorted suspensions with the favored parameters. Spin-coating (89,90) is chip and scalable, but does not provide any control over position and distribution of CNTs. In contrast, CNTs can be deposited at specific target locations using a nanopen (91), however, not on a scale of individual tubes. Very recently a directed assembly of end-functionalized (92) and DNA-wrapped CNTs (93) has been demonstrated. These techniques allow for a large scale placement of chirality-sorted individual CNTs onto chemically functionalized and lithographically patterned substrates and could be utilized for fabrication of CNT-based nanophotonic devices.

An efficient, scalable method for integration of CNTs into nanoelectronic systems is given with dielectrophoresis (DEP). DEP is an electrostatic phenomenon, describing motion of dielectric particles in a non-uniform electric field (94). In the presence of an inhomogeneous electric field a CNT becomes to an induced dipole and orients itself along the field gradient. Modeled as a prolate spheroid, CNT is experienced by the time-averaged DEP-force (95)

$$\langle F_{DEP} \rangle = \frac{\pi d^2 l}{8} \varepsilon_m \, Re\left(\frac{\varepsilon_t^* - \varepsilon_m^*}{\varepsilon_m^* + (\varepsilon_t^* - \varepsilon_m^*)L}\right) \nabla {E_{rms}}^2 \qquad (2.3)$$

with a depolarization factor L and complex permittivity of the tube and the medium $\varepsilon_{t,m}^* = \varepsilon_{t,m} - i\frac{\sigma_{t,m}}{\omega}$. $\langle F_{DEP} \rangle$ depends on the external factors (electric field strength E_{rms} and frequency ω), CNT metrics (length l, diameter d, dielectric constant ε and

conductivity σ) as well as on the characteristics of the medium. CNTs move toward regions of high field strength if their polarizability is higher than that of the medium. It is always the case for MeCNTs ($\varepsilon_t^{MeCNT} \geq 1000\varepsilon_0$ vs. $\varepsilon_{H_2O} \approx 80\varepsilon_0$). The polarizability of SCCNTs is much lower ($\varepsilon_t^{SCCNT} \approx 5\varepsilon_0$), so that at high frequencies $\langle F_{DEP} \rangle_{\omega \to \infty} \sim \frac{\varepsilon_t - \varepsilon_m}{\varepsilon_m}$ becomes negative. In this way, high-frequency DEP enables CNT separation by metallicity (96).

Low-frequency ac-DEP is widely used for the aligned deposition of solution-dispersed CNTs between pairs of electrodes by application of an alternating electric field (9). DEP is quick, cheap, causes no damage and provides less contamination. Typically it is employed for fabrication of CNT-based nanoelectronic devices. However, as shown in this thesis, DEP is well-suited for CNT-deposition into complex nanophotonic environments.

2.4.2 CNT-Based Integrated Light Emitters

In general, there are two classes of photonic devices most suitable for the integration of light-emitting CNTs, namely waveguides and microcavities. While waveguides are primarily used for the confinement and guiding of light over the chip, cavities serve for the enhancement and tuning of light emission. Both devices can be combined in a one to photonic crystal nanobeam cavity (PCNBC), which is an optical resonator directly incorporated into a waveguide.

A photonic waveguide consists of a longitudinally extended central core made of low-loss materials such as Si or Si_3N_4 surrounded by a cladding medium with lower refractive index (97). Light rays are guided through the waveguide along its longitudinal direction by total internal reflection. There are several types of waveguides such as optical fibers, planar and channel waveguides. Most waveguides employed in the device applications belong to the latter type. For example, the core of a channel rib waveguide used in this study is formed with a strip on top of the planar layer of the same material.

Microcavities (or microresonators) confine light within optical structures in order to establish optical resonance. The typical examples are Fabry-Perot interferometers, whispering galleries and photonic crystals (98). A figure of merit that describes the energy loss per cycle is the quality factor

$$Q = \frac{\lambda}{\Delta\lambda} = \frac{2\pi c\tau}{\lambda} \qquad (2.4)$$

with the resonance linewidth $\Delta\lambda$ and photon lifetime of the cavity τ. An important feature of microcavities is the enhancement of spontaneous emission by the environment, which can be described with the Purcell factor (99)

$$P = \frac{3}{4\pi^2}\left(\frac{\lambda}{n}\right)^3 \frac{Q}{V} \qquad (2.5)$$

The higher the Q factor and the smaller the mode volume of the cavity V, the stronger is the enhancement. CNT light emitters ideally suit for the integration inside the microcavity, as they barely disturb the resonance mode due to the tiny absorption cross section (100).

Most nanophotonic devices operate in the conventional telecommunication wavelength range (C-band, 1525 nm to 1565 nm), since light absorption in the silica-based glasses preferentially used in fiber-optics is minimal in this so called zero-loss window. However, for shorter distances the minimal losses are less important and other wavelengths (primarily 850 nm and 1300 nm) are widely used (101).

As discussed in the previous sections, CNTs act as light sources in the visible and NIR either in response to photoexcitation (PL) or to electrical current (incandescence and EL). Some CNT-species like (10,8)- and (10,9)-SCCNTs have their E_{11}-maxima in the telecommunication wavelength range (40). CNTs can be easily integrated into photonic environment, although most of the integration techniques lack on scalability or site-selectivity.

Figure 2.6 provides an overview about the SCCNT-based nanophotonic devices. It is important to mention that the majority of the devices were developed very recently, in parallel with the presented work and partially encouraged by it. In the most cases luminescent SCCNTs were integrated into cavities (82,88,102–107), but also the coupling of photoluminescent light into a waveguide was studied (105,108,109). The devices were fabricated using lithography techniques and SCCNTs were typically drop casted on the sample surfaces from the suspensions (82,102–107).

In Figure 2.6a a schematics of a back-gated, SCCNT-based FET is shown (107). With a metal mirror on top, the device acts as a Fabry-Perot planar microcavity. Electrically

driven light emission becomes highly directional and significantly narrower, while the emission maximum is shifted to the desired wavelength.

All other experimental works are dealing with photoluminescent, optically excited SCCNT emitters. Strong wavelength-selective enhancement of PL was observed by integration of SCCNTs into photonic crystal cavity (Figure 2.6b, (103)) and silicon microdisk (Figure 2.6c, (104)). This type of devices has smaller mode volumes and larger Q factor in comparison to Fabry-Perot cavities. In Figure 2.6d a ring resonator circuit with spin-casted SCCNTs on top is presented (105). In this device geometry SCCNTs can be optically excited using both surface-illuminated and collinear pumping. PL spectrum of the resonator demonstrates very sharp maxima with Q factor of 8000, which is the highest value reported for an integrated CNT-emitter so far. In the alternative approach, SCCNTs are CVD-grown onto photonic crystal nanobeam cavity (Figure 2.6e, (88)). These devices demonstrate narrow maxima, strong 300-fold PL enhancement due to the Purcell effect and very high coupling efficiencies of up to 92%. In contrast, the coupling efficiency for a CNT-emitter on top of waveguide is estimated to 10% (Figure 2.6f, (108)). For the proposed electrically-driven SCCNT-based laser, schematically shown in Figure 2.6g, a coupling efficiency of 60% was calculated (110).

The discussed photoluminescent devices are useful for study of the emitting behavior of CNTs in nanophotonic environments. However, the usage of these concepts in the applied research is greatly limited by the inability for the selective placement and excitation of individual tubes. In the following, a novel type of scalable integrated electrically driven CNT light source is presented.

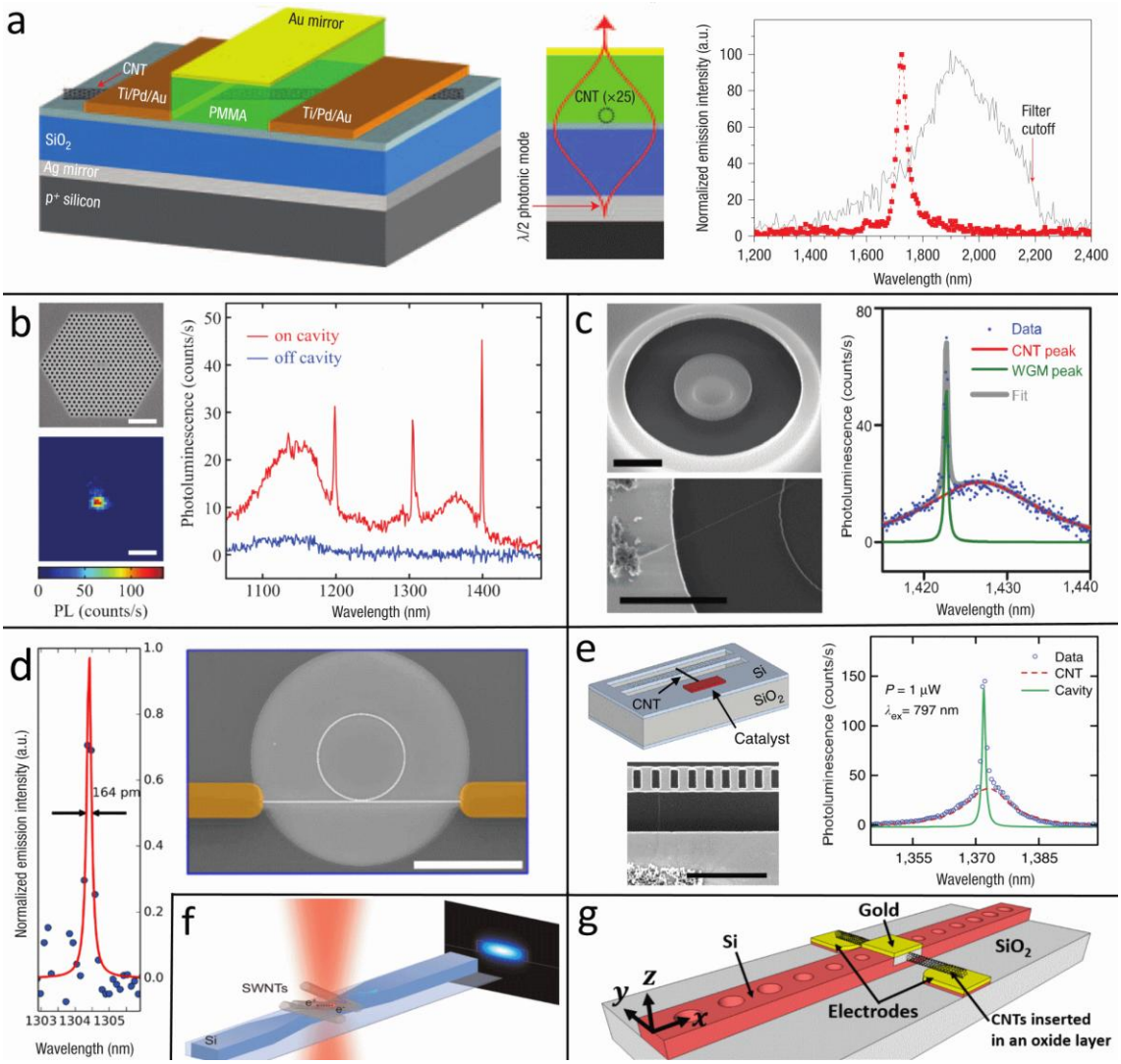

Figure 2.6 | Integration of CNT emitters into nanophotonic environment.

(a) Schematics of an electrically driven microcavity controlled SCCNT-based light emitter.
Emission spectra with and without top cavity mirror (red and black curves, respectively) (107).
(b) SEM image of a photonic crystal nanocavity and spatially resolved PL emission of integrated SCCNT.
PL spectra measured on and off the cavity (red and blue curves, respectively) (103).
(c) SEM images of a silicon microdisk with a suspended SCCNT.
PL spectrum (dots with Lorentzian fits) of SCCNT emission coupled to a microdisk (104).
(d) SEM image of a ring resonator covered with SCCNTs.
One of PL emission peaks with Q = 8000 (dots with Lorentzian fit) (105).
(e) Schematic and SEM image of a suspended SCCNT coupled to a nanobeam cavity.
PL spectrum of the device coupled to the SCCNT (dots with Lorentzian fits) (88).
(f) Schematics of photoluminescent SCCNTs coupled to a waveguide (108).
(g) Schematics of an electrically driven SCCNT-based PCNBC laser device. SCCNTs are embedded in oxide layer in the center of the PCNBC (110).
Scale bars: 2 μm in (b,c,e) and 50 μm in (d). Adapted with permission from (103–105,107,108,110).

3. Results and Discussion

3.1 Concept of Electrically Driven Waveguide-Integrated CNT

CNT as an integrable light source has a number of advantages. As described in the previous sections, CNTs emit in visible and NIR with GHz repetition rate (66). The variety of CNT types (metallic and semiconducting with different bandgap) demonstrates a broad range of electrical and optical properties (8). In combination with different excitation mechanisms (PL, EL and incandescence) this allows for a wide spectrum of possible applications. Moreover, electroluminescent SCCNT can act as single-photon source (77–79) that paves a way for on-chip integrated CNT-based quantum computers.

DEP provides a technique for controllable large-scale placement of CNTs in nanophotonic environments (9). Individual CNTs, typically 1 µm long, appear to be predestined for integration in waveguide architectures. Due to the tiny footprint and low absorption of nanotubes, the deposition of CNTs barely affects the transmissive properties of nanophotonic structures. CNTs can also be easily placed even in a complex environment as well as entirely removed using oxygen plasma. This makes nanophotonic structures a reusable (test) platform for CNT emitters of any type and density.

The PL excitation requires an external light source, reveals weak scalability and is not optimal for controllable addressing of individual devices. Therefore, the presented concept of Waveguide-Integrated carbon Nanotube light Source (WINS) envisages electrical excitation, resulting in heating-induced thermal emission and EL in the case of SCCNTs. Operating of light-emitting devices in two different emission regimes is an additional advantage for electrically driven CNTs in comparison to optical excitation. Not only for the integration and testing of CNT emitters in nanophotonic environments, but also for operating and optimization of wavelength-selective WINS-devices demonstrated in this proof-of-concept study (Sections 3.5 and 3.6), stable and reliable broadband thermal emission favors over relatively narrow-band EL. However, EL emission mechanism is preferential for the potential applications of WINS-devices, as

EL is more efficient, tunable via gating and doping as well as suitable for non-classical operation regime (Chapter 4).

The central building block of a WINS is schematically shown in Figure 3.1a (10). As can be seen there, the ends of the CNT bridge two yellow-colored metal electrodes, while the middle of the nanotube is in contact with the rib dielectric waveguide on top of the layered sample. The light propagating in the waveguides can be detected at their ends using grating couplers and fiber-optics system (Subsection 3.3.1).

By applying an electrical bias between the metal contacts the CNT begins emitting light. The distribution of the CNT-emitted light was simulated by Prof. W. H. P. Pernice using a 3D finite-difference time-domain (FDTD) method as shown in Figure 3.1b with the color code (Appendix A). The luminescent CNT on the waveguide-air interface was modeled as an electrical dipole (111) with the oscillating dipole moment perpendicular to the waveguide axis, as described in detail elsewhere (10). This model is also valid for incandescent CNTs, as one-dimensional thermal emitter demonstrates similar dipolar-like distribution of radiation (112). As shown in Figure 3.1b, the CNT-emitted light either spreads out in free space (I_E) or couples into substrate (I_C and I_{int}). Evanescent light coupling plays the most important role for electrically driven WINS. It leads to the propagation of radiation I_C inside the waveguide, as depicted in the cross-sectional view for 750 nm waveguide mode in Figure 3.1a. A part of the coupled light I_{int} interferes with the multilayered substrate and subsequently contributes either to the directly-emitted I_E or to the waveguide-coupled radiation I_C. The characteristic interference pattern distinctively influences the measured spectra in the both cases (Section 3.4).

There are few critical requirements to the device geometry and fabrication process. The metal electrodes should be close to each other, so that typically 0.5 µm to 1 µm long CNTs can bridge the gap. On the other hand, the distance between metal tips and waveguide walls has to be bigger than 200 nm in order to prevent damping of the CNT-emitted light by the metal electrodes (see also Section 3.6). This determines the choice of high resolution electron beam lithography technique for fabrication of WINS.

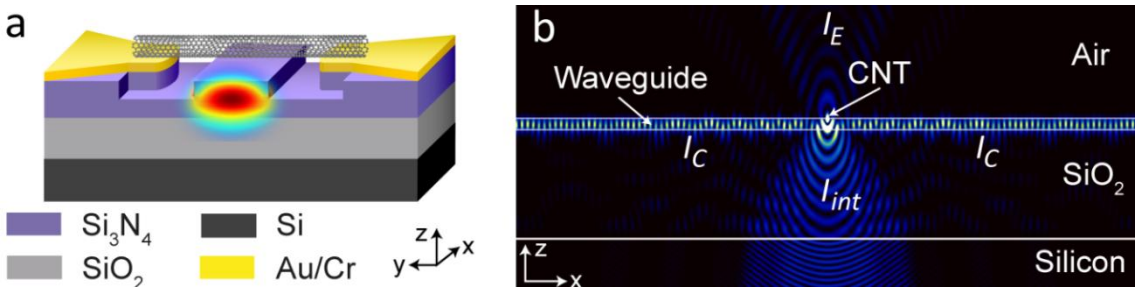

Figure 3.1 | Concept of electrically driven WINS.

(a) Schematic cross-sectional view of the multi-layer device structure (not to scale). The central waveguide is etched into the top dielectric layer and runs along the x-axis. The CNT is in contact with the metal electrodes and the waveguide, and aligned with the y-axis. A cross section through the waveguide mode at 750 nm is shown as a color overlay on the waveguide facet (intensity distribution of waveguide modes at other wavelengths are demonstrated in Appendix A).
(b) Cross-section through a 3D FDTD simulation of the electric-field intensity $\vec{E}^2$. The CNT is simulated as an electrical dipole at the waveguide-air interface, oscillating perpendicular to the x-z-plane.
Adapted with permission from (10).

The CNT sidewall should have a stable electrical contact with the metal electrodes in order to enable reproducible electrical characterization and emission measurements, but also to avoid energy losses and thermal degradation of the device during the operation. Moreover, for maximal coupling efficiency the nanotube should be placed as close as possible to the waveguide interface. Dielectrophoretic deposition technique fulfills these conditions.

The choice of the wavelength range in the experiment was limited by the emitting properties of CNTs, the spectral characteristics of the waveguide structures and detector's sensitivity. Electroluminescent CNT emitters operate primarily in the range of 500 nm to 2000 nm. In the case of broadband incandescent CNT emitters, both efficiency and position of the emission maximum are strongly temperature-dependent. It shifts from ≈ 3000 nm by 965 K towards 1500 nm at 1930 K according to the Wien's displacement law $\lambda_{max}\,(\mu m) = \frac{2897.8\ K}{T}$. In the wavelength regime relevant for CNT emitters the Si_3N_4 is the optimal waveguide material due to low loss from visible to mid-infrared (113), while silicon photonics technology based on doped Si-waveguides (114) is applied only for wavelengths beyond 1250 nm (101). Therefore, the operating wavelength range of WINS-devices in the presented study was determined in the first place by the sensitivity of the used Si detector, i.e. to the range of 500 nm to 1030 nm. This was not optimal for the measuring of CNT emission as both incandescence and EL

are stronger and more efficient at higher wavelengths. Among the wide variety of SCCNT species only those with the smallest diameter have their bandgaps in the accessible energy range (in particular (6,5)-CNT at around 980 nm (40)). According to the band structure of SCCNTs, there are also energy transitions of higher level (E_{22}, E_{33} ...) appearing at a shorter wavelength. However, the probability of such processes is much lower in comparison to the fundamental transition and the expected EL emission is both weaker and less efficient (54). Additionally, it is problematic to stimulate small-diameter SCCNTs to the EL emission as it requires higher energies to overcome the bigger bandgap. In contrast, the incandescent emission can be observed for both MeCNTs and SCCNTs in the accessible wavelength range. This allowed the investigation of CNT's emitting properties as well as light coupling and propagation capabilities.

With the installation of an additional InGaAs detector with the sensitivity ranging from 900 nm to 1600 nm, the observation of electroluminescent SCCNTs with larger diameter became possible at the end of this work (Section 4.1).

In the following the fabrication of the WINS is described in detail.

3.2 Fabrication

3.2.1 Lithography

All the WINS-devices fabricated during this thesis consisted of three components: nanophotonic waveguides with coupler gratings for optical connection, metallic contacts for electrical connection and CNTs as active light sources. The device fabrication was performed in three steps, as described in full detail in Appendix B and in the publications (10,11). At first, 50 nm to 100 nm thick metal contacts with a gap of 1.0 µm to 1.2 µm were formed on a doped Si-wafer with SiO_2 (2 µm) / Si_3N_4 (0.2 µm) top layers, using electron beam lithography and subsequent metal evaporation. Then, 0.5 µm to 0.7 µm wide rib waveguides, terminated with focusing grating couplers, were defined with electron beam lithography and formed by thinning 0.05 µm of the Si_3N_4 layer on both sides of the central strip in between the metal contacts by reactive ion etching. Optimal etching parameters for obtaining the nominal etching depth in combination with minimal surface roughness were identified using reflectometry, SEM and atomic force microscopy.

In order to enhance the CNT-emitted light at the selected wavelength, the CNT has to be integrated in the photonic crystal nanobeam cavities (PCNBC, Section 3.6). The fabrication of this complex device type is shown in details in Figure 3.2. Additional lithography steps were required to define photonic crystals and the cavity in the central part of the waveguide that were subsequently etched using hydrofluoric (HF) acid.

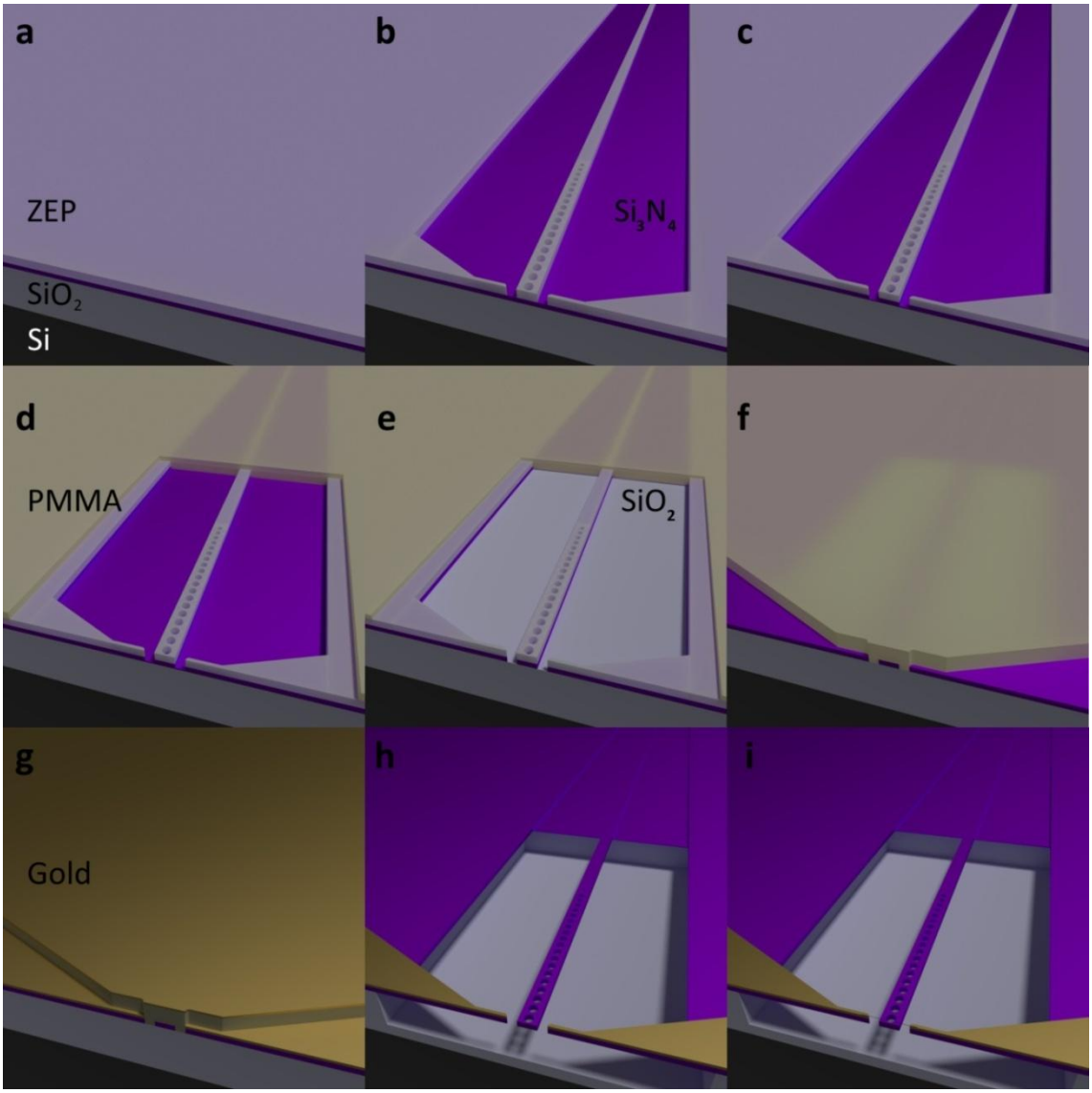

Figure 3.2 | Illustration of the PCNBC-device fabrication process.

(a) Sample with 4 layers of material: Si substrate (dark gray), SiO_2 insulator (light gray), Si_3N_4 (purple) and coated ZEP520a e-beam resist (translucent white).
(b) Resist after exposure and development.
(c) Reduced height of the unprotected Si_3N_4 after RIE.
(d) The sample is coated with PMMA (translucent yellow), then the window area has been exposed and developed.
(e) Removal of the remaining Si_3N_4 in the window area with another RIE step.
(f) Removal of resists, coating with PMMA, the electrodes area is exposed and developed.
(g) Gold is evaporated.
(h) PCNBC after lift-off and HF bath to remove the SiO_2 below the waveguide.
(i) Finished device after dielectrophoretic CNT deposition.
For further details see Appendix B.
Adapted with permission from (12).

3.2.2 Dielectrophoresis

The single-walled CNTs used in this study were provided in three types of suspensions:

- S1, water-based suspension containing predominantly SCCNTs and residual MeCNTs (Sections 3.4 and 3.5), prepared by Dr. B. S. Flavel using surfactant step-gradient technique (10,41).
- S2, toluene-based suspension containing SCCNTs (Sections 3.6-3.7 and Chapter 4), prepared by Dr. F. Hennrich using polymer wrapping technique (12,31,115).
- S3, water-based suspension containing MeCNTs (Sections 3.5-3.7 and Chapter 4) prepared by Dr. F. Hennrich and Dr. B. S. Flavel (12,116).

In all three cases HiPco nanotubes (Nanointegris) produced by catalytic chemical vapor deposition were used as the raw material for suspension preparation. The average length of CNTs varied from 0.5 μm to 1.0 μm, depending on the type, preparation process and fraction number of the suspension. The detailed recipes are listed in Appendix B.

The typical absorption spectra of the suspensions are shown in Figure 3.3a. In the course of the work several suspensions of each type with slightly varying CNT composition were used. The (n,m)-assignment for SCCNT suspensions S1 and S2 has been obtained from positions of E_{11} and E_{22} maxima on the basis of the data from the empirical Kataura plot (40). Notably, the maxima in absorption spectra, measured in aqueous and toluene-based suspensions, can slightly differ as it is influenced by the dielectric environment surrounding SCCNTs (117). Both suspensions contained SCCNT species from (6,5) to (10,8) with diameters between 0.75 nm and 1.25 nm. This is typical for HiPco material. Within the sensitivity range of Si detector only (6,5)-E_{11} and multiple E_{22}-transitions of SCCNTs with larger diameter could be observed in the intended emission measurements. The InGaAs detector, sensitive up to 1600 nm, allows for the characterization of E_{11}-transitions of all the SCCNT species present in the suspensions (in Figure 3.3a only a part of the absorption spectra below 1300 nm is shown, see also Chapter 4.1 with Figure 4.1).

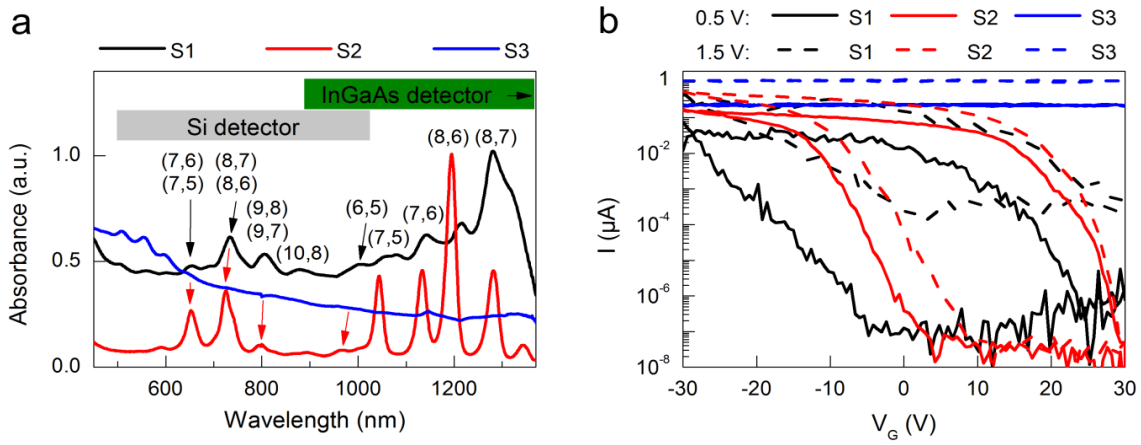

Figure 3.3 | CNTs in suspensions and devices.

(a) Absorption spectra obtained from suspensions with SCCNTs in water (S1, black) and toluene (S2, red) as well as MeCNTs in water (S3, blue curve). Sensitivity range of Si- and InGaAs detectors is labelled with grey and green color, respectively.
(b) The source-drain current I was recorded versus back-gate voltage V_G at source-drain voltages V_{sd} of $0.5\,V$ and $1.5\,V$. Transport measurements were performed on devices with deposited SCCNTs (red), SCCNTs and MeCNTs (black) or MeCNTs (blue curve).

The shoulder at the wavelengths smaller than 600 nm in absorption spectra of S1 and S3 are the signature of MeCNTs. Water-based suspensions S1 are typically more durable, but also contain more residual MeCNTs and contaminations than toluene-based suspensions S2.

The CNTs were deposited from the suspension between the metal contacts and onto the waveguide by ac-DEP, as schematically shown in Figure 3.4. The CNT suspension was diluted to the required concentration and dropped on the sample surface. A function generator SRS DS345 was used to apply a low-frequency voltage across the common ground electrode and the silicon substrate below the dielectric layer. The second electrode, specific to each device, was capacitively coupled to the common electrode and to the doped Si substrate. For CNTs longer than electrode gap, the DEP-force ensures alignment between the metal contacts perpendicular to the direction of the waveguide. Shorter tubes anchor to the common electrode without bridging the electrode gap and thus do not influence the electrical or emissive properties of the device. Variation of the DEP-parameters, such as exposure time, concentration of CNTs as well as amplitude and frequency of the applied voltage, allows for control over the number of CNTs deposited in between the metal contacts. These parameters depend on the structure geometry and CNT suspension. Typically, voltage was varied between 3 V

and 10 V with a frequency in the range of 1 MHz and 5 MHz.

After several minutes of DEP the sample was rinsed with toluene (S2) or water and methanol (S1, S3), and the voltage was switched off. Finally, the sample was annealed in oven at 150 °C for 2 hours to improve contact adhesion. Further details are provided in (9,96).

All WINSes were electrically characterized in a probe station setup before emission measurements. SCCNT-based devices prepared with suspensions S1 and S2 reveal p-type transport characteristics (Figure 3.3b, red and black curves). This is a typical behavior for FETs based on large bandgap SCCNTs (118). Devices fabricated using the toluene-based SCCNT suspension S2 show strong gate dependence, whereas devices with CNTs from the MeCNT suspension S3 demonstrated a much higher, gate-independent conductivity. Devices obtained by using S1-suspension mostly contained SCCNTs. However, there were also residual MeCNTs revealing in the increased off-state current at higher V_{sd}.

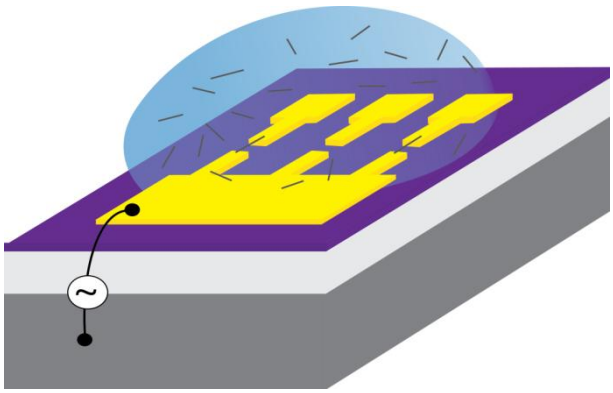

Figure 3.4 | Schematic illustration of dielectrophoresis.

Depending on the sample size, 10 to 50 µl drop of diluted CNT suspension was placed over the sample surface. An ac-signal was applied between the common electrode and the Si substrate. An external electric field polarized the CNTs, inducing an effective dipole moment inside the tubes and their alignment in the direction of the applied field. CNT were attracted to the regions of stronger electric field between the metal tips and bridged them on top of waveguides (not shown). In this way hundreds of electrode pairs were connected by CNTs simultaneously. After rinsing of the sample only CNTs attached to the electrodes remained on their places.

3.3 Characterization

In order to study and characterize the performance of the CNT-based nanophotonic devices, a number of primary optoelectronics experiments were carried out:

- Transmission measurements with an external light source (Figure 3.5a) provided information about functional (optical) properties of waveguide structures. This was essential for both optimization of fabrication process as well as obtaining of reference data for comparison with emission experiments.
- Electrical measurements served for characterization of metal-CNT-metal contacts and selecting out of devices with favored properties like CNT's type and number. The electrodes on the sample (gold contacts and silicon substrate as a gate) were connected by probe needles to Agilent 4155C semiconductor parameter analyzer in probe station setup.
- Emission measurements were the key experiments in this work, used for study of CNT-based light sources, coupling of the light into nanophotonic structures and propagation losses in waveguides. The devices were measured both spatially and spectrally resolved in the visible and NIR spectral ranges (Figure 3.5b).
- Finally, SEM imaging was performed using Zeiss Ultra Plus electron microscope for optimization of device fabrication and as concluding measurements after emission experiments in order to provide comprehensive information about device geometry such as CNT alignment in the nanoscale range.

3.3.1 Transmission Measurements

The measurement configuration for transmission experiments is schematically shown in Figures 3.5a and 3.5c. For the optical characterization the sample was fixed onto a movable XY-stage equipped with a piezo actuator (Picomotor, New Focus). An external supercontinuum white light source Leukos-SM-30-UV (output spectrum in the range of 380 nm and 2100 nm) was coupled into the chip plane using an 8 channel optical fiber array through Bragg diffraction on a grating coupler. All devices in this study were designed with a distance of 250 µm between grating couplers (or multiple of that), corresponding to the distance between adjacent fibers. Therefore, after propagation through the device, the transmitted signal was coupled out via a second grating coupler

port and measured with a JAZ Ocean Optics spectrometer (sensitive in the range of 340 nm and 1014 nm with resolution of 1.3 nm).

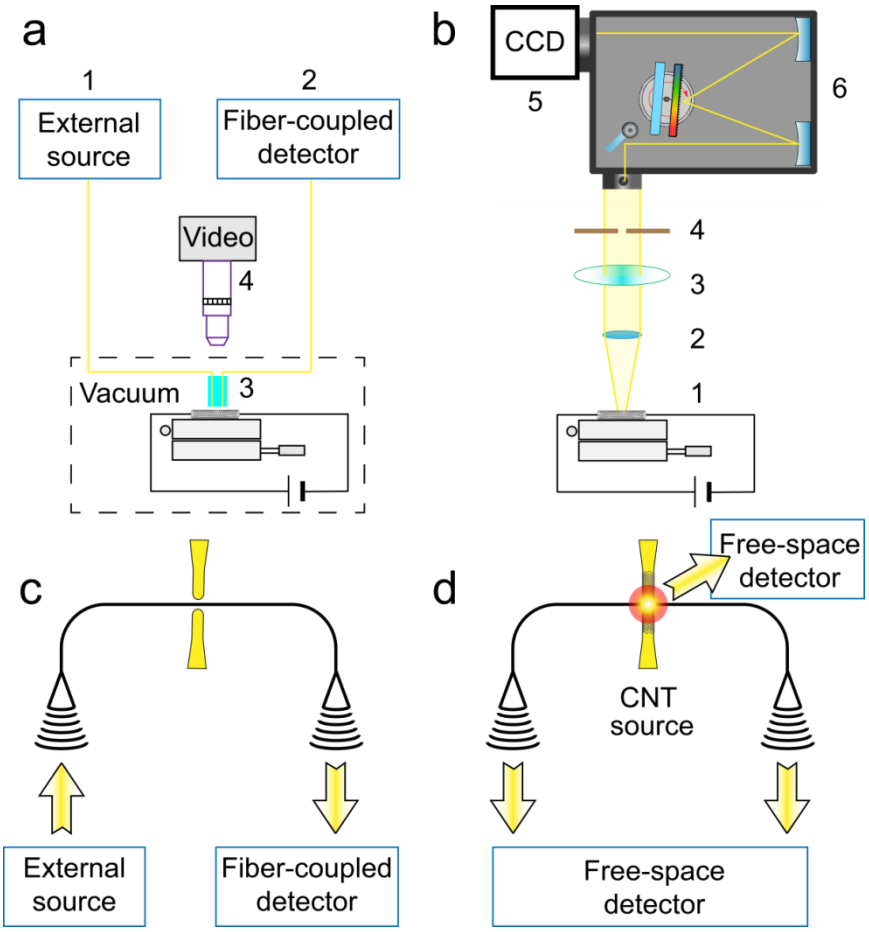

Figure 3.5 | Schematics of the transmission and emission setups.

(a) Transmission (fiber-optic) setup. Characterization of samples using a fiber-coupled external supercontinuum light source 1 and a fiber-coupled spectrometer 2. The sample is mounted on a piezo stage and aligned to a fiber array 3 using a CCD camera 4.
(b) Free-space characterization setup. The sample is mounted on a piezo stage 1, imaging and spectroscopy of the emitted light occur via a microscope (2-4) coupled to a high-sensitivity CCD camera 5 or spectrometer 6, respectively.
(c,d) Measurement configurations for characterization of samples using external and internal illumination, respectively.

3.3.2 Emission Measurements

The emission measurements were performed in free-space and in transmission setups. In the first case, the sample was mounted on a motorized stage and electrically connected below a Zeiss AxioTech Vario microscope in a light-tight box (Figures 3.5b and 3.5d). The microscope was directly connected to an Acton Research SpectraPro

2150i spectrometer and a Princeton Instruments PIXIS 256E Silicon CCD camera (1024×256 pixel, sensitive in the range of 500 nm to 1030 nm). The spectrometer was operated in the imaging mode, with a mirror in order to take real-space two-dimensional images, or in the spectroscopy mode, with a diffraction grating (300 grooves/mm, 750 nm blaze wavelength with spectral resolution of 1.5 nm). For most measurements Zeiss EC Epiplan-Neofluar 20x/0,50 and Motic Plan Apo 20x/0.42 objectives were used that have a spatial resolution of 1.3 µm. Zeiss LD EC Epiplan-Neofluar 100x/0,75 and Mitutoyo M Plan Apo 100x/0.70 objectives were employed for imaging with a higher resolution of 0.26 µm. The CCD detector was cooled down thermoelectrically to -55 °C in order to minimize the dark current occurring from thermally generated charges in the silicon lattice. With the noise level of about 2 counts per pixel per hour the integrating of the signal over extended time was possible, typical measurements took one to three minutes. By assuming an isotropic light source, the sensitivity of the setup was estimated to be around 100 emitted photons per count, taking into account the quantum efficiency and amplifier gain of the CCD, the efficiency of the grating and the geometrical constraints of the microscope optics. The absolute spectral calibration was performed with a mercury lamp. The characterization of relative spectral response of the system was done with a calibrated halogen lamp. The corresponding calibration curves were used for the correction of the recorded spectra. The calibration and the spectral properties of the free-space system are described in detail in the thesis of C. W. Marquardt (119).

In the transmission setup the CNT-emitted light was guided to the grating coupler ports and coupled out via fiber-optics to either the single-photon avalanche detector (τ-SPAD-100, PicoQuant) or the superconducting nanowire single-photon detector (SNSPD, SCONTEL).

In the both setups Keithley 6430 Sub-Femtoamp Remote SourceMeter as well as pulse generators HP 8131A and HP 8133A were used as voltage sources for dc and ac emission measurements, respectively.

All the experiments with exception of pulsed measurements (Subsection 3.7.2, vacuum) and single-photon emission measurements (Section 4.2, low-temperature vacuum) were performed at ambient conditions.

3.4 Emission and Coupling of Light into Waveguide

3.4.1 CNT-Based Emitter

An optical micrograph of a standard WINS-device is presented in Figure 3.6a. To the left and to the right of the CNT-based light emitting element (*E*) extends the waveguide with two Bragg grating couplers (*C1* and *C2*) at both ends at the distance of 250 µm. The waveguide serves for propagating of externally or internally emitted light and should have minimal losses at the operating wavelength of the device. For the given structure geometry this requirement is fulfilled for 500 nm to 600 nm broad waveguides etched into Si_3N_4 layer on top SiO_2/Si substrate (see Section 3.2 and Appendix A,B). Grating couplers typically serve in passive nanophotonic devices for in- and out-coupling of light in transmission measurements performed with an external light source. In the WINS-devices the couplers are also involved in the out-coupling of the CNT-emitted light from the waveguide into the far field. The central region of the WINS is shown in Figure 3.6b. In the false-colored SEM image the etched Si_3N_4-waveguide (purple) between two metal electrodes (yellow) is bridged by CNTs, appearing as thin white lines in the high-resolution inset.

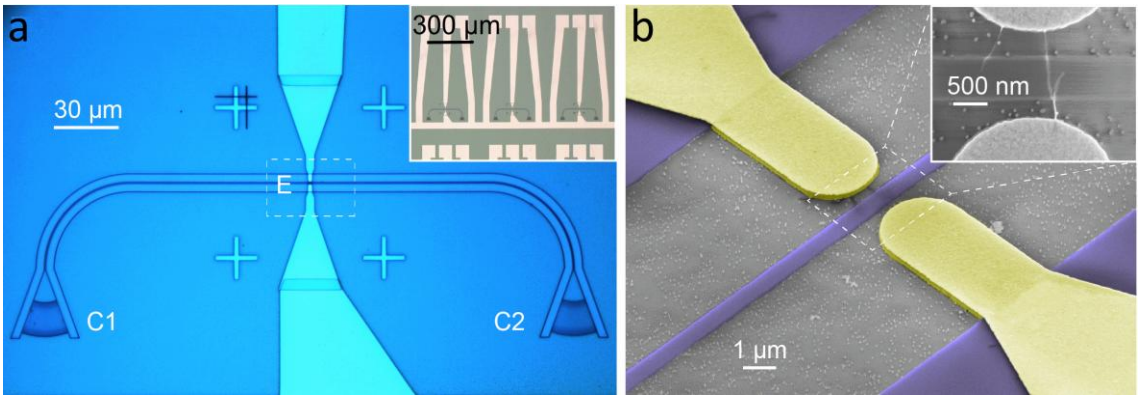

Figure 3.6 | Waveguide-coupled carbon nanotube light emitter.

(a) Optical micrograph of a complete device in top view comprising the metal contacts with the CNT emitter *E* and the extended photonic waveguide with two terminating coupler gratings *C1* and *C2*. The inset shows an array with multiple WINSes, one typical sample contained between 100 and 200 devices. (b) False-colored SEM micrograph of the central emitter region *E*, showing tips of two metal electrodes (yellow) bridged by a single-walled CNT (suspension S1) on top of photonic waveguide (purple). Tilt angle 45°. The inset shows the indicated region at higher magnification. CNTs appear as thin white lines. Adapted with permission from (10).

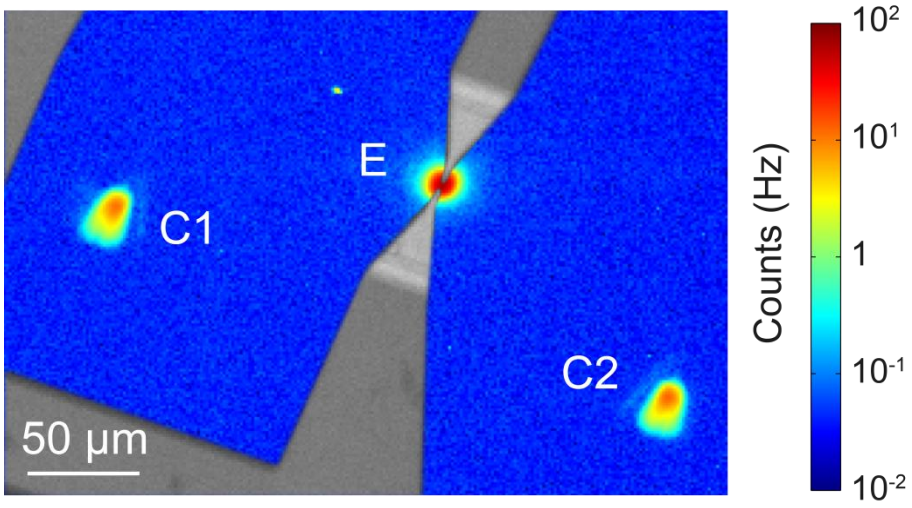

Figure 3.7 | Light emission and propagation.

CCD-camera image of the device shown in Figure 3.6 under electrical bias. Light emission is observed from the carbon nanotube emitter *E* and from the terminating coupler gratings *C1* and *C2*, both connected with *E* through the waveguide (not visible). Point-like spots randomly distributed over the image are transient measurement artifacts caused by cosmic rays. Superimposed is a grayscale image of the sample under external illumination to reveal the position of the electrodes.
Adapted with permission from (10).

Here and in the following experiments, the emission measurements were performed in the light-tight free-space setup. The sample was electrically connected and under applied voltage three emission spots were observed, as exemplarily shown in Figure 3.7. The central, strongest spot originates from the CNT emitter between the metal contacts. The gathered light was directly emitted in free space along the surface normal within 60° acceptance angle of the microscope objective. The positions of two weaker spots correspond to the both grating couplers. This emission was also caused by the CNT, since the emitted light partly coupled into the waveguide, propagated inside it and was diffracted at the couplers. The comparison of the integral emission intensity of light spots at *E* and *C* reveals high coupling efficiency of the CNT-emitted light into the waveguide, as discussed in the following (Subsection 3.4.3). Figure 3.7 illustrates the key result of this work. For the first time the coupling and propagation of the light emitted by electrically driven CNT in nanophotonic environment was observed. Therefore, CNT can serve as a scalable integrable light source for optoelectronic applications on chip.

In the scope of this thesis about 500 electrically driven WINSes were characterized. Standard WINS-devices, prepared using all the three CNT suspensions, demonstrated

nearly identical emitting behavior similar to the one shown in Figure 3.7. Depending on the type and number of deposited CNTs, the light emission occurred in the broad range of 3 V and 30 V, which corresponds to the electrical power of 0.1 µW to 1 mW. SCCNTs typically emitted at higher voltage and lower electrical power (10 to 20 V and 0.1-10 µW) than MeCNTs (3 to 5 V and 10 to 100 µW). The long-time stable emission with the measured count rates in the range of 1 Hz and 1 MHz can be reversibly triggered by modulation of electrical power, as demonstrated in several examples in the next sections.

All the devices prepared with suspensions S1 and S3 as well as about 90% of devices with CNTs from suspension S2 demonstrated broadband incandescence (63,64). A series of typical incandescent spectra measured at *E* is depicted with colored symbols in Figure 3.8a, revealing two signatures. The black body radiation profile with increasing emission intensity towards higher wavelength is overlained by the self-interference of the emitted light with $Si_3N_4/SiO_2/Si$-substrate. This kind of strong interference was observed in several studies (120,121).

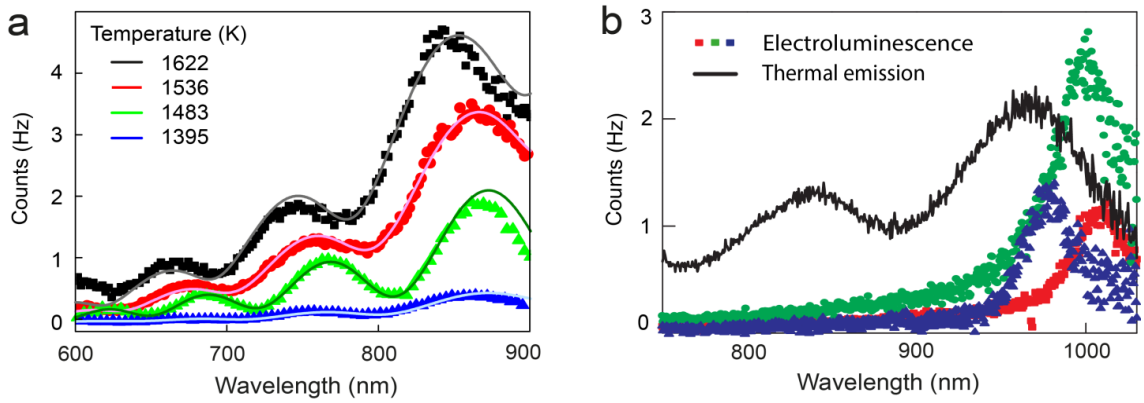

Figure 3.8 | Emission spectra of electrically driven CNTs.

(a) Sequence of incandescent CNT spectra recorded at emitter *E* with increasing electrical power dissipation. The data is fitted with a Planck spectrum modulated by substrate induced interference fringes (Equation 3.1). The fit-parameter temperature is given for every curve.
(b) Sequence of electroluminescent spectra (red, green and blue symbols) with a single pronounced maximum attributed to (6,5)-SCCNTs. Incandescent CNT spectrum (black line) is plotted for comparison. Adapted with permission from (10).

The incandescent CNT emission can be described as

$$I_{CNT}(\lambda) = I_d(\lambda) + I_r(\lambda) + 2\sqrt{I_d(\lambda) I_r(\lambda)}\, Re\left(\gamma_{d,r}\right) \quad (122)$$

$$\propto f_{Planck}(\lambda, T)\,(1 + 2\,Re\left(\gamma_{d,r}\right) f_{int}(\lambda)) \qquad (3.1)$$

with $I_d(\lambda)$ and $I_r(\lambda)$ intensities of directly emitted and reflected light. $\gamma_{d,r}$ is the degree of coherence function and describes the visibility of interference, for fully coherent source $|\gamma_{d,r}| = 1$. The measured emission spectra were fitted as function of black body emission according to the Planck's Law

$$f_{Planck}(\lambda, T) \sim \frac{1}{\lambda^5 (e^{-hc/\lambda k_B T} - 1)} \qquad (3.2)$$

modulated with the interference term

$$f_{int}(\lambda) = Re(r(\lambda)\, r^*(\lambda)) \qquad (3.3)$$

where $r(\lambda) = 1 - k \times reflectance(\lambda)$ with the reflectance(λ) calculated for CNT emitter localized on top of $Si_3N_{4\,(0.2\,\mu m)}/SiO_{2\,(2\,\mu m)}/Si$ substrate using transfer matrix approach (97). The coefficient k represents the fraction of light that is streamed into the substrate.

The fitted curves $I_{CNT}(\lambda)$ are shown in Figure 3.8a as narrow lines. The extracted electron temperatures are typically in the range of 1100 K and 1700 K, in agreement with the values reported in other works (63). The maximal temperatures are limited by melting of metal contacts and oxidation processes. However, the CNTs themselves remain stable even beyond 3000 K in vacuum (123).

From the simulation (Equation 3.1) the degree of coherence $\gamma_{d,r\,(sim)} = 0.016 - 0.025$ was derived, which can be compared with the theoretical estimation

$$\gamma_{d,r}(T, \tau) = \int_0^\infty f_{Planck}(\nu, T) e^{-2\pi i \nu \tau}\, d\nu \quad (124) \qquad (3.4)$$

depending on the delay time between the emitted and reflected photons, propagated in Si_3N_4 and SiO_2 layers (reflective indices $n_{Si_3N_4} = 2.01$ and $n_{SiO_2} = 1.544$)

$$\tau \equiv \frac{\Delta z}{c} = \frac{2\,(n_{Si_3N_4}\,0.2\,\mu m + n_{SiO_2}\,2\,\mu m)}{c} = \frac{6.98\,\mu m}{c} = 23.3\,fs \qquad (3.5)$$

With the extracted temperatures of CNT emitters (Figure 3.8a) the estimated degree of coherence: $\gamma_{d,r}\left(1395\,K - 1622\,K, 23.3\,fs\right) = 0{,}0026 - 0.0040$. The superiority of the fitted degree of coherence over the calculated values probably results from the reduced dimension of the CNT emitter, thus increasing the coherence (120). The number of CNTs as well as the applied voltage affects the intensity of the incandescent emission and the temperature of the contact, but typically don't change the spectral profile.

Only a few devices prepared with S2-suspension did not reveal a significant incandescent component, but a distinct EL maxima (48,125) at around 1000 nm corresponding to the radiative E_{11} -transition of (6,5)-SCCNTs (40), as shown in Figure 3.8b (red, green and blue curves). EL emission was mostly observed by the characterization of test devices without waveguides at 10 to 20 V and 0.1 to 1 µW. The maxima exhibited FWHM of around 50 nm that is rather narrow in comparison to the EL measurements on short-channel devices with typically 50 to 200 nm broad maxima (49,53,126,127). As already mentioned in Section3.1, there are several reasons for the absence of electroluminescent signatures in the majority emission spectra measured in the wavelength range below 1030 nm. In consistence with the majority of the electronic transport measurements (Figure 3.3b, black curves), the presence of residual MeCNTs in suspension S1 typically led to devices with mixed CNT networks and dominant contribution of thermal emission. Even for the purely semiconducting devices prepared using suspension S2, self-heating of SCCNTs at higher electrical power, required for EL emission in the visible range, induced a significant incandescent background that probably hindered the observation of weaker and relative broadband E_{22} signal. Most of the SCCNTs in suspensions S1 and S2 had E_{11} transitions outside the sensitivity range of Si detector up to 1030 nm. Thus, the strongest component of EL could not be observed to the time of the experiments described in Sections 3.4-3.7. Only at the end of this work, with the installation of the InGaAs detector, the spectral characterization of CNT emission in the NIR up to 1600 nm became possible. Initial measurements performed in this wavelength range on the test devices revealed pronounced electroluminescent emission, as demonstrated in the Section 4.1.

Therefore, most electrically driven WINSes presented in this thesis were operated in incandescent emission regime. Such important parameters of WINS-devices as coupling efficiency, propagation losses and out-coupling of the guided light are discussed in more detail below.

3.4.2 Propagation Losses

An essential characteristic of WINS, especially considering potential applications, is the propagation loss for the light guided on the chip. In order to determine the losses, a series of devices with asymmetric long waveguides was fabricated (Figure 3.9a, (10)). The length of the waveguide arm between CNT emitter *E* and coupler *C2*, L_{E-C2} , varied from 1.6 mm to 10.1 mm in the seven steps, while all other structural parameters like grating couplers and the length of the shorter waveguide arm $L_{E-C1} = 25$ µm were kept unchanged.

The transmission performance of the devices was characterized in the fiber-coupled setup (Figure 3.5b) using an external light source with the signal intensity I_0. The Gaussian-shaped transmission spectra with Fabry-Perot-like intensity modulation were dominated by the narrow-band couplers, the maxima appeared at the characteristic wavelength of the used gratings $\lambda_{gratting} = 756\,nm$ (Figure 3.9c, see Subsection 3.4.4). The propagated light is getting partially absorbed in the waveguides, so that the transmission intensity exponentially decays with the increasing pass way $I \sim e^{-\alpha L}$. The propagation losses per unit length were determined:

$$\alpha_{transmission} = \frac{d}{dL}\left(log\frac{I_0}{I_{C2}(L)}\right) \qquad (3.6)$$

as shown in Figure 3.9d.

The average loss $\alpha(756\,nm)_{transmission} = 12.7 \pm 1.2\ {}^{\mathrm{dB}}/_{\mathrm{cm}}$ is a standard value for the type of waveguide geometry used in this work (128).

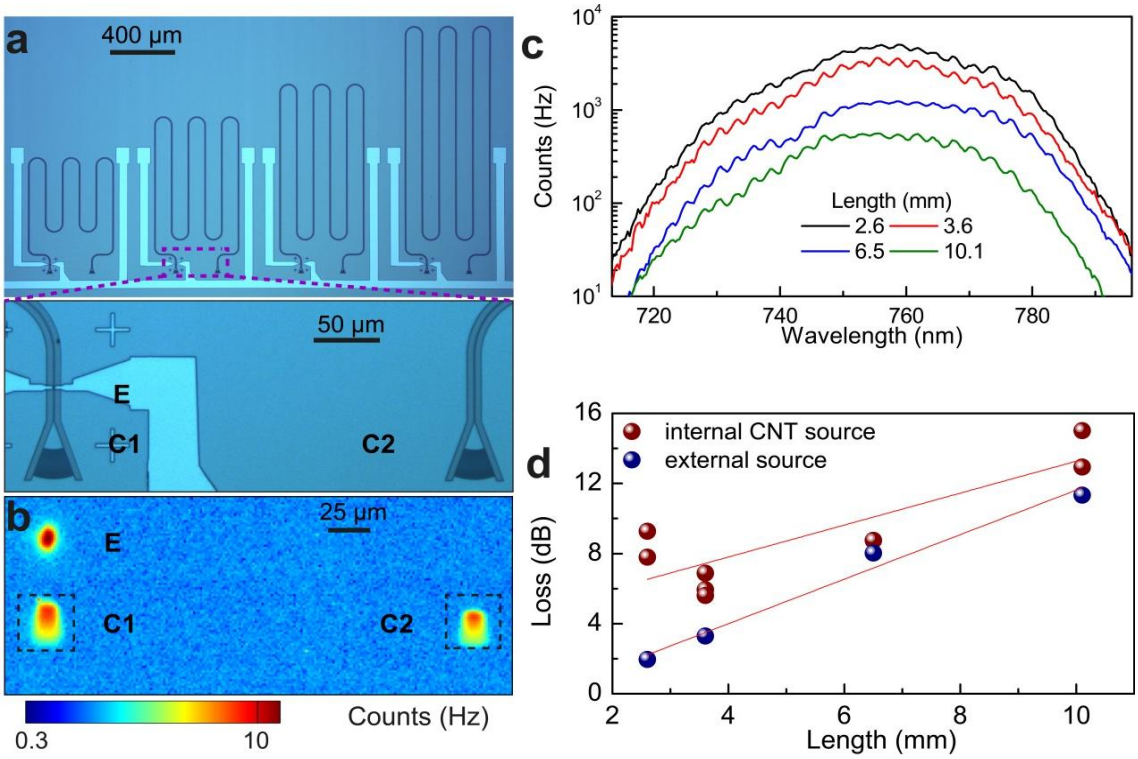

Figure 3.9 | Propagation loss in extended waveguide structures.

(a) Optical micrographs of 4 out of 7 devices with asymmetrically long waveguide segments between the CNT emitter *E* and the coupler gratings *C1* and *C2*. The total waveguide length *L* between *C1* and *C2* for the devices shown here is 3.6 mm, 5.3 mm, 6.5 mm and 7.3 mm.
(b) CCD-camera image of the device with *L* = 6.5 mm under electrical bias. Light emission is observed from the CNT emitter *E*, the nearby coupler *C1* and the remote coupler *C2*. Losses in the waveguides are calculated from the integrated scattering light intensities I_{C1} and I_{C2} at *C1* and *C2* within the dashed regions, respectively.
(c) Transmission spectra of complete devices (*C1*-waveguide-*C2*) measured with an external supercontinuum light source. Fabry-Perot-like intensity modulation in spectra is caused due to reflexions between grating couplers and optical fibers. Losses in the waveguide are calculated from the decreasing signal intensity at the peak wavelength 756 nm with the increasing waveguide length *L* and are plotted in (d).
(d) Comparison between losses in the waveguide determined with the external supercontinuum light source (blue) and with the integrated waveguide-coupled CNT light emitter source (red).
Adapted with permission from (10).

After CNT deposition the emission measurements were performed in the free-space setup. The amount of photons emerging from the biased CNT emitter and propagating through a waveguide towards the couplers is identical for both directions. Therefore, the observed discrepancy between the light intensities I_{C1} and I_{C2} in Figure 3.9b can only be accounted for by the different pass ways $L_{E-C1} \ll L_{E-C2}$. The presented devices allow determination of propagation losses unaffected by such variable parameters of CNT light sources as excitation mechanism, emission intensity and efficiency of coupling into the waveguide. The integrated signal intensities within the indicated regions for

devices having different lengths were measured and the losses in emission mode were calculated

$$\alpha_{CNT} = \frac{d}{dL}\left(10\, log \frac{I_{C1}}{I_{C2(L)}}\right) \qquad (3.7)$$

The determined $\alpha_{CNT} = 9.1 \pm 2.1\ {}^{\mathrm{dB}}/_{\mathrm{cm}}$ is reasonably close to $\alpha_{transmission}$, as shown in Figure 3.9d. The absolute loss in the emission mode is higher because of contamination of the long waveguides after CNT deposition. Above all, the light scattering inside the waveguide bends significantly contributes to the absolute losses in the devices. Nevertheless, CNT-emitted light propagates over centimeter distances on chip and can be detected and characterized at the remote coupler.

Typical WINS-devices with straight waveguide arms $L_{WG} \approx 100\,\mu m$ have the absolute propagation losses of 0.1 dB, i.e. only 2% of light intensity gets lost. These marginal changes can be neglected in the majority of applications. In fact, the quality of the used waveguided devices was improved with time and thus the recently fabricated structures exhibited significantly higher transmission. The low losses make the presented experimental platform suitable also for measurements in single-photon emission regime. The demonstrated results attest an excellent performance of WINS-devices in the guiding of light on a chip.

3.4.3 Coupling Efficiency

The yield of the waveguide-integrated emitters is typically determined by the amount of light coupled into the waveguide, while the light emitted in free-space is lost. Therefore, the intensity of the coupled light I_C measured on the grating couplers should be maximized in comparison to the intensity of the directly emitted light I_E. The lower limit of coupling efficiency $\eta_{coupling}$ of the CNT-emitted light into the waveguide was estimated as the ratio of the out-coupled light scattered at the both couplers $2I_C$ to the entire emission:

$$\eta_{coupling} \geq \frac{2I_C\, L_{WG}\, \alpha_{CNT}}{I_E + 2I_C\, L_{WG}\, \alpha_{CNT}} \approx \frac{2I_C}{I_E + 2I_C} \qquad (3.8)$$

As mentioned above, the devices presented in this work typically had relatively short waveguide length L_{WG}. Thus, the influence of the total propagation loss $L_{WG}\, \alpha_{CNT}$ on

the measured I_C was insignificant and could be ignored. The decrease of I_C due to the bending losses and contaminations as well as out-of-plane scattering at the grating couplers was also not taken into account.

$\eta_{coupling}$ was determined based on both spectrally and spatially resolved emission measurements. In the first case, simultaneously recorded spectra $I_E(\lambda)$ and $I_C(\lambda)$, exemplarily shown in Figure 3.10a, were compared. The spectral properties of the waveguided and out-coupled light $I_C(\lambda)$ are nearly identical with $I_E(\lambda)$, demonstrating the same incandescent emission profile with interference fringes. I_C was weaker than I_E at any wavelength and the relation between $I_C(\lambda)$ and $I_E(\lambda)$ was nearly wavelength-independent besides of the deep at around 880 nm that is discussed in the next subsection. Figure 3.10b demonstrates $\eta_{coupling}(\lambda)$ calculated according to Equation 3.8 for three WINSes. As it could be expected from Figure 3.10a, $\eta_{coupling}(\lambda)$ is almost constant in the broad operating wavelength range. Therefore, the efficiencies of coupling and transmission in WINS-devices are nearly wavelength-independent. For the best device (black symbols) coupling efficiency exceeds 60%.

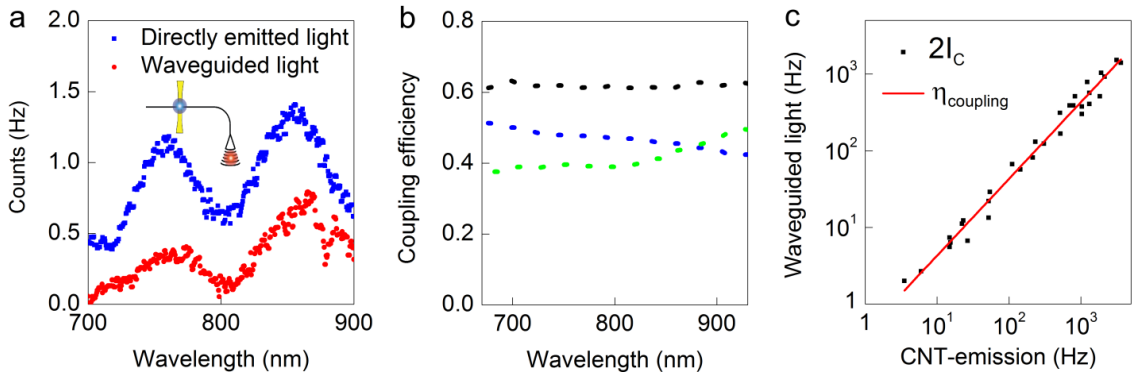

Figure 3.10 | Coupling efficiency.

(a) Emission spectra simultaneously recorded at CNT emitter *E* ($I_E(\lambda)$, blue line) and coupler *C1* ($I_C(\lambda)$).
(b) $\eta_{coupling}$ (λ) for three WINSes with relatively high coupling efficiency, based on simultaneously recorded emission spectra $I_E(\lambda)$ and $I_C(\lambda)$.
(c) Integrated intensity of coupled light $2I_C$ as function of entire emission intensity $I_E + 2I_C$ measured on dozens of WINSes with fitted $\eta_{coupling} = 0.43 \pm 0.03$.

However, spectral measurements can be performed only for the light sources with count rates over 100 Hz. At lower emission intensities $\eta_{coupling}$ was calculated based on the comparison between integral light intensities of simultaneously measured emission spots (see Figures 3.7 and 3.9b). Typically, I_E was 1.5 to 10 times stronger than I_C. In Figure 3.10c the intensities of the guided emission $2I_C$ are plotted over the entire CNT emission intensity $I_E + 2I_C$ for dozens of WINS-devices. The linear fit to the data provides $\eta_{coupling} \approx 0.43$ as an average of the coupling efficiency for the standard WINSes. These results are in the same order as the reported $\eta_{coupling}$ of comparable waveguide-integrated emitters (129,130) and several times higher as estimated coupling efficiency for waveguide-integrated photoluminescent SCCNT (108). Remarkably, the average $\eta_{coupling}$ remains the same over three orders of magnitude of emission intensity. Among factors affecting $\eta_{coupling}$ were number, density and alignment of CNTs. In most cases $\eta_{coupling}$ was higher for single-tube devices in comparison to multi-tube structures.

WINS-devices demonstrate an efficient broadband coupling of CNT-emitted light into waveguide. Their performance can be further enhanced by optimizing the nanophotonic environment. For instance, integration of CNT emitter into a photonic cavity allows efficient wavelength-selective coupling along with intensity enhancement as shown in Section 3.6.

3.4.4 Out-Coupling of CNT-Emitted Light

The out-coupling mechanism of the CNT-emitted light is discussed in more detail in this section. Figure 3.11a demonstrates a SEM image of a typical fabricated grating coupler. The grating etched into the Si_3N_4 layer provides in- and out-coupling of the external faser-coupled light with the incident angle of $\theta = 8°$ (131–133). After passing the grating, the incoming collimated beam was focused by a taper in the waveguide plane. The central coupling wavelength is determined by the effective refractive index of the grating n_{eff}, which depends on the refractive index of material n_{top}, diffraction mode m and grating period P (inset of Figure 3.11):

$$n_{eff} = n_{top} \sin(\theta) + m\frac{\lambda}{P} \quad (134) \qquad (3.9)$$

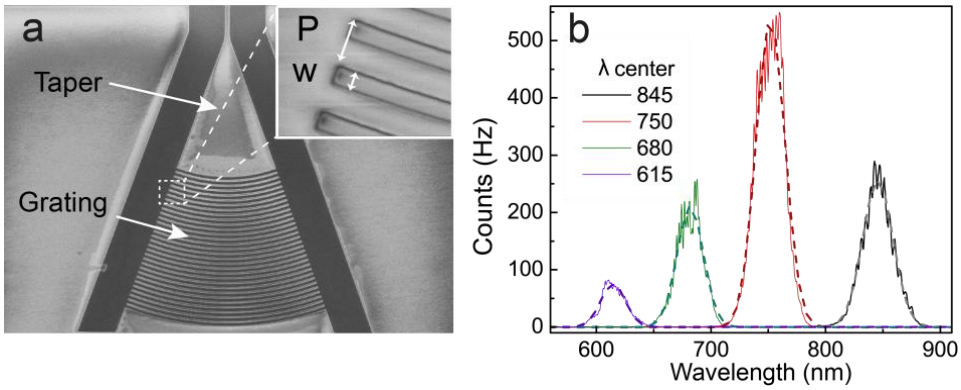

Figure 3.11 | Properties of grating coupler.

(a) SEM micrograph of a grating coupler. Inset: a zoom into the grating section with assignment of geometric dimensions.
(b) A Gaussian fit (dashed lines) to the measured data (solid lines) reveals the central coupling wavelength for the devices with different grating periods *P* (400, 440, 520 and 585 nm for lila, green, red and black curves). The coupling bandwidth of the devices is in the range of around 30 nm.
Adapted with permission from (10).

Therefore, the peak wavelength of the Gaussian coupling profile can be adjusted by variation of *P*. In Figure 3.11b transmission profiles of several devices with different grating distances are shown. The transmission through the waveguided structures fluctuated in the range of 1% and 10% from device to device mainly limited by the insertion loss of grating couplers. In transmission spectra of WINS-based devices neither peak wavelength nor intensity were significantly changed after CNT deposition.

In the emission measurements grating couplers served as outputs for internally emitted light coupled into the waveguide. As shown in Figure 3.7, the emission spots corresponding to the grating couplers *C1* and *C2* are of similar size and intensity. In the high-resolution CCD camera image, superimposed with SEM micrograph of the coupler, two emission regions stand out (Figure 3.12a). Only light with the characteristic wavelengths determined by the grating period *P* can propagate along the gratings to the end of the coupler. Therefore, the grating serves as a spectral filter and the spectra recorded at the remoted regions of the couplers are dominated by the Bragg scattered light with corresponding maxima at wavelengths λ_i as demonstrated in Figure 3.12b on the example of two devices with different *P* (Figure 3.12b, blue and orange lines). In contrast, all the photons with shorter or longer wavelengths diffusively scatter at the first grating lines, therefore these areas of the coupler reveal maximal

signal intensity. The spectra of the light collected at diffusive scattering regions reveal distinct dips at λ_1 and λ_2, respectively.

Thus, the emitting, waveguiding as well as in- and out-coupling properties of standard electrically driven WINSes were characterized. Further sections consider more complex nanophotonics devices with integrated CNT emitters.

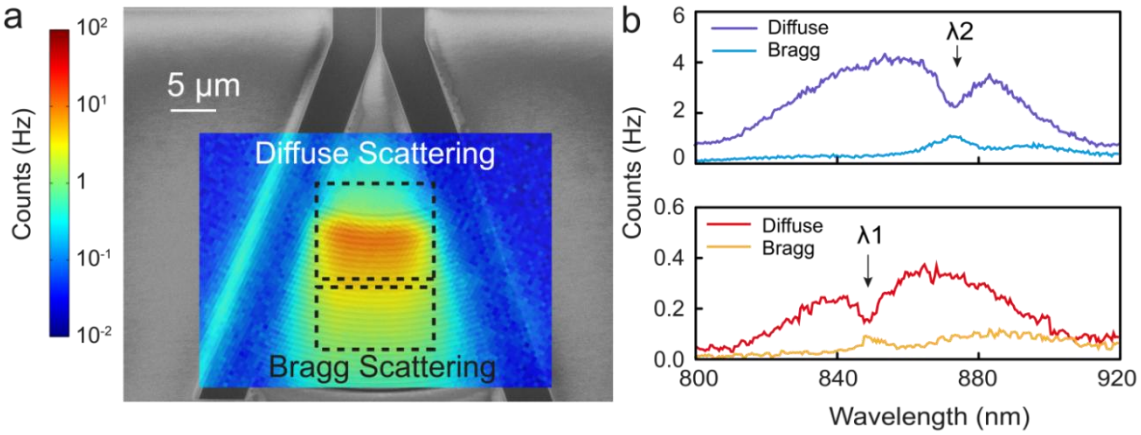

Figure 3.12 | Out-coupling of CNT-emitted light.

(a) High-resolution CCD camera image of the coupler grating *C2*. Indicated are regions of diffusive scattering and Bragg scattering, close and remote from the waveguide entrance, respectively. Superimposed is a SEM image of *C2* to reveal the position of the waveguide (entering from top).
(b) Spectra from *C2*, recorded at regions of diffusive scattering and Bragg scattering, respectively, at two structures with different grating periods. Spectra from diffusive scattering are similar to the spectra of *E* although with dips at λ_1 and λ_2. The missing intensity is recovered in the spectra from the Bragg scattering as explained in the text.
Adapted with permission from (10).

3.5 Nanophotonic Devices with Light Emitting CNTs

3.5.1 Interferometry Experiments

Waveguides are the core component of NPIC, allowing for the propagation of light to arbitrary positions on a chip, similar to wires in electrical circuits. Aside from them, the rich toolbox of nanophotonics provides a number of NPIC-devices for investigation of optical phenomena in a chipscale framework. The prominent examples of passive integrated devices are nanocavities, photonic crystals, modulator and couplers, changing direction, amplitude or spectrum of the passing light in a controlled manner.

CNTs as an electrically-triggered photon sources with a tiny footprint can be integrated into various NPIC-components. In this section two such nanophotonic devices with CNT-based emitters are presented: Mach-Zehnder interferometer (MZI) and directional coupler (DC).

MZI modulates the intensity of light in the broad wavelength range. This feature was used to demonstrate an electrically driven light interference on a chip (10). The MZI with the path way difference ΔL of 50 µm was integrated in the WINS-device, as shown in Figure 3.13a. The CNT-emitted light on the way to the coupler grating *C2* propagates along the waveguide, splits equally in the bifurcation (Figure 3.13b), passes the MZI, gets recombined at the output port and scatters out in the free space. Figure 3.14a shows the spectrum of this light, spatially resolved along the y-axis, the *C2*-location is marked with the dashed lines. The interference of the light leads to distinctive intensity modulation in the coupler spectrum.

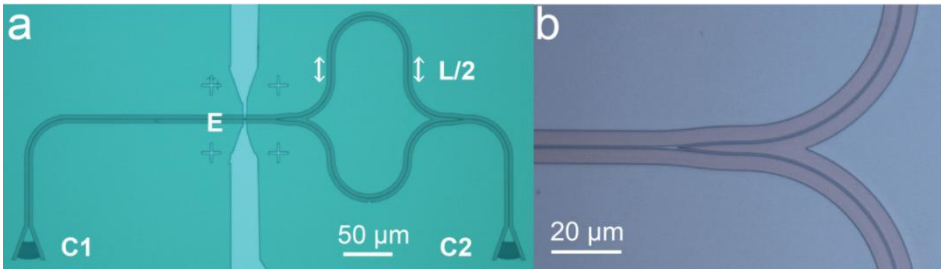

Figure 3.13 | On-chip Mach-Zehnder interferometer.

(a) Optical micrograph of a MZI-device. The waveguide in between the CNT emitter *E* and the coupler grating *C2* is split into two arms with a path difference of $\Delta L = 50\,\mu m$. The total waveguide length between *C1* and *C2* is $640\,\mu m$ and $640\,\mu m + \Delta L$, respectively.
(b) Optical micrograph of the 50/50 splitting element at higher magnification.
Adapted with permission from (10).

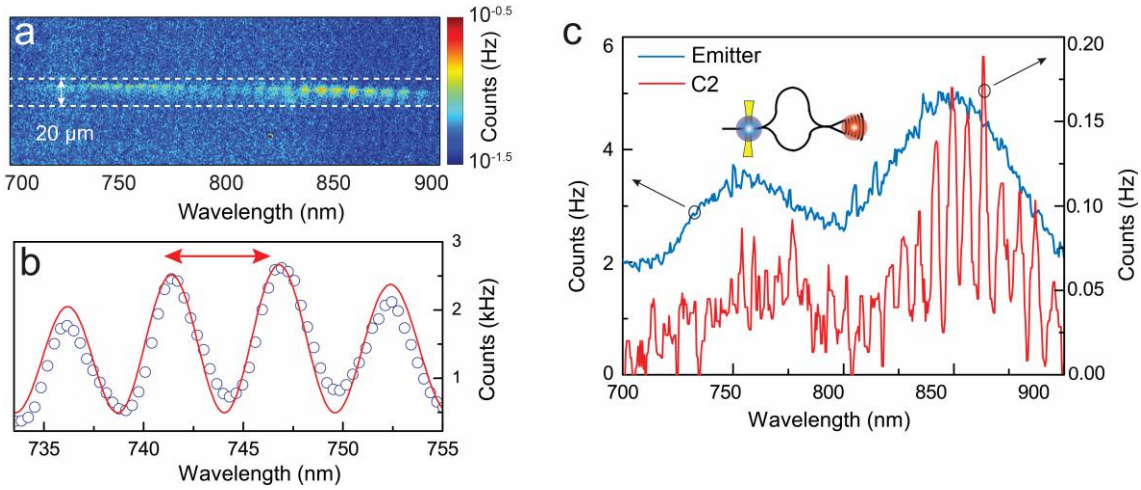

Figure 3.14 | Spectral characteristics of CNT-based Mach-Zehnder interferometer.

(a) CCD-camera image with combined spectral and spatial information of light emitted from the CNT (*E*), after passing through the MZI and the coupler grating *C2*. The dashed lines mark the position of *C2* in the y-direction and the MZI-induced intensity oscillations.
(b) Transmission spectra of a complete MZI-device measured with an external supercontinuum light source. The red line is a fit to the data. An arrow indicates Δλ (FSR).
(c) Comparison of CNT emission spectra recorded at *E* (blue curve) with spectrum recorded at *C2* after passing through the MZI (red curve, integrated intensity from (a)).
Adapted with permission from (10).

The integrated spectra recorded at the emitter *E* and at coupler *C2* show the long-wave modulation because of the back-reflection from the substrate (Figure 3.14c). The short-wave intensity modulation occurred only in the *C2*-spectrum, which is induced by the MZI due to the interference of light within the waveguide along the surface. The same oscillation was observed in the transmission spectrum of the device, measured with an external light source (Figure 3.14b). The periodicity of the modulation Δλ, also known as free spectral range (FSR), fits very well to the predicted value

$$\Delta\lambda = \frac{\lambda^2}{\eta_g(\lambda)\,\Delta L} \quad (135) \qquad (3.10)$$

Thus, at 850 nm with the group refractive index of the waveguide $\eta_g(850nm) = 1.964$ (Appendix A), $\Delta\lambda = 7.4\,\text{nm}$ (10) that is very close to the observed period of about 7 nm.

The analytically calculated FSR (Equation 3.10) is plotted in Figure 3.15 along with experimental values obtained using on-chip waveguide-coupled CNT emitter and the

external light source. The measured and calculated data are in a good agreement with each other. This attests CNT as suitable light source for on-chip nanophotonic experiments.

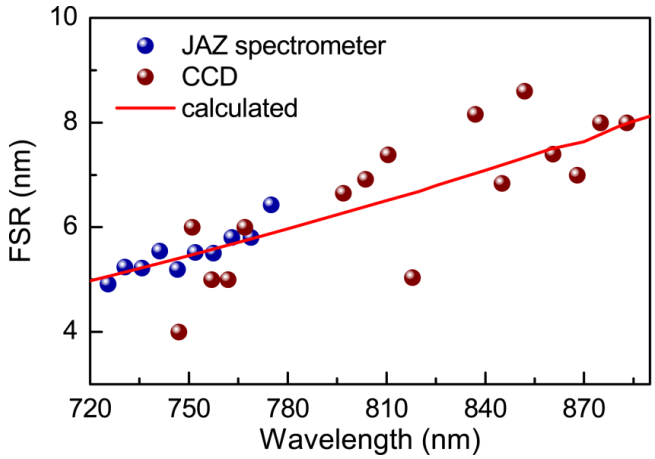

Figure 3.15 | Measured and calculated FSR.

FSR versus wavelength extracted from the data shown in Figure 3.14b,c along with the FSR-value calculated according to Equation 3.10 (red line).
Adapted with permission from (10).

3.5.2 Directional Coupling

Another example of NPIC-components working in combination with CNT-based light emitter is directional coupler (DC, (132)) shown in Figure 3.16a. This structure is used for lossless wavelength-dependent power splitting that allows to tailor the properties of CNT emitter in combination with optical signal processing on a chip.

The field of the electro-magnetic wave decays exponentially with the distance to the waveguide walls. The light propagating in one waveguide partially evanescent couples into the second one, if it is close enough. This effect allows effective wavelength-dependent optical power splitting. Here two-channel DCs consisting of two parallel singlemode identical waveguides were used (11). A supermode, which emerges in the interaction volume of the DC, cyclically transfers the light intensity from one waveguide into another.

The supermode is determined by the effective mode indices $n_{eff,even}$ and $n_{eff,odd}$. These values depend on diverse material and geometrical parameters and are mostly fixed due to the established fabrication process, so that only the distance between the waveguides can be changed. The gap size of 250 nm was chosen to realize compact DC-structures with reproducible properties. For this fixed geometry $n_{eff}(\lambda)$ of DC-supermode was calculated by R. Fechner using COMSOL-software (11) as shown in Figure 3.17.

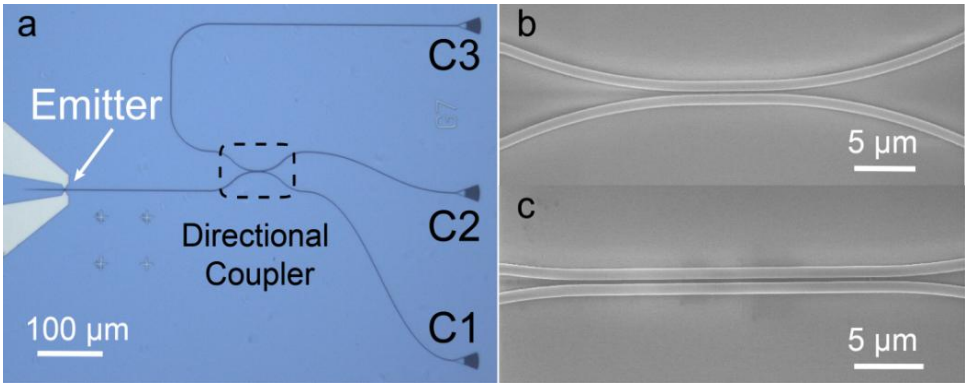

Figure 3.16 | Directional couplers with WINS.

(a) Optical micrograph of device with electrode pair *E* and two evanescent coupled waveguides with coupler gratings *C1*, *C2*, *C3*.
(b,c) SEM of tilted DCs with 5 µm and 21 µm interaction lengths L_i (all fabricated waveguides are 625 nm wide and 130 nm high).
Adapted with permission from (11).

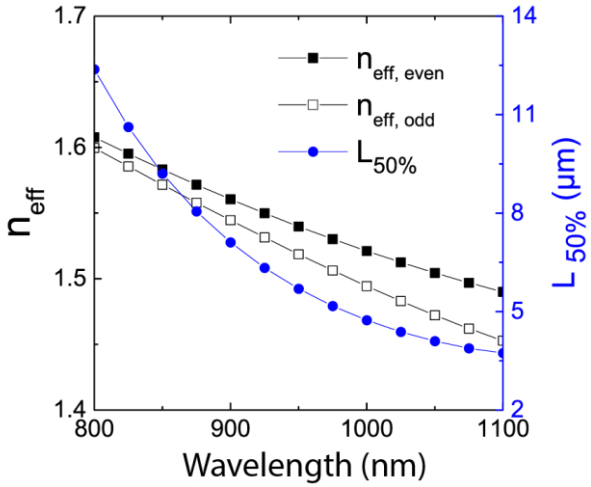

Figure 3.17 | Effective refractive indices of DCs.

Simulation of effective supermode indices $n_{eff}(\lambda)$ and interaction length $L_{50\%}(\lambda) = 0.5\, L_C$ of a DC. Adapted with permission from (11).

The crucial characteristic of DC is the percentage of light coupled in to the neighboring waveguide, called coupling efficiency $\eta_{DC}(\lambda) = \frac{I_{coupled}(\lambda)}{I_{coupled}(\lambda) + I_{direct}(\lambda)}$. The intensities of direct propagated light I_{direct} and of coupled light I_{couple} are measured at the corresponding grating couplers (Figure 3.16a). For the DC with interaction length L_i

$$\eta_{DC}(\lambda) = sin^2\left(\frac{L_i}{\lambda}\,\pi\left|n_{eff,even} - n_{eff,odd}\right|_{n_{material}}\right) = sin^2\left(\frac{\pi}{2}\,\frac{L_i}{L_c}\right) \qquad (3.11)$$

100% of the light couples from the first into the second waveguide, if the L_i is equal to the coupling length $L_c = \frac{\lambda/n_{material}}{2*|n_{eff,even} - n_{eff,odd}|}$ or multiple of it.

For this work primarily the CNT-based devices with 50/50 splitting, i.e. $\eta_{DC} = 0.5$ are of interest. MeCNTs are used as thermal broadband light sources with increasing intensity towards higher wavelengths. Considering the limits of detector sensitivity, the targeted wavelength range is 950 nm to 1000 nm with the corresponding

$$L_{50\%} = 0.5\, L_C\,(975\,nm) \approx 5\,\mu m \text{ (Figure 3.17)} \qquad (3.12)$$

The scope of Equation 3.12 is limited among others due to the fabrication imperfections especially for longer DCs. For that reason pairs of identical DC-devices connected via MZ-interferometers were tested (see Appendix C and (11)). Transmission

measurements provide information about performance of different long DCs, allowing the precise calculation of η_{DC}. Following the simulation, the DCs with the lengths L_i of 5 µm and 21 µm were determined as suitable for 50/50 splitting in the range of 950 nm and 1000 nm.

After the optimal parameters of DC-components had been found, the power splitting WINS-devices were fabricated (Figure 3.16a). A device comprises two waveguides linked by DCs of different lengths (Figure 3.16b,c) and terminating either by grating couplers (*C1*, *C2*, *C3*) or by electrodes bridged with the MeCNT emitters shown in Figure 3.18a. The power splitter has two possibilities of signal inputs. One input allows the CNT-emitted light to couple into the waveguide, pass the DC and to be read out via a free-space spectroscopy and imaging setup. In contrast, grating couplers allow for external laser light to propagate inside the main waveguide of a device and couple out to a spectrometer via optical fiber array. An additional advantage of the presented design is given by the placement of CNTs aside from the main waveguide, eliminating any impairment of transmission through the device due to CNT deposition.

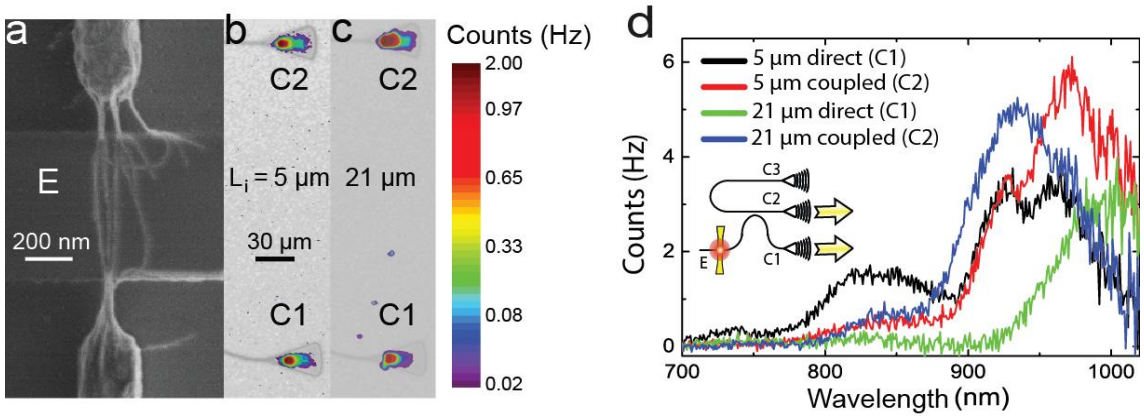

Figure 3.18 | Emission measurements performed with power splitting WINS-devices.

(a) SEM of the central part *E* with the metallic CNTs on top of the waveguide between two metal contacts.
(b,c) High-resolution CCD camera images of the light emission observing on the coupler gratings *C1* and *C2*; superimposed with grayscale images of the samples with L_i of 5 µm and 21 µm.
(d) CNT emission spectra simultaneously measured at *C1* and *C2* for the devices with 5 µm and 21 µm long coupling lengths (compare with Figure 3.19).
Adapted with permission from (11).

Similarly to the previous experiments, electrically driven emission measurements were performed in the free-space setup. As schematically shown in the inset of Figure 3.18d, the CNT-emitted incandescent light couples into the waveguide and passes on the way to the grating coupler *C1* the directional coupler. The DC splits the propagating light depending on L_i and wavelength, so that it partly evanescently couples in to the neighbouring waveguide and scatters out at *C2*. The relative integral intensity of light measured at *C1* and *C2* varies from device to device depending on L_i. Structures with short DCs demonstrate nearly equal emission intensity at both couplers (Figure 3.18b). On the contrary, for the devices with $L_i = 21\,\mu m$ the intensity of the coupled light (*C2* in Figure 3.18c) is much stronger compared to the direct propagated light (*C1*). Consistently, the spectral measurements performed on couplers reveal, in the case of longer DC, the superiority of the coupled light to the directly propagated light almost over the entire measurement range (Figure 3.18d). The simultaneously recorded spectra are typical for thermal emission with intensity modulation due to the interference on substrate, similar to the previous measurements (Subsection 3.4.1). The interrelated spectral curves (black and red, green and blue) cross each other in the desired wavelength range.

Additionally the devices were characterized in the fiber-coupled transmission setup. The external light is coupled in to the structure at *C3*, while the transmitted spectra of both the directly propagated and coupled light are collected at *C2* and *C1* respectively (Figure 3.19a). The spectral profiles, measured in both setups, look similar. The Gaussian-shaped form of transmission spectra is caused by the grating coupler. Moreover, due to its small numerical aperture the transmission intensity and the accessible wavelength range are significantly smaller than those in the free-space setup.

The measured transmission and emission spectra are used for the calculation of η_{DC}. The extracted efficiencies fit well to each other both for short and long DCs (Figure 3.19b). While the progression of $\eta_{5\mu m}$ and $\eta_{21\mu m}$ reveals significant differences, the 50/50 splitting in the both cases occurs at the targeted wavelength of about 975 nm.

Therefore, the integrated CNT light sources in combination with DC-components demonstrate highly reproducible performance. The results in emitter mode are

comparable with the transmission measurements with the advantage that without fiber-optics and grating couplers the losses are lower and the accessible wavelength range is much broader. Since the chosen operating wavelength range of DCs matches the excitonic transitions of (6,5)-CNTs (40), the device can be used as a convenient platform for measurements in the narrow-band SCCNT emission regime, providing a basis for correlation experiments for the characterization of a single-photon source. In general, the presented design emerges as a fundamental building block for hybrid CNT-nanophotonic components such as narrow classical or/and quantum chip-integrable CNT emitters.

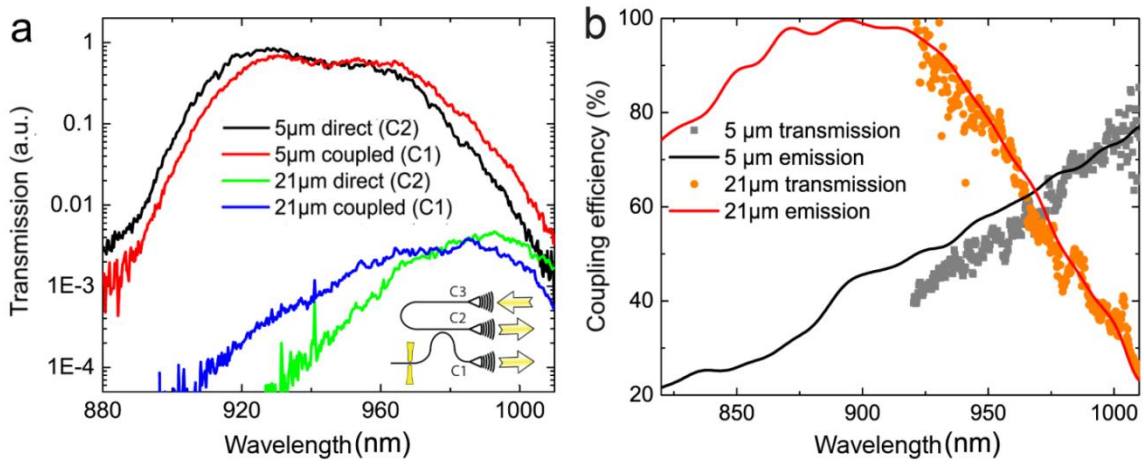

Figure 3.19 | Transmission spectra and coupling efficiency of power splitting WINS.

(a) Transmission spectra of complete structures measured between *C3* and *C2*, *C3* and *C1* with an external supercontinuum light source. The difference in transmission between 21 µm and 5 µm is due to the lower efficiency of detector at higher wavelengths.

(b) Coupling efficiency η_{DC} calculated from the data measured for 5 µm and 21 µm long devices in transmission and emission modes.

Adapted with permission from (11).

3.6 CNT as Narrow-Line Light Emitter

3.6.1 Photonic Crystal Nanobeam Cavity with Integrated CNT

Nanophotonic devices with narrow-line emission spectra are highly attractive for applications in telecommunication, sensing and optomechanics due to improved performance and enhanced light-matter interaction. The incandescent WINS-devices demonstrated in the previous sections reveal broadband emission. Furthermore, even electroluminescent SCCNTs integrated into short-channel devices typically have rather broad spectral maxima with 50 to 200 nm (49,53,126,127). Fortunately, the emission properties of nanoscale light sources can be tuned by adjusting the nanophotonic environment (136–143). In particular, the one-dimensional photonic crystal nanobeam cavities (PCNBCs, (144–146)) with a high quality factor Q for Purcell enhancement and a small mode volume appear to be predestined for integration of CNT light sources. In the scope of this thesis, the electrically driven WINS-devices in PCNBCs with exceptionally narrow linewidths in the 1 nm range were demonstrated for the first time (12).

In comparison to a standard WINS-device, the presented structure comprises an etched PCNBC in the middle part of a purple-colored waveguide between metal contacts (in yellow), as schematically shown in Figure 3.20a. A CNT emitter is suspended across the electrodes in the center of the PCNBC (Figure 3.20b). The essential advantage of the novel PCNBC structures consists in the strong influence on the spectral properties of the emitted light due to the signal modulation in the photonic cavity. Periodic photonic crystal holes (PCHs) in the nanobeam form a photonic bandgap. The distribution of the electric field in a PCNBC can be tuned by variation of size and arrangement of PCHs. The quality factor Q of a PCNBC increases with the number of PCHs, N_{PCH} (for details to simulation of PCNBC see Appendix D). There are two alternative PCNBC designs compared in this study. In the case of dielectric mode cavity the maximum of the electric field is inside the dielectric nanobeam, these devices have bigger PCHs in the central part of PCNBC. In contrast, air mode cavities have the field maxima inside the central PCHs, which are smaller as the outer holes.

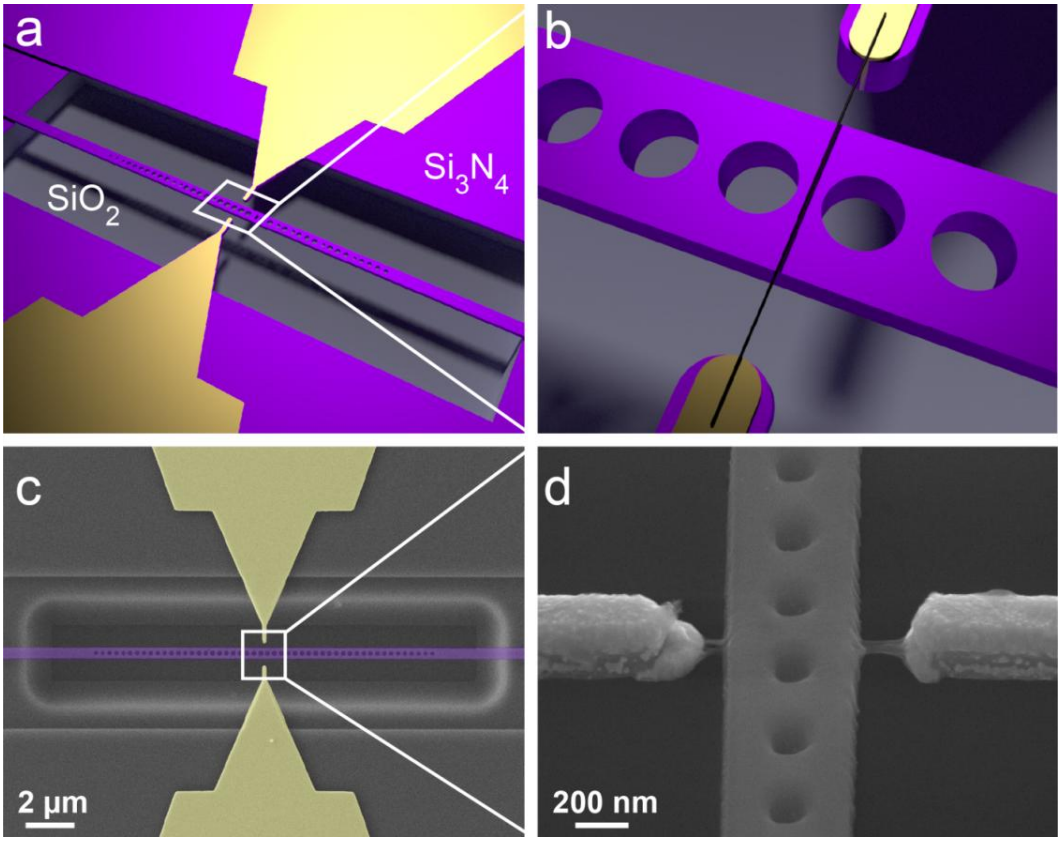

Figure 3.20 | PCNBC device with coupled CNT light emitter.

(a) Schematic view of the multilayer device structure consisting of two metal electrodes (yellow) and a photonic waveguide (purple). The photonic waveguide was etched into the Si_3N_4 layer. Its central part was underetched into the SiO_2 layer to a depth of 1.5 µm and PCHs were formed.
(b) Schematic close-up of the cavity center illustrating the CNT (black line) in contact with the Au/Cr metal electrodes on top of the Si_3N_4 waveguide. The width of the waveguide was 0.6 µm for all devices, the gap between metal electrode and waveguide varied between 0.2 µm and 0.4 µm. The number of PCHs amounted to 40 or 50 depending on the device.
(c) False-colored SEM images of the central part of the device, showing the PCNBC structure between two metal electrodes. The cavity center matches exactly the midpoint between the two electrode finger tips.
(d) SEM image of the cavity center with two metal electrodes and a photonic waveguide, bridged by several single-walled CNTs (device 1). The air-suspended part of the CNTs is clearly visible, while the material contrast on the waveguide top is too low to resolve the CNTs. Tilt angle 45°.
Adapted with permission from (12).

PCNBCs and grating coupler were considered for operation at the wavelengths of around 980 nm. This wavelength range was chosen in order to match both the radiative transition of (6,5)-SCCNTs and the efficiency maximum of thermal emission within the sensitivity range of the Si-detector. The design of the cavity promotes the coupling of the CNT-emitted light into the waveguide as well as the signal enhancement due to the PCNBC. CNTs have tiny absorption cross section and does not disturb the cavity resonance (100). The influence of the metal electrodes on the cavity modes is more

significant due to the radiation damping and scattering of the light at the electrode fingers (see Figure 3.26). As the electrode gap width is limited by the lengths of deposited CNTs, a separation of up to 1.4 µm was used. This corresponds to the maximal electrode-waveguide distance of 0.4 µm for a 0.6 µm wide waveguide. The nanobeam with PCHs is suspended in air in order to increase the refractive index contrast between the waveguide and the substrate, and thus the confinement quality of the PCNBC.

The fabrication of PCNBC-structures is shown in Figure 3.2 and is described in full detail in Appendix B. Additionally to the lithography steps required for fabrication of a standard WINS-device, here the cavity with the suspended waveguide and PCHs was formed using wet etching technique. In Figure 3.20c,d SEM images of a PCNBC are shown, while the complete device is demonstrated in Figure 3.21a. The complex geometry of PCNBC with suspended perforated nanobeam makes the dielectrophoretical deposition of CNTs between metal contacts more demanding in comparison to standard WINSes. CNTs tend to pull down into PCHs during the drying step. This effect is especially pronounced in dielectric mode cavities with larger central holes. Since the attracting dielectrophoretic force $\langle F_{DEP} \rangle$ is stronger in the case of highly polarizable MeCNTs (Section 2.4.2), they were deposited onto dielectric mode cavities, while SCCNTs from suspension S2 were placed onto air mode cavity devices.

The emission measurements were performed in the free-space setup. In Figure 3.21b a color-scale CCD image demonstrates the spatial intensity distribution of the CNT-emitted light, overlapped with the grayscale image of the PCNBC structure. Similarly to the measurements on standard WINSes (Figure 3.7), bright spots between the metal contacts and at the grating couplers are observed. A more detailed heat map of the CNT light source E is shown in Figure 3.21c. At higher magnification a low-intensity broadening of the emission signal along the nanobeam becomes visible. The comparison of the integral emission intensities at the central spot I_E and at the couplers I_C allows for calculation of full-bandwidth coupling efficiency for PCNBC devices $\eta_{coupling} \approx 10 \ldots 30\%$ (Equation 3.8). This value is lower than the typical WINS-efficiency of around 45% (Subsection 3.4.2). As demonstrated below, in contrast to the standard WINSes, the coupling into the PCNBC is wavelength-dependent with a significant enhancement at cavity resonances and strong suppression at the other wavelengths.

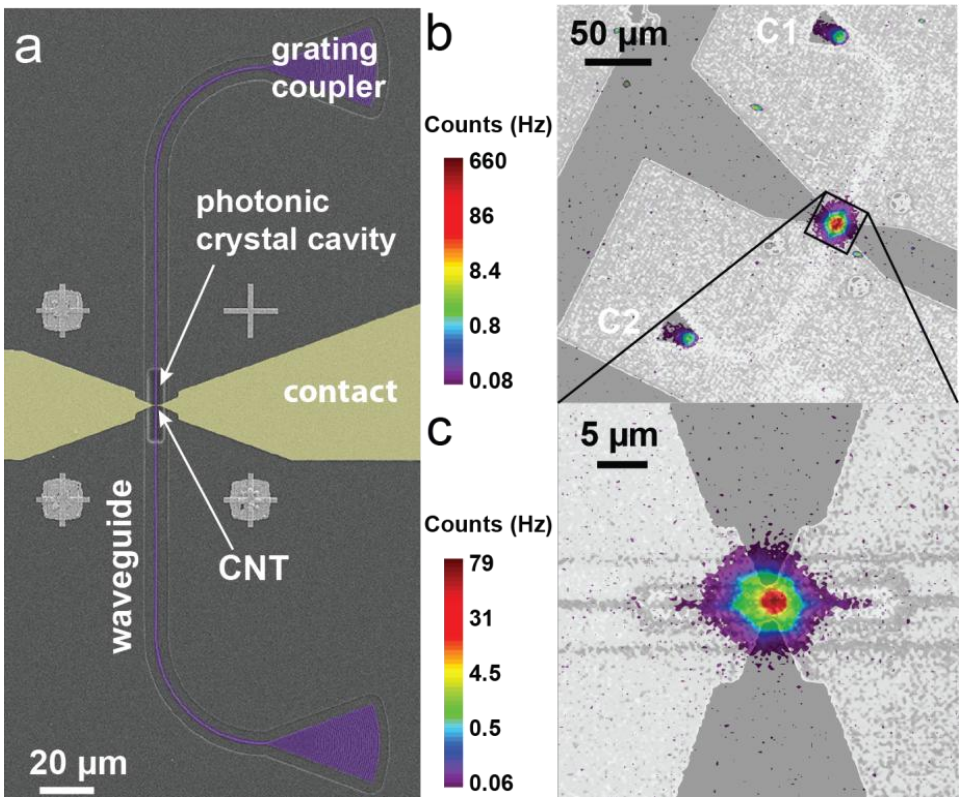

Figure 3.21 | Light emission from a CNT-coupled PCNBC device.

(a) SEM image of the PCNBC device, showing the extended photonic waveguide with two terminating grating couplers separated by 250 µm between two metal electrodes.
(b) CCD-camera image of the device under direct voltage. Light emission is observed from the CNT emitter and from the terminating coupler gratings, both connected with the emitter via the waveguide. Superimposed is a grayscale image of the sample under external illumination to reveal the position of the electrodes.
(c) CCD-camera image of the cavity in the central part of the device. Light emission from the CNT and scattering of the emitted light on PCHs along the waveguide is observed. Superimposed is a grayscale image of the sample.
Adapted with permission from (12).

The waveguide structures designed in the scope of this thesis typically had symmetrical geometry so that the CNT-emitted light coupled and propagated along the waveguide equally in both directions, with nearly identical signal intensities at the couplers $I_{C1} \approx I_{C2}$ (Figures 3.7 and 3.21b). However, with asymmetrical PCNBC a monodirectional light propagation can be realized. As shown in Figure 3.22a, in such a device almost no light reaches the top coupler, I_{C1} is about 10 times lower than I_{C2}. It is explained by the fact that the light reflects almost completely on PCHs in the longer part of the cavity, as demonstrated in the corresponding FDTD simulation of the fundamental mode (Figures 3.22b,c). In this way, just by using unequal number of PCHs a strong mirror inside the waveguide can be realized.

However, PCNBC devices can be used for the tuning of the transmitted and emitted light in a more subtle way. In the following the selection of the desired emission wavelength from the CNT spectrum combined with the intensity enhancement using symmetrical PCNBC devices is demonstrated.

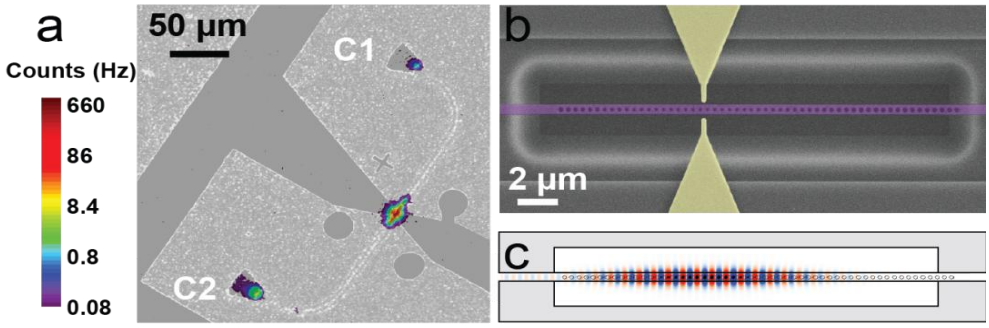

Figure 3.22 | Light emission from a CNT-coupled mirror PCNBC device.

(a) CCD-camera image of the asymmetrical PCNBC device under electrical bias. The CNT-emitted light couples into the waveguide and propagates mostly to the bottom coupler due to the reflection off the photonic crystal mirror.
(b) SEM of the central asymmetric part of the PCNBC device with 20 PCHs to the left and 35 PCHs to the right of CNT light source.
(c) Mode profile of the fundamental mode for the mirror structure. Light reflects on PCHs in the longer right part of the cavity and propagates in the shorter, left part of the waveguide.
Adapted with permission from (12).

3.6.2 Dielectric Mode Cavity Devices

In the scope of this thesis dozens of air and dielectric mode PCNBC devices with fundamental resonance wavelengths in the range of 975 nm to 1050 nm were characterized, tuned by small adjustments to the PCNBC geometry. An overview of fabricated devices is given in Figure D.3 in Appendix D. Here three sets of spectra for each device type are exemplarily presented: sim1 and devices 1,2 for air mode cavity (Table 3.2) as well as sim2 and devices 3,4 for dielectric mode cavity (Table 3.1). The simulations were performed for cavity design that contained fewer PCHs than the actual devices (24 or 30 instead of 40 or 50) due to limitations in computational power. This reduction decreased the Q factors of the maxima, but barely affected the spectral locations of resonance wavelength (Appendix D, Figure D.2a,b).

Device	**N_{PCH}**	**Gap, µm**	**1. mode (nm)**	**2. mode (nm)**	**3. mode (nm)**
Simulation2	30	-	984	1,002	1,021
Device3 (e3)	40	0.3	987/973/978	1,002/988/989	1,015/1,001/1,003
Device4 (f4)	50	0.4	990/977/979	1,001/987/988	1,012/997/998

Table 3.1. Dielectric mode cavity.

PCNBC devices differ in mode type, N_{PCH}, gap between metal contact and waveguide as well as position of resonant modes (green – simulated values, black – measured transmission, red – measured light emission).

The simulated and measured spectra from the dielectric mode cavities with deposited MeCNTs are shown in Figure 3.23. The normalized transmission spectrum for the device sim2 in Figure 3.23c illustrates the simulated response of a dielectric mode reference cavity with N_{PCH} = 30 to a broad electromagnetic pulse as obtained from FDTD simulations. The fundamental mode 1s was designed for 980 nm, the second order mode 2a for 1000 nm and a number of higher order modes are visible at longer wavelengths, which then blend into the continuum of guided modes below the dielectric band edge (for details see Figure D.1d in Appendix D). Strong transmission peaks provide a high coupling efficiency from the dielectric mode cavity into the waveguide. The number in the modes label indicates the mode order (1-5) while the letter indicates

whether the mode profile is symmetric (s) or asymmetric (a) with respect to the cavity center. Field distribution for the 1s and 2a mode profiles is shown in Figure 3.23a,b.

The transmission spectra of the devices 3 and 4 (Figure 3.23d,e) demonstrate pronounced narrow-line maxima close to the designed wavelengths in qualitatively agreement with the simulation. The deviations between the exact positions of designed and measured resonances (Table 3.1) are caused by the uncertainties about the refractive index and the thickness of the cavity after wet etching. The transmission spectra are enveloped by the Gaussian profile of the grating coupler. Furthermore, the fundamental modes in the measured spectra were strongly suppressed because of the influence of the metal electrodes. Since the fundamental mode provides a field maximum at the cavity center (Figure 3.23a), evanescent coupling to the nearby metal contacts leads to substantial optical loss.

Significant differences in the PCNBC spectra are expected when the device is operated in emission regime. The coupling of a cavity to the CNT emission can be described in terms of the local density of states (LDOS) (147). Since LDOS is a function of space and frequency, the interaction between cavity and dipole-like CNT emitter depends on the CNT location and its spectrum. For dielectric cavities with the large central PCHs the misaligned CNTs are pulled into the holes by capillary forces and form no electric contact. Therefore, only axial aligned CNTs can be deposited and bridge the electrodes. Figure 3.23f illustrates the simulated LDOS spectrum of the sim1 normalized with respect to a simple waveguide, for two different emitter locations on top of the waveguide (solid line) and at the outer waveguide edge (etched line). The spectra demonstrate similar profile, but the enhancement is significantly stronger if the emission takes place in the center of the PCNBC. Comparing Figure 3.23f to Figure 3.23c, even order peaks are not observed in the LDOS spectrum, because the odd symmetry of the corresponding cavity modes leads to a field node with zero field values at the cavity center as shown in Figure 3.23b.

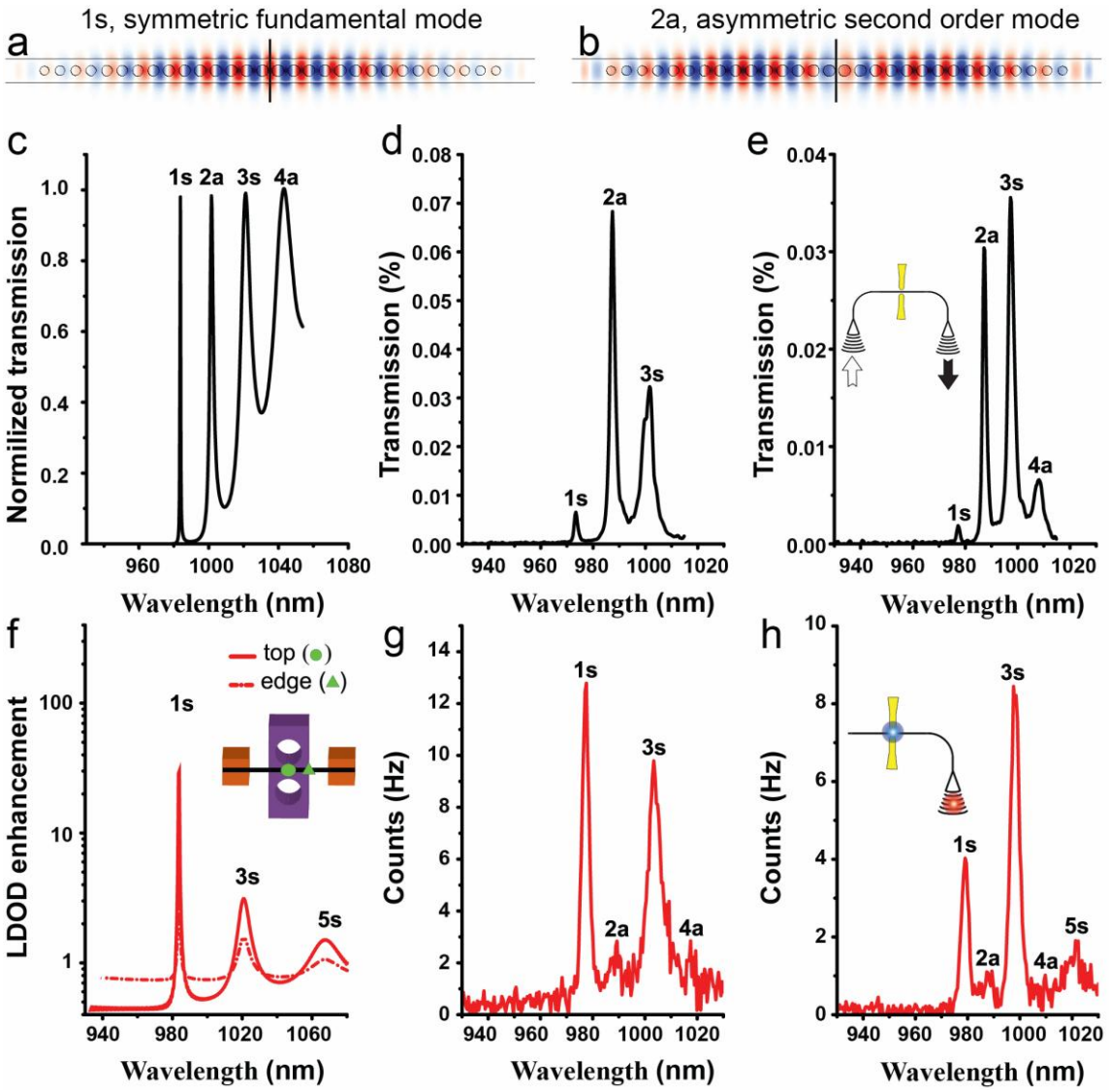

Figure 3.23 | Transmission and emission spectra of CNT-based dielectric mode PCNBC.

(a) Mode profile of the fundamental mode (even symmetry) for dielectric mode cavity.
(b) Mode profile of the second order mode (odd symmetry) for dielectric mode cavity.
(c) The simulated transmission spectrum for the device sim2.
(d,e) The experimentally recorded transmission spectra for the devices 3 and 4, respectively.
(f) The simulated normalized intensity enhancement for the light emission on top (line) and edge (dash dot) of PCNBC for the device sim2. The inset shows the position of the CNT for both cases.
(g,h) The spectra of electrically driven CNT sources recorded at grating couplers for the devices 3 and 4, respectively (compare with d and e).
Adapted with permission from (12).

Figure 3.23g,h demonstrates emission spectra of electrically driven CNTs recorded at grating couplers. In contrast to the standard WINSes with broadband incandescent emission modulated with substrate interference, the spectra show narrow-line maxima at the same positions as the corresponding transmission spectra described above. However, the odd resonance modes are enhanced and the even resonance modes suppressed in agreement with the LDOS simulations. These spectra illustrate the key result of this section, as for the first time a carbon based electrically driven narrow-line light source with an arbitrary designed emission wavelength was realized.

3.6.3 Air Mode Cavity Devices

The performance of air mode cavity devices with deposited SCCNTs was studied in a similar way. The spectral characteristics of this second type of PCNBC structures are presented in Figure 3.24 and Table 3.2. Figure 3.24c demonstrates the simulated transmission spectrum of the reference structure sim1 with the fundamental mode 1a located close to 980 nm similar to the sim2. However, in this case the band gap stretches to higher wavelengths. The transmission of the fundamental mode reaches only up to 52% due to the lower coupling efficiency into the waveguide. The recorded transmission spectra from devices 1 and 2 shown in Figure 3.24d,e are also weaker compared to the dielectric mode cavities (Figure 3.23d,e). Nevertheless, the cavity resonances are just as narrowband. While the fundamental mode is suppressed similar to Figure 3.23d,e, the higher order modes are clearly visible in the transmission spectra. In particular the 2s resonance mode dominates the transmission spectra of both devices.

Figure 3.24f depicts the LDOS spectra of the air mode cavity for two different CNT locations schematically shown in the inset. An aligned CNT emitter in the center of the waveguide strongly couples only to the second order resonance 2s, because the fundamental mode 1a has a field node at the cavity center (Figure 3.24a). For the same reason the deposition of a CNT emitter at the center of the first small PCH, in the position of the highest intensity antinode of 1a, results in a pronounced fundamental resonance in the enhancement spectrum. Therefore, a shift of the emitter location from the symmetry plane leads to stronger peaks at the even symmetry resonances and weaker odd symmetry maxima. This is to be expected in experiment with air mode

cavities, since CNTs are most likely not perfectly aligned along the cavity center due to the capillary forces dragging tubes towards holes.

The recorded emission spectra shown in Figure 3.24g,h are almost identical to the corresponding transmission spectra and in contrast to the dielectric cavities no maxima are missing here. Considering the LDOS simulations, either several light emitting CNTs were located both in the cavity center as well as at the center of the first PCH or a single CNT was deposited in the intermediate position. The emission linewidths are close to the spectral resolution of the spectrometer (1.3 nm) and hence more than an order of magnitude narrower than the linewidths of electrically driven CNTs ever measured (51,53,63,64,108,127). Also in the case of air mode cavities no typical signatures of EL or incandescence were observed in the measured spectra. The light emitting characteristics of both cavities were determined entirely by the PCNBC structure and could be tuned over a wide range of resonance frequencies by the photonic crystal geometry.

Device	**N_{PCH}**	**Gap, µm**	**1. mode (nm)**	**2. mode (nm)**	**3. mode (nm)**
Simulation1	24	-	973	951	927
Device1 (c5)	40	0.2	985/978/988	970/966/969	958/953/955
Device2 (g1)	40	0.3	965/961/962	950/944/945	938/932/933

Table 3.2. Air mode cavity.

The positions of resonant modes of presented PCNBC devices
(green – simulated values, black – measured transmission, red – measured light emission).

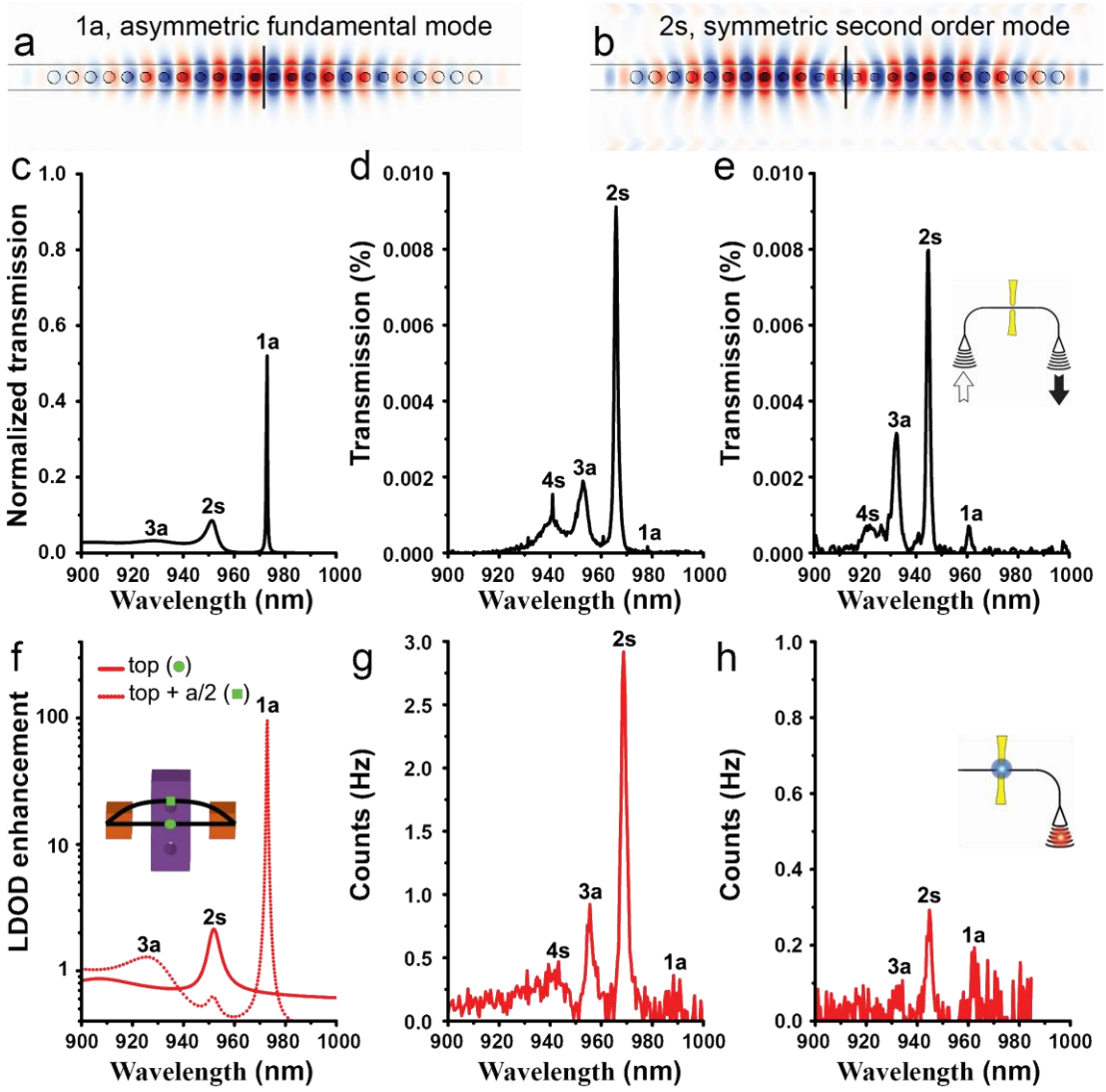

Figure 3.24 | Transmission and emission spectra of CNT-based air mode PCNBC.

(a) Mode profile of the fundamental mode (odd symmetry) for air mode cavity.
(b) Mode profile of the second order mode (even symmetry) for air mode cavity.
(c) The simulated transmission spectrum for the device sim1.
(d,e) The experimentally recorded transmission spectra for the devices 1 and 2, respectively.
(f) The simulated normalized intensity enhancement for light emission at the cavity center (red line) and over PCH (red dots) for the device sim1. The inset shows the position of the CNT for both cases.
(g,h) The spectra of the electrically driven CNT sources recorded at grating couplers for the devices 1 and 2, respectively (compare with d and e).
Adapted with permission from (12).

3.6.4 Cavity Spectra and Role of Metal Electrodes

The only significant discrepancy between the simulation and the measurement was the lower intensity of the fundamental mode in the most of transmission and emission spectra recorded at grating couplers. However, this resonance was observed in the spectra of CNTs measured directly on the cavity center as shown in Figure 3.25a. Emission spectra measured on the dielectric mode cavities typically also reveal a number of higher order modes, albeit weaker than the first one. The effect was less pronounced for devices with wider electrode gap, as the resonance peaks in the cavity spectra appeared due to the scattering of the light at the electrodes. The fundamental mode has its field intensity concentrated in the cavity center (Figures 3.23a and 3.24a) and most of the mode energy radiates away into the surroundings of the cavity, leading to a clear resonance in the cavity spectrum. In contrast, the higher order modes are less affected by the scattering at the electrodes.

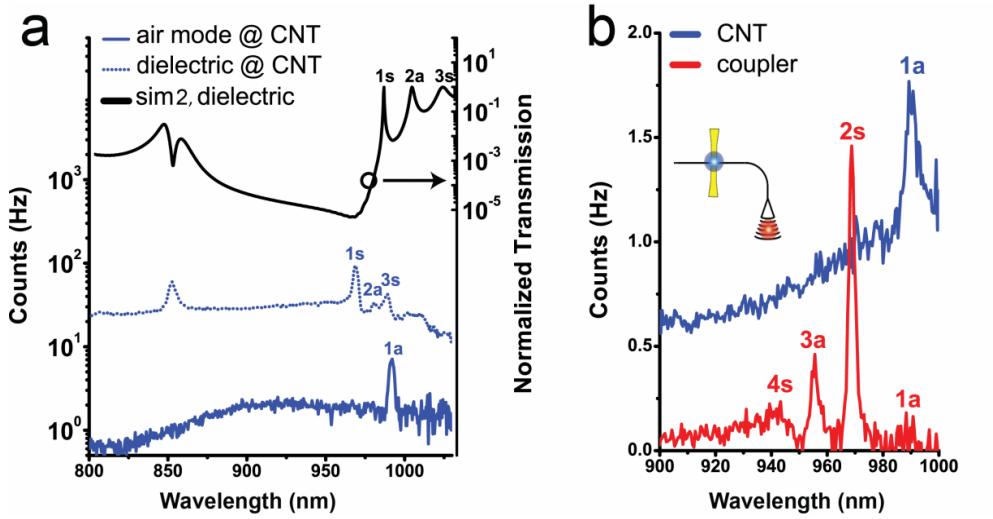

Figure 3.25 | CNT emission inside PCNBC.

(a) Comparison of CNT emission spectra recorded at the cavity centers of dielectric (blue line) and air mode (blue dots) devices. The air mode cavity spectrum has only one maximum 1a corresponding to the fundamental mode. In contrast, the spectrum of the dielectric mode cavity shows multiple resonances as well as the bandgap edge maximum at 850 nm, similar to the simulated transmission spectrum for the device sim2 (black line).
(b) Comparison of CNT emission spectrum at the cavity center (blue) with the spectrum recorded at the grating coupler (red) for the air mode cavity (device 1). The first resonance mode 1a is only clearly visible in the CNT emission spectrum.
Adapted with permission from (12).

The cavity spectra exhibit a broadband background at shorter wavelength between 600 nm to 950 nm, which is not observed in the case of the coupler emission. The cavity center is fully suspended and thermally decoupled from the substrate, so that this background most probably is induced by the heating of the CNT and the cavity. A weak resonance that appears at 850 nm both in the simulated and measured spectra of dielectric mode cavity corresponds to the onset of the air band.

The simultaneously measured intensity spectra of the CNT at the cavity center and at the grating coupler are plotted in Figure 3.25b. The pronounced resonance peak in cavity spectrum with enhancement of 1.5 over the baseline intensity matches exactly to the barely visible fundamental resonance 1a in the coupler spectrum. The 2s coupler resonance compared with the background of cavity spectrum demonstrates the same enhancement factor of 1.5. Taking into account the coupling and propagation losses, an overall enhancement factor of 5 can be conservatively estimated for the 2s mode. Using Equation 3.8, the coupling efficiency for the second order resonance can be calculated with $\eta_{coupling\ ,970\ nm} \approx 75\%$, which is significantly higher than the full-bandwidth coupling efficiency for PCNBC devices. However, the simulated LDOS enhancement for 2s mode of an air mode cavity with 40 PCHs yields a higher enhancement factor of 28. Most probably, the difference is caused by the discrepancy between emission location and cavity center as well as by absorption losses due to the metal contacts.

Electrodes strongly influence the transmission and emission properties of the PCNBC. Since the contacts are metallic and thus highly absorptive, considerable damping of the cavity modes occurs when the two electrode fingers are close to the cavity. Figure 3.26 demonstrates the simulated Q factor = $\lambda/\Delta\lambda$ for variable electrode-waveguide distances for both cavity types with N_{PCH} = 50. The Q factor of the fundamental mode increases exponentially with electrode-waveguide separation. At a minimal distance of 0.2 μm it is therefore reduced by almost two and three orders of magnitude for the dielectric and air mode cavities, respectively, compared to the situation with no electrodes. For such a small separations the Q factor of the fundamental mode becomes even smaller than the Q factor of the corresponding second order mode, because the electric field strength of the latter is concentrated away from the cavity center (Figures 3.23a,b and 3.24a,b). As the choice of the electrode gap was limited by CNT length, the electrode-waveguide separation of up to 0.4 μm was used and consequently radiation damping has to be

taken into account.

An important characteristic of photonic cavity is the stability of light emission in sense of intensity and wavelength. While the first parameter is common with the previous devices and depends primarily on CNT properties and experiment conditions, the variation of peak wavelength could occur in PCNBC-devices due to the heating of the cavity. For the case where the peak position would change with the voltage neither highly-controllable emission nor high-speed operation in narrow-line regime would be possible for our CNT device. Therefore, it is of prime importance that no variation of the peak wavelength as a function of the voltage neither at the cavity nor at the coupler was observed, as shown in Figure 3.27 for the device 1. The positions of emission maxima depend only on cavity geometry, while the emission intensity was controlled by varying the voltage applied to the CNT.

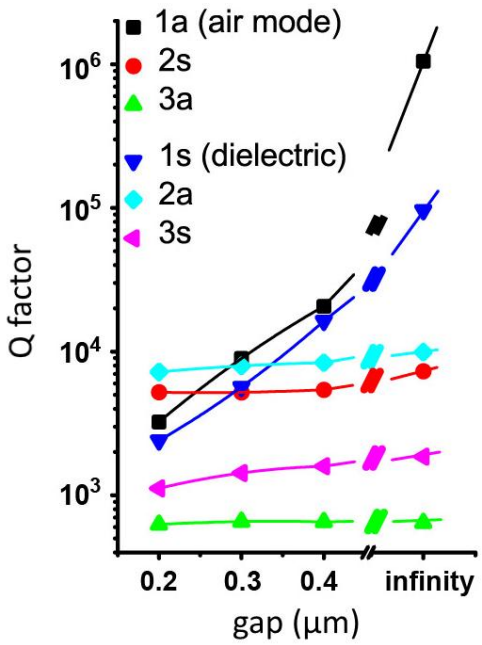

Figure 3.26 | Role of metal contacts in light enhancement.

Plot of the simulated Q factors of air and dielectric mode devices for different electrode-waveguide distances.
Adapted with permission from (12).

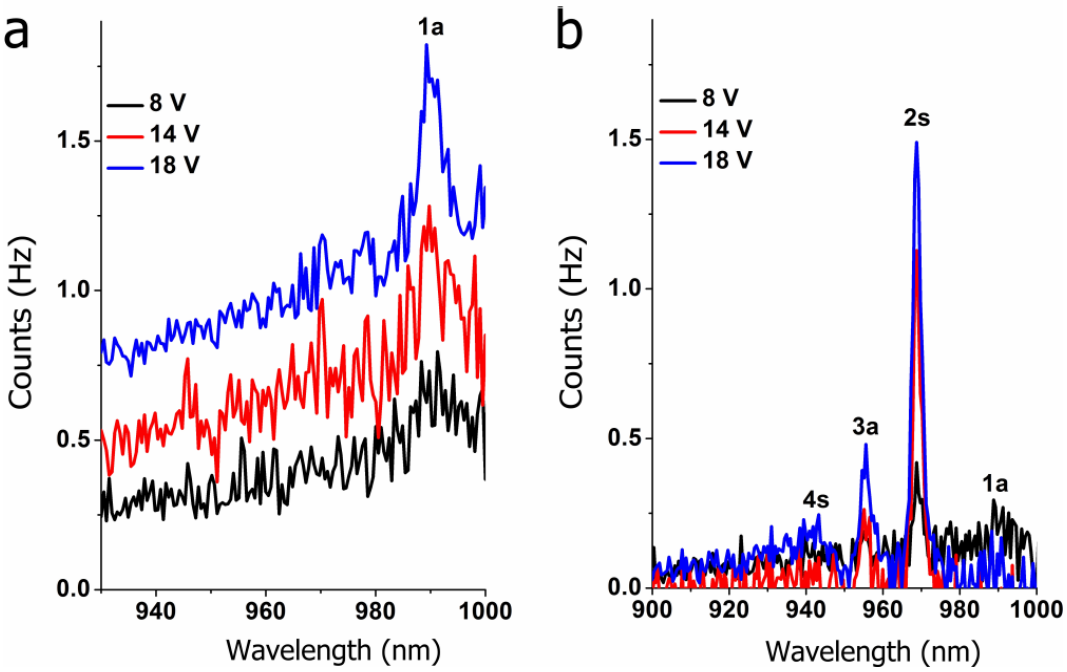

Figure 3.27 | Voltage-dependence of light emission from PCNBC-device.

(a,b) The voltage-dependent spectra of the electrically driven CNT source recorded at the cavity center (a) and the grating coupler (b) for the device 1.
Adapted with permission from (12).

Electrically driven CNTs emerged as applicable light sources for integration into PCNBC devices. CNTs barely influenced emitting wavelength and linewidth of a nanophotonic cavity. On the contrary, the linewidth of integrated CNT emitter was determined solely by the quality factor of PCNBC so that no emission broadening due to temperature and surface interaction was observed. The limited resolution of the spectrometer hindered the precise evaluation of the linewidth, but even with the maximal value of 1.5 nm the presented emitter is at least 10 times narrower than previous reports for electrically-driven CNTs. The demonstrated on-resonance coupling efficiency of around 75% is rather high and can be strongly improved with enlargement of electrode gap. Therefore, presented narrow-line WINSes are suitable for the large-scale fabrication of fully-integrated on-chip light sources with tailored emission wavelength.

3.7 CNT as High-Frequency Light Emitter

3.7.1 Pulsed Measurements in Free-Space Setup

Fast conversion of electrical signals into optical pulses is a great advantage for nanophotonic devices with an embedded light source. However, the majority of experimental studies on emitting properties of CNT-based devices are aimed on static light generation. In particular, electrically driven CNT emission in the time-frequency-domain has not been often investigated.

As was shortly mentioned in Section 2.3.2, CNTs belong to the fastest thermal emitters. Light mass of carbon atoms and strong carbon-carbon chemical bonds determine the exceptionally high thermal conductivity of carbon materials. The expected response time of thermal emission τ_{therm} for the CNTs with diameter of $0.8 \dots 1.2\ nm$ emitting at $1000 \dots 1500\ K$ can be calculated as $\tau_{therm}(T) = \frac{\rho_{CNT} * c_{CNT}(T)}{g(T)}$ (148) $\approx 5 \dots 70\ ps$ with corresponding mass density $\rho_{CNT} = 0.7 \dots 1.8\ 10^{-15}$ kg/m, thermal conductivity across the CNT-axis $g(T) = 0.1 \dots 0.3$ W/Km (149) and specific heat conductance $c_{CNT}(T) = 2500 \dots 3900$ W s/kg K (70). Therefore, the upper limit of operation frequency for incandescent CNTs, $\frac{1}{\tau_{therm}}$ is in the range of 100 GHz. The expected operation limit for electroluminescent SWCNTs with exciton lifetimes $\tau_{lum} \approx 10\,ps$ (150–152) should be in a similar range.

Although both EL as well as incandescence enable operating of CNT emitters in high frequency mode, only two experimental works were published recently in this field. The gate-controlled generation of luminescent pulses in the µs range was demonstrated for individual suspended SCCNTs (153). For the case of MeCNT films, the incandescent high-frequency free-space emission was reported (66).

In this section the usage of CNTs as waveguide-integrated electrically driven pulsed light sources is demonstrated. The emitting properties of CNTs in the broad frequency range of up to GHz were investigated (13). The presented results emerge potential application of CNTs as fast nanoscale light source for the on-chip signal generation.

The pulsed measurements were performed preferentially with MeCNTs (suspension S3)

on standard waveguided devices and PCNBC-structures (Section 3.6), SCCNT-based devices (suspension S2) were also characterized. The SEM-images of the typical samples with deposition densities ranging from $1\,\mu m^{-1}$ to $100\,\mu m^{-1}$ are shown in Figures 3.28a-c.

The samples were placed in the free-space setup and electrically driven by means of a pulse generator. Similar to the experiments under continuous electrical excitation, discussed in the previous subsections, ac biasing of MeCNTs above a threshold voltage V_{th} induced long-time stable emission. Figure 3.29a demonstrates a series of emission spots measured between the electrical contacts at different biasing conditions, illustrating the rapid increase of emission intensity with pulse magnitude. For quantitative characterization of radiating properties ac-driven MeCNTs, the integral intensities of light spots I were measured at variable voltage magnitude V_{pulse}, pulse width w and duty cycle $D = \frac{w}{Pulse\ periode}$ of electrical signal. As shown in Figure 3.29b, the normalized emission intensity $I_{norm} = {}^{I}/_{D}$ raised by four orders of magnitude with increasing V_{pulse}, unaffected by pulse width in the broad frequency range (black and pink symbols). As for some samples threshold voltage V_{th} can extend the maximal pulse voltage that can be applied using pulse generator, an additional offset bias V_{dc} has to be used (Figure 3.29b, inset). For $V_{dc} < V_{th}$ the biased MeCNTs under $V = V_{dc} + V_{pulse}$ show a similar trend as devices without an offset bias (Figure 3.29b, blue and green symbols).

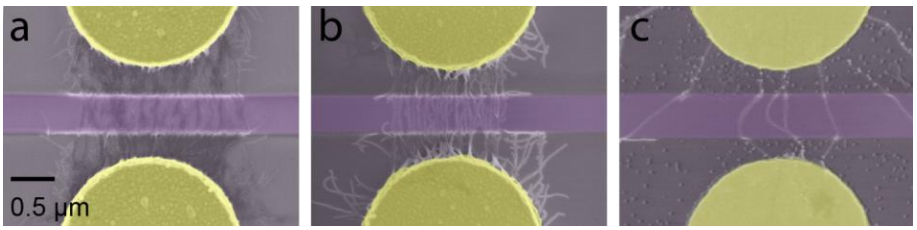

Figure 3.28 | WINS-devices used for pulsed measurements.

False-colored SEM images of waveguides (purple), horizontally aligned between metallic contacts (yellow). The CNTs can be seen as thin vertical lines between the electrodes crossing the waveguides. The density of MeCNTs per waveguide length ranges from films with ~ $100\,\mu m^{-1}$ (a) to multi-tube devices (~ $10\,\mu m^{-1}$, b) and to single-tube devices (c).
Adapted with permission from (13).

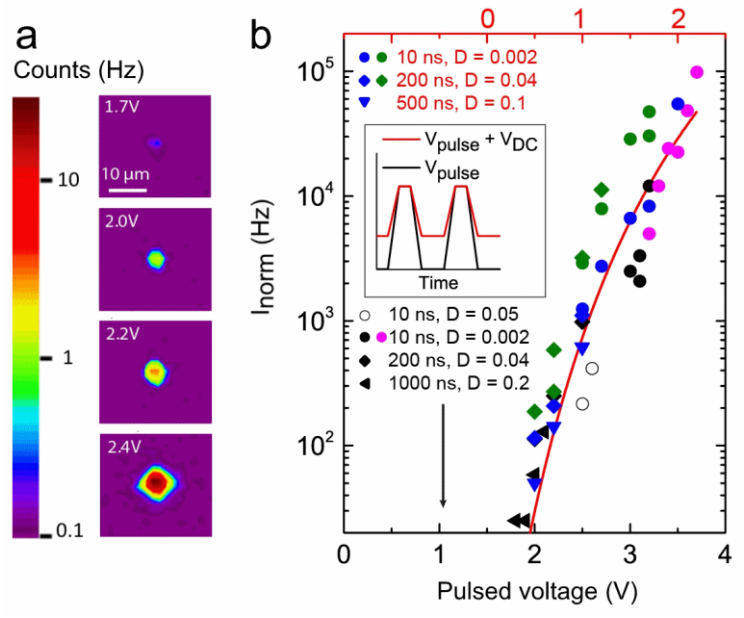

Figure 3.29 | Intensity of pulsed emission in free-space setup.

(a) Spatially resolved light emission from a CNT emitter driven with 100 ns electrical pulses at 200 kHz rate for different V_{pulse} .
(b) Normalized total intensity I_{norm} versus V_{pulse} under variation of electrical pulse width *w* and duty cycle *D*. The full line is a fit to the data. I_{norm} increases rapidly with V_{pulse} independent on *w* and *D*. The inset schematically illustrates two biasing schemes.
Adapted with permission from (13).

In order to understand the voltage-dependence of I_{norm} the spectral characteristics of pulsed CNT emitters were measured. The emission spectra of ac-biased MeCNTs demonstrated the typical incandescent profile with continuous increase of intensity at longer wavelengths along with interference modulation (Figure 3.30a, similar to Figure 3.8b). The extracted electron temperature varies in the common range of 1000 K and 1500 K depending on the type and density of MeCNTs, as well as on the operation parameters such as voltage and pulse width. The average MeCNT temperature in pulsed regime was not significantly different from the temperature of dc-biased MeCNTs (10,63,64).

Therefore, ac-driven MeCNTs act as regular thermal emitter and the detected temperature-dependent emission spectra $I_{m,fs}(\lambda,T) \sim S_{fs}(\lambda)I(\lambda,T)$ can be easily simulated, as shown in the inset of Figure 3.30b considering black body emission profile $I(\lambda,T)$ and Gaussian-shaped spectral sensitivity of the Si detector $S_{fs}(\lambda)$. The integrated temperature-dependent intensity of detected light along with two functions

used for fitting of incandescent CNT emission are demonstrated in Figure 3.30b. Power law fit $I \sim (T - T_0)^4$ (154) with a temperature offset T_0 as a fit parameter does not match the data well, especially at lower temperatures. In contrast, the data fit well to the function $I \sim e^{-E/kT}$ (63) with the energy $E = 1.5\,eV$ (830 nm) corresponding to the maximum spectral sensitivity of the Si detector.

MeCNT emitters were driven at relatively high bias regime where current through the CNT increases sublinearly with the voltage or even saturates due to the electron scattering on optical phonons (71,149,155). Consequently, the dissipated power and temperature raised nearly proportionally to the voltage, $V \sim P_{el} \sim T$ and $I \sim e^{-E/kT} \sim e^{const\,/V}$ can be used for fitting of experimental results previously shown in Figure 3.29b (red line). The emission intensities measured at different ac-conditions over several orders of magnitude demonstrated an excellent agreement with the fit function.

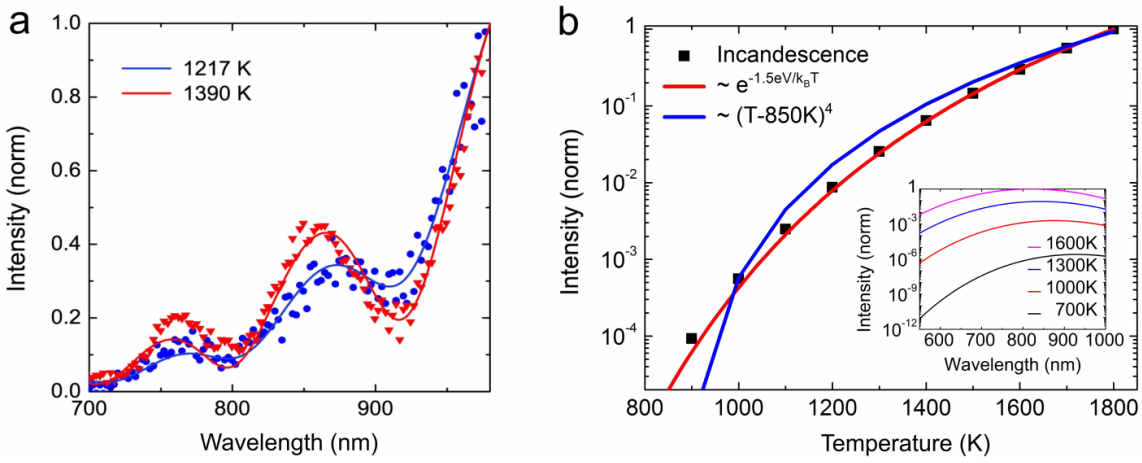

Figure 3.30 | Pulsed black body emission and temperature.

(a) Spectrally resolved light emission from a waveguide integrated CNT transducer, driven with 200 ns electrical pulses at 200 kHz repetition rate for $2V_{pulse}$ (blue circles) and $3V_{pulse}$ (red triangles). The full lines are fits to a black-body radiation curve modulated by substrate induced interference. The thermal emitter temperature from the fit is 1217 K (1390 K).
(b) Simulation of the temperature-dependent total intensity of the collected light (black symbols), compared with Arrhenius-type (red line) and power law (blue line) fits. Inset: Simulated spectra of a thermal emitter measured by the free-space setup in this work. The emitter temperatures are indicated. The shape of the spectra deviates from the Planck curve due to the spectral sensitivity of the detector.
Adapted with permission from (13).

3.7.2 Pulsed Measurements in Fiber-Coupled Setup

In the previous sections the emitting properties of CNTs were studied in the free-space setup allowing for the spatially resolved imaging, broad spectral characterization and detection of both directly emitted and waveguided light. Nevertheless, all the investigated devices presented in the Sections 3.4-3.7 provide grating couplers, so that the characterization of the CNT-emitted light is also possible with an external fiber-coupled detector in transmission setup described in Subsection 3.3.1. Coupler grating enables additionally wavelength-specific filtering of the light signal which has its positive and negative aspects in comparison to the free-space measurements. In fact, the efficiency of free-space detection $\eta_{fsd} \approx 0.01$ (119) is relatively low in comparison to the efficiency of external fiber-coupled detector $\eta_{fcd} \approx 0.5$, even taking into account the out-coupling loss $\eta_{oc} \approx 0.2$. However, due to the narrow transmission bandwidth of the grating coupler, the integral detection efficiency of broadband thermal emission $I(\lambda, T)$ using fiber-coupler setup is inferior to the free-space setup by factor of 0.2 (1000 K) to 0.5 (1500 K):

$$\frac{I_{fiber\ -coupled}}{I_{free\ -space}} \approx \frac{\eta_{fcd}\ \eta_{oc} \int_{730\ nm}^{770\ nm} I(\lambda,T)d\lambda}{\eta_{fsd} \int_{500\ nm}^{1030\ nm} I(\lambda,T)d\lambda} = 0.2\ (1000\,K) - 0.5\ (1500\,K) \qquad (3.13)$$

This order-of-magnitude estimation was performed for the typical grating coupler with the central wavelength of 750 nm.

On the other hand, the fiber-coupled setup has some advantages, namely it is more flexible with respect to sample environment options and detection techniques. It became crucial for pulsed emission experiments, because the Si detector used in the free-space setup was not suitable for time-dependent measurements with the required picoseconds resolution. Therefore, for the measurements with a high time resolution an external fast detector was employed and the measurements were performed in the fiber-coupled setup at vacuum conditions. This was an additional benefit, as CNTs under the exclusion of oxygen were protected against burning and could be driven at higher electrical powers yielding significantly stronger emission intensity.

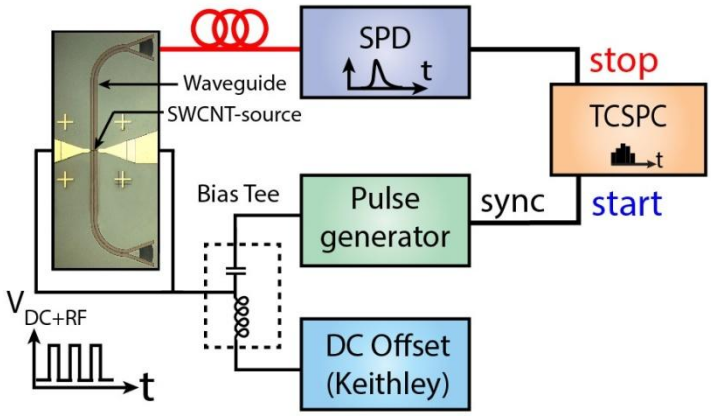

Figure 3.31 | Fiber-coupled setup for TCSPC measurements.

Adapted with permission from (13).

At first, at 10^{-7} mbar a tested device was electrically connected to the pulse generator via RF probes (Cascade Microtech) and optically connected to an external light source and detector via fiber-optics. The optimal position of the waveguide device with respect to the fibers was found in order to achieve the highest out-coupling efficiency (Subsection 3.3.1). Then the external light source was switched off and time-resolved emission experiments on ac-driven waveguide-coupled CNTs were performed. The measurement configuration is schematically shown in Figure 3.31. The time-correlated single-photon counting (TCSPC) technique used for the characterization of CNT emitters is optimal for the study of weak light sources and ultrafast processes (156). Start-Stop method was used to accommodate the photon arrival times in a histogram with 4 ps resolution using Picoharp 300 and a second time-synchronized output of a pulse generator as a trigger for time counting.

As already shown in the free-space measurements, a pulsed electrical signal which was applied to CNT transducers induced light emission. TCSPC-histograms provided a comparison between electrical excitation and optical response signal in the time domain. The guided optical pulses measured at the grating coupler followed the form of an electrical signal (Figure 3.32a) in the broad pulse width range between 5 ns and 200 ns without any significant broadening or delay in consistent with the results reported for free-space emitting CNT films (66). Some intensity modulations of the optical signal (Figure 3.32a, 20 ns and 70 ns) are attributed to signal reflections in the connection

cables and an impedance mismatch between components in the RF system. Upon switching on the electrical signal a fast initial response on a sub-nanosecond timescale corresponding to CNT heating is observed. On a longer nanosecond scale (30 ns to 50 ns) an additional response contributed to the relative increase of emission, which is related to the temperature increase of substrate beneath the CNT (66).

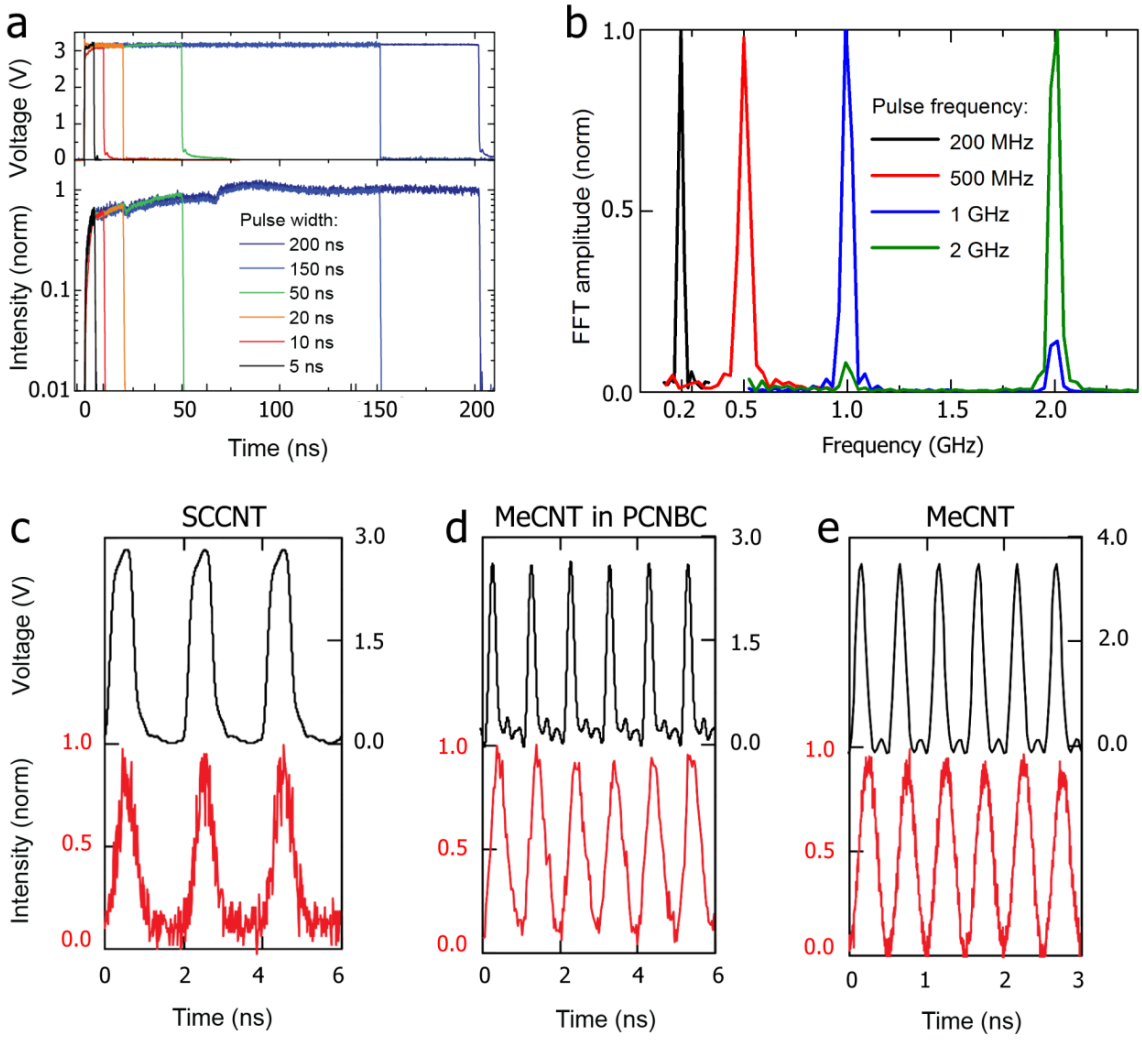

Figure 3.32 | Electrical pulses along with response emission.

(a) Comparison of electrical pulses with TCSPC-histograms of optical pulses, measured at a grating coupler.
(b) Normalized Fast Fourier Transform (FFT) spectra of modulated CNTs, emitting at frequencies of 0.2 GHz, 0.5 GHz, 1 GHz and 2 GHz.
(c-e) Sequence of electrical pulses (black curves) as well as emission pulses (red curves) measured with SCCNTs (0.5 GHz, c) and MeCNTs (2 GHz, e) in standard waveguide structures, as well as with MeCNTs in a PCNBC-device (1 GHz, d).
Adapted with permission from (12,13).

Therefore, for shorter pulses the response of CNT transducers is decoupled from the substrate heating and depends primarily on the intrinsic properties of CNT. In the following, CNT emitters were excited with a series of electrical pulses. The regular modulation of photon emission measured at different devices at 200 MHz to 2 GHz is demonstrated in Figure 3.32b using Fourier-transformations of TSCPC-histograms. No significant differences between individual CNTs and films, MeCNTs and SCCNTs were observed. Both SCCNTs in standard waveguide structures (Figure 3.32c) and MeCNTs placed in a PCNBC-cavity (Figure 3.32d) emitted pulsed light in accord with the applied electrical signal. In the last case, the CNT emerged as a nanoscale ultra-fast light source with exceptionally narrow emission profile. Theoretically, the optical pulse could be delayed and broadened by passing the PCNBC (157,158). However, according to Equation 2.4, this influence is negligible for devices with Q factors below 10^4, since the photon lifetime of the nanocavity τ_{cavity} (fs) $\approx Q/2$ at $\lambda \approx 1000\ nm$.

CNTs are very fast emitters, and this caused problems by their characterization because of technical limitations of experimental setup. Running the CNT emitter at the maximal settings of the pulse generator, the regular pulsed light emission at 2 GHz were observed (Figure 3.32e), even for the case of individual CNTs. This is also the fastest operation frequency of CNT emitter demonstrated so far.

The repetition rate of a light emitter is intrinsically limited by the decay time of emission τ. The observed τ_{therm} was strongly influenced by the total timing jitter of the measurement setup, determined primarily by the timing jitter of single-photon detector t, shown in inset of Figure 3.33 (red curve for SNSPD and blue curves for SPAD). The comparison between two detectors used for the characterization of the same CNT emitter is shown in Figure 3.33. The measurement performed with the slower single photon avalanche detector (τ-SPAD-100 with $t_{SPAD} \approx 350 ps$ in investigated wavelength range, blue symbols) demonstrated much longer decay time than it was observed using the faster superconducting nanowire single-photon detector (SNSPD with $t_{SNSPD} \approx 40 ps$, red symbols). Even for the second case the measured $\tau_{therm} = 79\,\mathrm{p}s$ is perhaps significantly enlarged in comparison to the intrinsic decay of the CNT emitter due to the total timing jitter and the decay time of the electrical pulse (Figure 3.33, black line). No significant variation of the measured τ_{therm} was observed, independently from the measurement conditions, CNT type or CNT density.

Therefore, due to technical limitations such as the frequency of the pulse generator and the timing jitter of the measurement setup, the highest operation frequency of incandescent CNT emitter could not be experimentally identified. Nevertheless, in the given measurements even single-tube devices revealed as reproducible, stable light sources in the GHz-range. In the end, it has been demonstrated that the electrically driven incandescent CNTs can be used as high-frequency electrically triggered light emitters on chip.

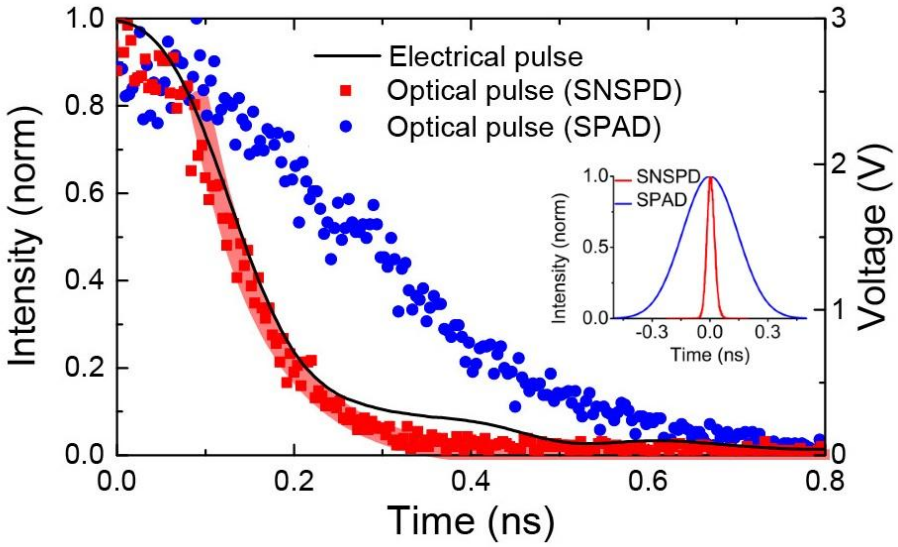

Figure 3.33 | Decay time of incandescent CNT emitters.

The decay of the CNT emission was measured with the slow SPAD (blue symbols) and fast SNSPD (red symbols along with fitted exponential decay time $\tau_{therm} = 79\,\mathrm{ps}$) after the end of an electrical pulse (black line) (13). Inset: Timing jitter measured for SNSPD (red line) and stated by producers of SPAD (blue line).
Adapted with permission from (13).

4. Further Research and Conclusion

4.1 Electroluminescence in Telecommunication Wavelength

This thesis project proceeds in several research areas. Recently a significant progress in EL measurements, especially in experiments with WINSes acting as non-classical emitters, was achieved. These findings clearly demonstrate the high potential of the WINS-technology developed within the framework of the thesis. The detailed discussion of the current and partly preliminary results would go beyond the scope of this study, thus, only the most promising directions are mentioned here.

One of the aims of the current research is to enhance the qualities of waveguide-integrated CNT-based emitters as a technology for application-relevant on-chip light sources. The obvious improvement would be the development of devices operating in the telecommunication wavelength range of 1550 nm (C-band). This requires three steps, namely

1. Achievement of stable and reproducible light emission at the desired wavelength, either using intrinsic SCCNT properties (EL emission) or due to the tuning of photonic environment (PCNBC, Section 3.6).
2. Adjustment of the nanophotonic architecture to the NIR-conditions.
3. Integration of CNTs into the modified structures, requiring an optimization of DEP-parameters due to the changed device geometry.

The first, most critical milestone has been already achieved, since the EL of individual SCCNTs in the NIR on the test short-channel devices without waveguides was recently demonstrated (14). These structures with Pd-electrodes on top of Si/SiO_2 (0.8 µm) substrate were fabricated and characterized by I. M. Alamgir and S. Dehm. With the installation of the InGaAs detector, sensitive in the wavelength range between 900 nm and 1600 nm, a detailed investigation of electroluminescent CNT with diverse chiralities became feasible. As shown in Figure 4.1, the emission spectra measured on the test devices in the free-space setup reveal several pronounced maxima, which refers to the radiative E_{11} -transitions of corresponding SCCNTs deposited from the few-chirality suspension S2. Especially (10,8)-SCCNTs with E_{11}-maximum at around 1550 nm (red symbols) could be of interest as application-relevant light sources. To the

extent of our knowledge, it is the first demonstration of CNT emission in the telecommunication wavelength range. The EL maxima are systematically red-shifted with respect to the corresponding peaks in the absorption spectrum of the tested CNT suspension (gray line) due to the change in the dielectric SCCNT environment(117). The electroluminescent maxima, corresponding to (6,5)-, (7,5)-, (7,6)- and (8,6)-SCCNTs with smaller diameter also present in the suspension, were almost never observed probably due to the dominance of the thermal emission at the shorter wavelengths. In general, electroluminescent SCCNTs reveal as long-time stable, reproducible and reversible light-sources.

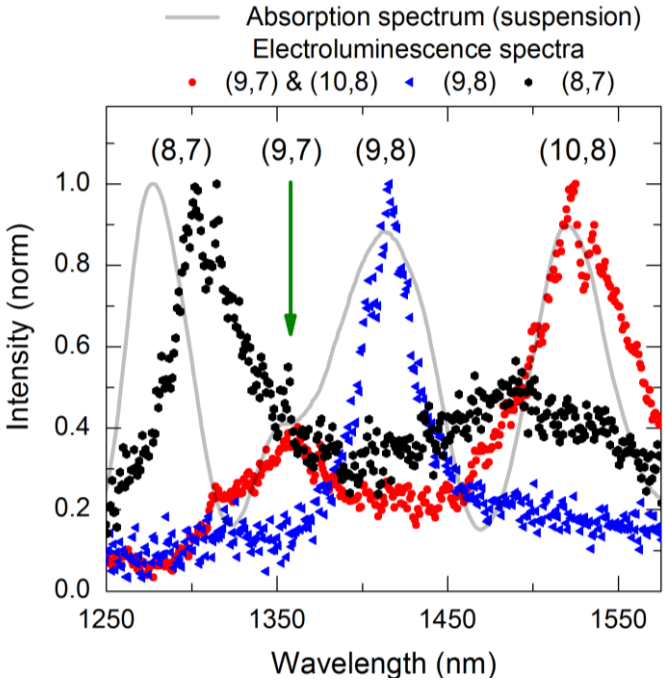

Figure 4.1 | Comparison of absorption spectrum with EL emission in NIR.

Absorption spectrum of SCCNT suspension (gray curve) along with EL spectra of three SCCNT-based devices (black, blue and red symbols). (n,m)-assignment was performed based on Kataura plot (40). Adapted with permission from (14).

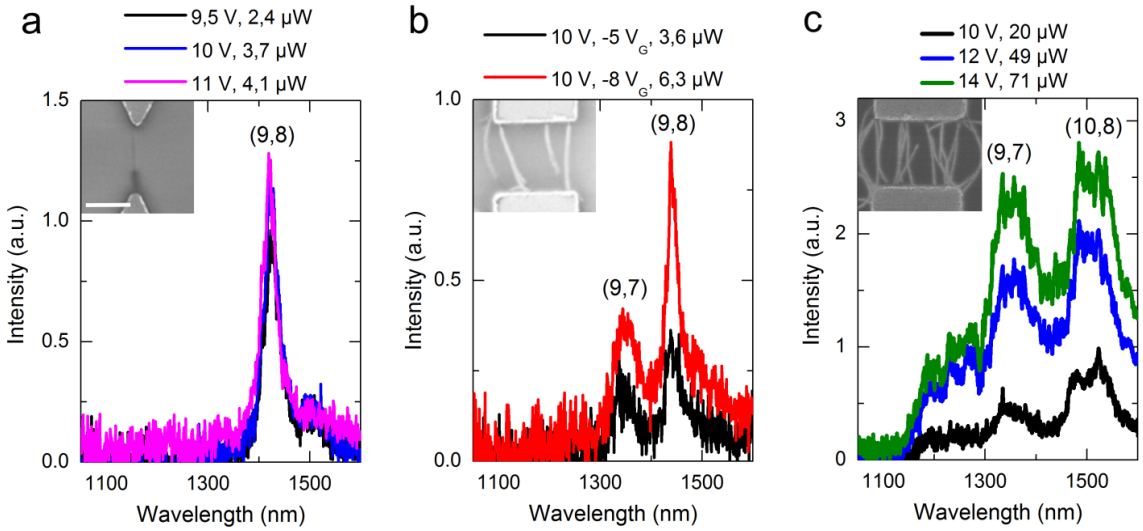

Figure 4.2 | EL spectra of devices with different SCCNT densities.

(a) Single-tube device (inset, scale bar 0.5 µm) measured at variable dc-bias revealed one emission maximum, corresponding to (9,8)-SCCNT. The peak position and the linewidth is independent on the biasing conditions.
(b) Device with two SCCNTs bridging metal electrodes (inset) demonstrated two emission maxima characteristic for (9,7) and (9,8) SCCNTs. The emission intensity was triggered by variation of V_G. (9,8)-peak with FWHM = 23 nm (14 meV) is the narrowest reported EL maxima.
(c) Emission spectra of multi-tube device (inset) measured at different voltages exhibited several broad EL maxima. Emission intensity increased at longer wavelength, as is typical for thermal emitter.
Adapted with permission from (14).

In general, individual SCCNTs (Figures 4.2a,b) with narrow-line emission profile turned out to be more efficient and better controllable light sources in comparison to SCCNT films (Figure 4.2c). The emission spectra of multi-tube devices typically showed several broad maxima with significant thermal contribution, while single-tube devices demonstrated single narrow-line peaks at lower electrical power. Additionally to the tuning of the emission intensity by variation of V_{sd} (Figure 4.2a), SCCNT-based devices can be triggered adjusting V_G (Figure 4.2b).

Therefore, for the first time electrically driven CNT emission in the telecommunication wavelength range was demonstrated. Moreover, the observed emission linewidth of 23 nm (Figure 4.2b) is 2 to 8 narrower than the previously reported EL results (50,62). As the next step, the integration of electroluminescent SCCNTs in the appropriate nanophotonic environment for on-chip emission measurements in the range of 1550 nm is planned.

4.2 SCCNT as Waveguide-Integrated Single Photon Emitter

We continue the development of advanced devices with CNTs as active optoelectronic element. As described in Subsection 2.3.3, SCCNTs emerge as single photon sources in PL experiments (77–79). This is an application-near research area due to cryptography needs (72–74), and an advancement would be the demonstration of antibunching photon for electrically driven on-chip integrated SCCNTs. Here preliminary results in this field, achieved in cooperation with the research group of Prof. W. H. P. Pernice and S. Khasminskaya, are presented (15).

Our goal was the scalable realization of a quantum photonic circuit with single photon detectors (D) and SCCNT as single photon emitter (E), schematically shown in Figure 4.3a. A series of devices depicted in the SEM image in Figure 4.3b was fabricated. SCCNTs from the suspension S2 were deposited between the metal contacts on the waveguided structures with integrated superconducting nanowire single photon detectors (SNSPDs (159–161)) at the ends. Therefore, instead of the grating couplers for external detection of CNT-emitted light, the presented devices possesses integrated electrically driven broadband detectors. The sample geometry, consisting of a central light source between two equally spaced SNSPDs, allows for antibunching measurements in Hanbury-Brown and Twiss setup.

At cryogenic conditions required by SNSPDs, electrically driven SCCNT emitted light is partially coupled into the waveguide and propagated towards the photon-counting detectors. As shown in Figure 4.3c, the count rate N' measured at every SNSPD is raising with the electrical current I and the electrical power over five orders of magnitude, demonstrating essential similarity with power-dependent PL measurements in continuous-wave mode (162). Therefore, we believe that in the performed experiment the light emission was dominated by luminescence and the kink at around 10 nA is attributed to exciton-exciton annihilation (EEA) with corresponding relative decrease in SCCNT emissivity (162). Another explanation for the kink would be the increased energy of excitons in favor of nonradiative decays, similar to the observations in PL experiments with increasing temperature (79,152,163). At higher currents beyond 50 nA (second kink) the contribution of thermal emission to the entire photon flux becomes crucial and the emission rate increases again.

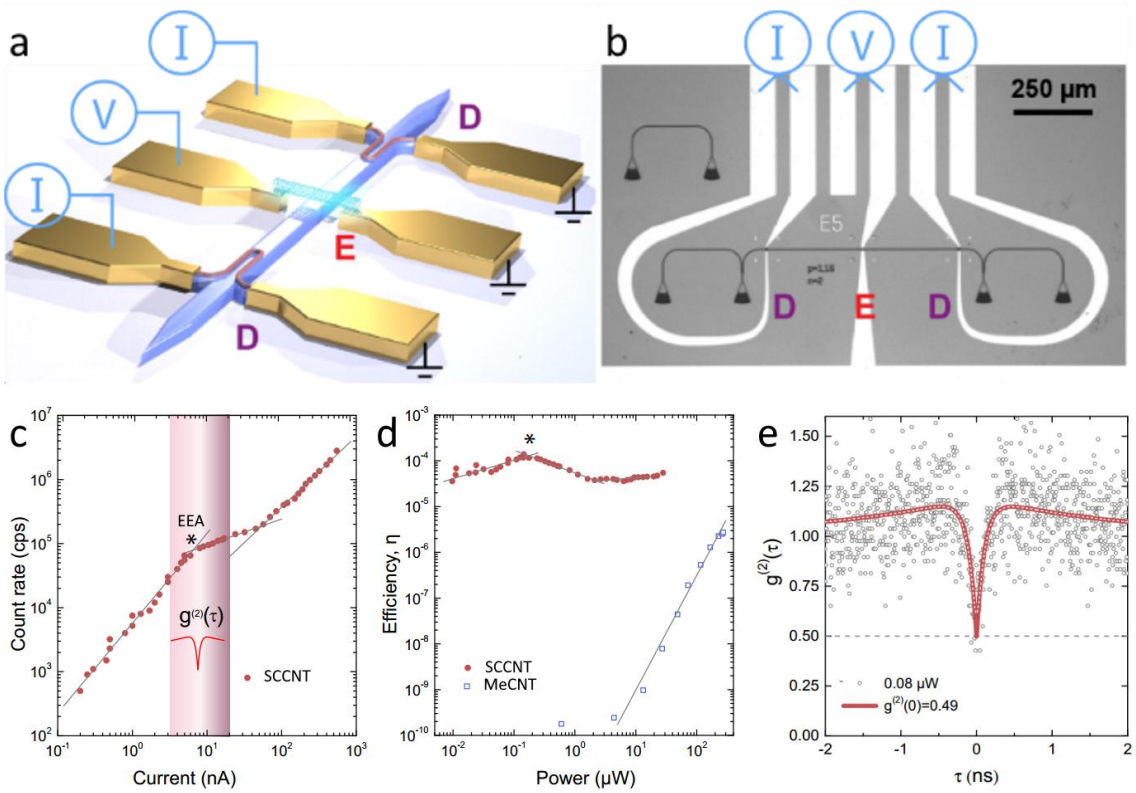

Figure 4.3 | Antibunching measurements in quantum photonic circuit.

(a) Schematic view of a waveguide with integrated SNSPDs (D) and SCCNT (E), both biased electrically.
(b) SEM picture of the metal contacts and the waveguide. The positions of the detectors and emitter are denoted with D and E.
(c) Count rate N' of a SCCNT emitter measured as a function of current. Two kinks in the emission curve are clearly visible. Linear fits reveal slopes of 1.4, 0.4 and 1.1 from left to right. The colored area represents the current range with the best observed antibunching.
(d) Quantum efficiencies η of SCCNT (red) and MeCNT (blue, suspension S3) depend on the electrical power. Luminescent light of SCCNT demonstrates much higher efficiency in comparison to incandescence of MeCNT in the presented power range.
(e) Second order correlation function $g_2(\tau)$ measured at SCCNT emitter from (c). Normalized coincidence histogram of non-classical light emission along with the fit (red line).
Adapted with permission from (15).

The quantum yield of CNT $\eta_{CNT} \geq \frac{4e^{-}N'}{I\,\eta_{SNSPD}\;\eta_{coupling}}$ was calculated taking into account the coupling efficiency of the emitted light into waveguide $\eta_{coupling}$ (≤0.6, Subsection 3.4.3) and SNSPD-efficiency η_{SNSPD} (≤0.15 for the wavelengths below 1600 nm). In Figure 4.3d the comparison between yields of MeCNT and SCCNT emitters as a function of power is shown. The electrically driven SCCNT emitter demonstrated with $2*10^{-4}$ a high quantum yield, orders of magnitude above incandescence. Measurements performed on other SCCNTs reveal η_{CNT} of up to 10^{-3} that is the highest efficiency reported for EL-SCCNTs so far (50,54). The observed

fundamental discrepancies in emitting properties of SCCNT and MeCNT point out the different dominant emission mechanism, electroluminescence and incandescence, respectively. Thanks to both relatively high detection efficiency and protective measurements conditions, it was possible to perform characterization of CNT emitters in a wider power range as in the previous experiments.

According to PL measurements (77,78), at the low temperatures excitons in SCCNTs can be localized at zero-dimensional defects, so that SCCNT can serve as a single photon emitter. At $N' > 10^4$ the number of photons is high enough for the calculation of coincidence histograms from time-dependent measurements at both SNSPDs. Histograms recorded at lower electrical currents (colored area in Figure 4.3c, corresponding to the efficiency maximum in Figure 4.3d) reveal pronounced photon antibunching, as exemplarily shown in Figure 4.3e. The central deep with $g_2(0) = 0.49 \pm 0.07$ is the figure of merit for antibunching that unambiguously characterizes electrically driven SCCNT as a non-classical light source. In comparison to the previously reported antibunching observed in PL experiments (77,79), the electroluminescent SCCNT emitter presented in this work demonstrated significantly higher count rate. At higher electrical energy the antibunching was diminished probably due to the weaker localization of excitons (79) and completely disappears beyond 20 nA. In contrast, for MeCNTs no antibunching was observed for any current levels.

With these results a single-photon emission from electrically driven SCCNTs was demonstrated for the first time. In the following a study of non-classical properties of SCCNT in more detail is planned, in order to understand the influence of the gating voltage, SCCNT type and measurement conditions on the device performance as well as to improve its performance in terms of $g_2(0)$ and η_{CNT}.

4.3 Outlook

There are several important improvements that would make WINS-technology more attractive for potential applications. Preparation of CNT suspension, CNT deposition process, nanophotonic architecture and measurement technique can be significantly optimized with the expected strongly increase of efficiency and performance of WINS-devices.

For the scalable fabrication of WINSes with determined electrical and optical properties a structurally pure CNT material is required. Especially suspensions with high percentage of (10,8)- and (10,9)-SCCNTs emitting around 1550 nm are sought for preparation of WINS-devices operating in the telecommunication wavelength range. Optimization of CNT sorting techniques using solution-based separation methods are the main research themes of Dr. B. S. Flavel (30) and Dr. F. Hennrich (31), who prepared the suspensions for the fabrication of WINSes. Alternatively, recent efforts in the chirality-specific growth of CNTs (24,164) gave rise for hope for a controllable synthesis of CNTs with the desired parameters. In both cases, the ultimate goal would be the production of pure monochiral SCCNT suspensions with narrow length distribution.

In fact, CNT length is another structural parameter that determines performance of WINSes. Most of the devices used in this study had an electrode distance of 1 µm as the available CNTs were not long enough to bridge a significantly broader gap. Although the demonstrated devices revealed a satisfactory performance, it would be of advantage to access CNTs with lengths of 1.5 µm to 2 µm. Longer CNTs allow for fabrication of devices with the bigger separation between electrodes and waveguide that lowers the radiation damping. This is especially important for CNTs integrated into PCNBCs (Figure 3.26). Moreover, it should be also ensured that the ends of CNTs overlap both metal electrodes by at least 100 nm to minimize contact resistance (165). The quality of electrical contacts is critical for reproducible fabrication of efficient WINS-devices. High contact resistance leads to the decrease of electrical power dissipated through the CNT, contact heating and unstable transfer characteristics of WINS-devices. Moreover, the CNT adhesion and contact quality can be improved by optimization of sample annealing after DEP or with subsequently metallization of CNT-metal contacts from the

top (166). It is important to mention that SCCNTs with a smaller bandgap and larger diameter have significantly lower contact resistance due to the larger contact area and smaller Schottky-barrier. Thus, WINS-devices operating in the NIR would have lower contact resistance.

In ambient conditions, WINS-devices cannot be driven at higher electrical powers since self-heating induces oxidation of nanotubes and metal contacts. In order to preserve CNTs, the measurements can be performed in vacuum. This significantly increases the operating range of WINS-devices as it was demonstrated in Sections 3.7 and 4.2. Alternatively, CNT can also be protected by covering with a thin transparent layer of polymer or oxide. As an additional advantage, in this way the creation of solitary oxygen dopand states can be induced (79). Deep trap states for exciton localization at the desired areas of CNTs (e.g. in the middle, on top of waveguide) could also be realized by means of e-beam lithography. In the both cases, doping allows for controllable tuning of SCCNT emission wavelength (167) and offers promising prospects for room-temperature single-photon electroluminescence

Fabrication of WINSes emitting in the telecommunication wavelength range opens exciting opportunities for application-relevant research. Both incandescent and electroluminescent emission processes are much more efficient at longer wavelengths. Thus, a significant enhancement of the WINS-performance from visible to NIR is expected. Moreover, the replacement of Si_3N_4 with NIR-transparent silicon waveguides would offer more freedom for design, operating and application of WINS-devices. Silicon photonics can also be implemented on the same substrate with the directly compatible microelectronics.

The determination of Q factor for PCNBC-emitters, maximal modulation frequency and intrinsic decay time for ac-driven CNTs were limited by the resolution of the free-space setup, the operating range of the pulse generator and the timing jitter of the detector, respectively (Subsections 3.6.4 and 3.7.2). For further progress in these areas, an improvement of the measurement setup or cooperation with other research groups is essential.

As shown in Section 4.1, SCCNTs appear as relatively narrow-line EL emitters in the NIR. Electroluminescent processes in short-channel CNT-based devices are not fully

understood till now and further measurements are required, especially to clarify time-dependent emitting behavior of SCCNTs in the sub-nanosecond range. The most important questions for electroluminescent SCCNT are: What is its highest possible operating speed? and What are the conditions, requirements and limitations of single-photon emission? In any case electroluminescent SCCNTs are preferred over incandescent CNTs in the NIR and hence the next generation of WINS-devices will be driven by EL emitters. Using chirality-sorted SCCNT suspensions, WINSes with the tailor-made wavelength-selective nanophotonic structures such as PCNBCs, interferometers or ring resonators can be fabricated. The devices fabricated in this way should demonstrate high-speed and intrinsically narrow-line electroluminescent pulsed emission in the telecommunication wavelength range and, potentially, also in the single-photon regime.

Lastly, an important aspect that was not addressed in this study is the response of waveguide-integrated SCCNTs to light exposure. Photoluminescence and photocurrent measurements performed on WINS devices would not only provide complementary information regarding CNT properties in nanophotonic environment, but could also be useful for development of novel applications such as waveguide-integrated SCCNT-based photodetectors.

4.4 Conclusion

The presented work is a proof-of-concept study for scalable realization of waveguide-integrated electrically driven CNT emitters. MeCNTs and SCCNTs were dielectrophoretically deposited from suspensions onto nanophotonic devices, fabricated using e-beam lithography. The electrically excited CNTs acted as nanoscale sources of thermal and electroluminescent light that coupled into underlying waveguide with high efficiency of up to 60%, propagated inside nearly lossless and coupled out at coupler gratings. Spectral and dynamical properties of WINSes were studied in the free-space and fiber-optic setups.

About 10 types of WINS-devices were designed, fabricated and characterized. The determination of propagation loss by means of emission measurements with an integrated CNT emitter eliminated the need of an external light source and in- and out-coupling system for the waveguide characterization. The propagation of CNT-

emitted light in the extended waveguide structures over centimeter distances was demonstrated. On-chip devices like Mach-Zehnder interferometers and directional couplers were scalable implemented within the WINS-framework. Integration of CNTs into photonic crystal nanobeam cavity allowed for the spectral tuning of CNT-emitted light. The tailored mode frequency of such devices depends only on the cavity geometry and CNT position inside PCNBC, but not on the intrinsic CNT spectrum. Adjustable emission maxima feature linewidths of ≈ 1 nm limited by the spectral resolution of the measurement setup and at least an order of magnitude narrower than measured previously for electrically driven CNTs. This device concept allows the fabrication of WINSes emitting at telecommunication frequencies with Q factors beyond 10^5 and linewidths below 10^{-2} nm.

Exceptionally high thermal conductivity of CNTs was utilized for realization of ultra-fast light emitters. Different types of ac-driven WINSes operated in the broad MHz and GHz frequency range by the conversion of a modulated electrical signal into a pulsed incandescent light. The optical pulses were guided through the waveguides at frequencies of up to 2 GHz limited by the pulse generator. However, with the intrinsic response times of incandescent or electroluminescent CNT in the order of 10 ps modulation of optical signal at 10 to 100 Gbit/s can be realized. In combination with PCNBCs, WINSes appear as multifunctional on-chip light sources with both extremely high response speed and exceptionally narrow-line adjustable emission profile.

Moreover, the recent measurements in the telecommunication wavelength range demonstrate the potential of SCCNTs as electroluminescent non-classical light source. Full-integrated SCCNTs in quantum photonic circuit emitted antibunched photons with $g_2(0) \approx 0.5$ at 10^5 cps that is orders of magnitude higher than in comparable measurements with photoluminescent SCCNTs.

Thus, the presented concept of electrically driven WINS emerges as diversified experimental platform for both fundamental and application-oriented research on integrated CNT emitters.

Appendix

The following supplementary information includes the contributions of collaborators, corresponding to the preparation of the CNT suspensions, as well as to the fabrication and the simulations of WINS-devices. These results were reported in the publications (10–13) and are summarized here to ensure the completeness of the data presented in this work.

A: Calculation of Light Propagation in Waveguide[1]

Finite-Difference Time-Domain Calculation of the Electric-Field Intensity

In order to analyze the near-field coupling of the CNT emitter to the waveguide structures FDTD simulations were performed using the commercial software package OmniSim distributed by Photon Design. The simulations were carried out full-vectorial in three dimensions using high grid resolution to ensure convergence within a 5% error margin. The CNT emitter was modeled as an elongated dipole source with dimensions corresponding to the real nanotube emitters, placed in direct contact with the top surface of the waveguide. Simulations were carried out both for continuous-wave excitation to obtain travelling wave modal distributions as shown in Figure 3.1b, as well as with pulsed excitation to obtain the broadband response of the waveguide structure.

Calculation of Effective and Group Refractive Indices of Si_3N_4 Waveguides

The optical characteristics of waveguide are determined by the effective refractive index $n_{eff}(\lambda)$, calculated from refractive indices of waveguide core and surrounded media for the given waveguide geometry. For a 500 nm wide rib waveguide which is half etched into a thick Si_3N_4 layer on top of SiO_2/Si, $n_{eff}(\lambda)$ has been calculated using finite - element simulations (Comsol Multiphysics) (168). The wavelength-dependency of n_{eff} is demonstrated in Figure A.1a (blue markers).

[1] adapted from the Supplementary Information to (9), performed by Prof. W. H. P. Pernice and S. Khasminskaya.

The group refractive index $n_g(\lambda)$, defined as the ratio of the vacuum velocity of light to the group velocity in the medium, is used for calculation of time delays for ultra-short pulses or the free spectral range (FSR). For the rib waveguide $n_g(\lambda)$ has been calculated according to the following equation (Figure A.1a, red markers):

$$n_g(\lambda) = n_{eff}(\lambda) - \lambda \frac{dn_{eff}(\lambda)}{d\lambda} \qquad \text{(A. 1)}$$

The wavelength dependence of the chromatic dispersion in Si_3N_4 has been accounted for through a Sellmeier equation (169).

The distribution of electric field at for λ = 700 nm and λ = 900 nm is shown in Figure A.1b,c.

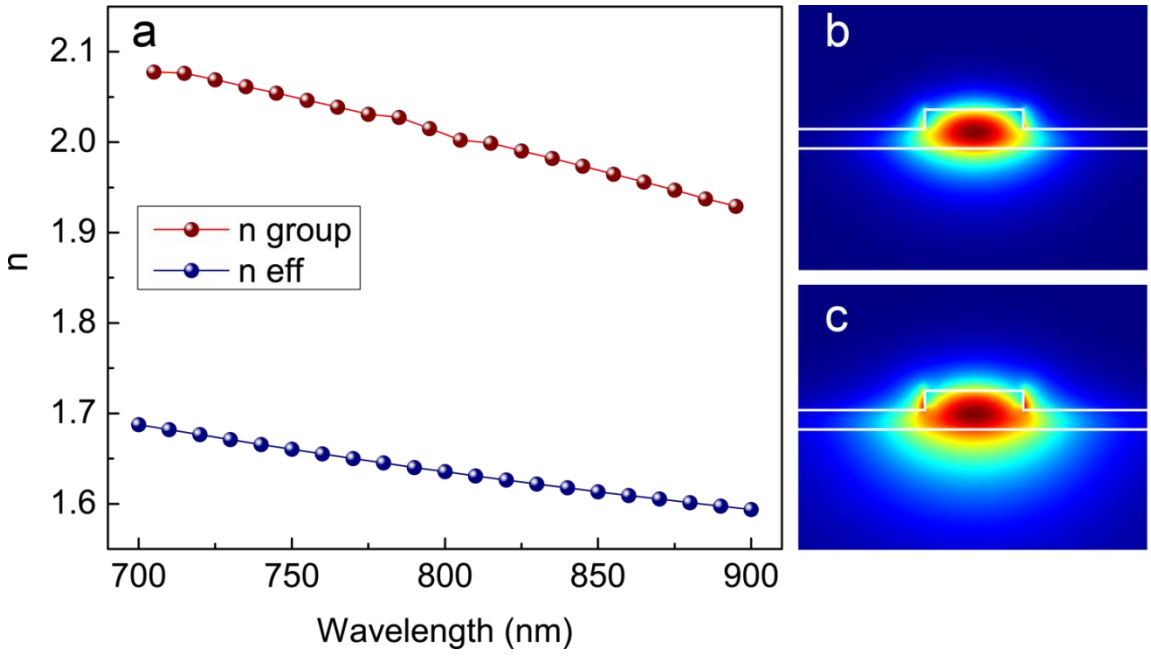

Figure A.1 | Refactive index and electric field distribution in waveguide.

(a) Numerical simulation of the effective refractive index $n_{eff}(\lambda)$ (blue markers) and group index $n_g(\lambda)$ (red markers) of the waveguide for Si/SiO_2 (2 µm)/Si_3N_4 (0.2 µm) substrate.
(b,c) Cross-sectional electric field intensity distribution $\vec{E}^2$ for λ = 700 nm (b) and λ = 900 nm (c), equivalent to the color overlay shown in the main text in Figure 3.1a for λ = 750 nm.

4.5 B: Device Fabrication and Materials

Lithography[2]

In the following the fabrication of the standard waveguided devices (Sections 3.4 and 3.5, by S. Khasminskaya (10) and R. Fechner (11)) as well as PCNBC-devices (Section 3.6, by V. Fütterling (12)) is described. The devices were prepared from doped Si-wafer with SiO_2 (2 µm) / Si_3N_4 (0.2 µm) top layers.

Rib waveguides were fabricated in close vicinity to electrical contacts using several steps of electron beam lithography with subsequent dry etching. The nanophotonic devices were prepared from high quality silicon carrier wafers, containing 200 nm of stoichiometric Si_3N_4 deposited by low pressure chemical vapor deposition (LPCVD) on top of 2000 nm buried SiO_2. Prior to lithography, all samples were cleaned via sonication in acetone for 10 min, rinsing in isopropanol followed by oxygen plasma etching (Diener Femto, 20 % power, 10 sccm, 0.4 mbar, 3 min) to remove organic residue. To drive off remaining water the samples were dried on a hot plate at 200 °C for 5 min. During the first lithography step the pattern for electrical contacts was written in 250 nm of PMMA on a Raith EBL system. After exposure the sample was developed in a solution of methylisobutylketon (MIBK): isopropanol (1:3). For manufacturing of metal contacts 50 nm gold was evaporated with a 5 nm adhesive layer of chromium and a 10 nm coating layer of chromium on top. The subsequent liftoff was performed by immersing the sample in acetone with subsequent weak sonication. In a second lithography step nanophotonic waveguides were defined in ZEON Chemicals ZEP 520A positive resist with alignment accuracy better than 20 nm. After developing for 50 s in Xylene, reactive ion etching (RIE) was used to transfer the pattern from resist into the Si_3N_4 on an Oxford 80 system. The etching recipe contained 50 sccm CHF_3 and 2 sccm O_2 at 175 W RF power and a base pressure of 55 mTorr. The sample was etched at a rate of 1.1 nm/s for several minutes in order to form ½ or ¾ etched Si_3N_4 waveguides. The optimal height of the waveguide allowing for the minimal propagation loss was determined in series of transmission tests.

[2] adapted from the Supplementary Information to (9) and (11), performed by S. Khasminskaya, R. Fechner and V. Fütterling.

The PCNBC structures were fabricated on a similar way (Figure 3.2). First, a 15 mm × 15 mm sample is spin-coated with PMMA 4% and alignment markers are exposed by a JEOL electron beam writer JBX-5500ZD at 50 keV. After development in 1:3 MIBK:IPA for 50 seconds, 5 nm of Chromium followed by 100 nm of Gold are evaporated onto the sample using a physical vapor deposition system. Subsequent lift-off is performed in a NEP (N-ethyl-2-pyrrolidone) bath using weak sonication. In the next step, the sample is coated with Zep520a photo resist. The PCNBC-devices are aligned to the local markers and exposed. After development in Xylene the waveguides and cut-outs for the electrodes are etched into the Si_3N_4 layer using an optimized RIE recipe described above, so that 150 nm from the initial 200 nm of Si_3N_4 were removed. In order to suspend the waveguide in a window around the cavity, a new layer of MicroChem PMMA resist is spin-coated on top of the remaining Zep520a resist, followed by the third e-beam lithography step. The windows are aligned to the existing structures on the sample and exposed. The PMMA is developed in 1:3 MIBK:IPA, removing the PMMA resist in the window area, but leaving the ZEP520a resist intact, which still covers the top of the waveguide and the electrode cut-outs. In the following RIE step, the remaining 50 nm of Si_3N_4 are removed inside the window area, while the waveguide inside the window is protected by the ZEP520a resist, and the outside waveguide is protected by the unexposed PMMA. After the RIE step, both the PMMA and the ZEP520a resists are removed in a NEP bath and subsequently in an Oxygen plasma cleaner. In the fourth step, the sample is spin-coated with PMMA 8% and the electrodes are exposed. After development in 1:3 MIBK:IPA for 3 minutes, followed by Oxygen plasma etching, 5 nm of Chromium and 165 nm of Gold are evaporated onto the sample, and the lift-off procedure is performed. The next step is the removal of the SiO_2 in the window area by isotropic wet etching procedure in 6% HF. The sample remains inside the HF bath for 15 minutes to clear the window below the waveguide to a depth of 1.5 μm.

Preparation of CNT Suspensions[3]

All the suspensions were prepared from HiPco raw material (Nanointegris) synthesized using catalytic chemical vapor deposition method.

The CNT suspension S1 was prepared by Dr. B. S. Flavel as described elsewhere (41). In brief 10 mg of raw SWCNTs was suspended in 15 mL of H_2O with 1 wt-% sodium dodecyl sulfate (SDS) using a tip sonicator (Bandelin, 200 W maximum power, 20 kHz, in pulsed mode with 100 ms pulses) applied for 2 h at ~20 % power. The resulting dispersion was then centrifuged at ~100,000 g for 1.5 h and carefully decanted from the pellet that was formed during centrifugation. The centrifuged CNT material was then used for gel filtration fractionation. Gel filtration was performed as described elsewhere (116) using a Sephacryl S-200 gel filtration medium (Amersham Biosciences) in a glass column of 20 cm length and 2 cm diameter with a final bed height of ~14 cm. After separation of the MeCNTs from the SCCNTs (stuck on the gel) the pH of the 1 wt-% SDS in H_2O eluent was changed from 4 to 1 upon addition of the appropriate concentration of HCl. The pH was reduced in 12 steps with the (8,7) material collected as an early fraction. The collected fraction was then dialyzed for 24 h to readjust the pH to 7 in 1 mL Float-A-Lyzer G2 dialysis devices by using 500 mL of a 1 wt-% sodium cholate solution in H_2O.

The suspension S2 with few-chirality SCCNTs was prepared by Dr. F. Hennrich as described previously (31,115). 100 mg of CNTs was dispersed for 2 h in 100 mL toluene with 100 mg of Poly(9,9-di-n-octylfluorenyl-2,7-diyl) (PFO, supplied by Sigma Aldrich), using a Bandelin-sonicator (200 W, 20 kHz) at 20% power. The resulting dispersion was then centrifuged at ~20,000 g for 2 h.

The suspensions of type S3 with MeCNTs were prepared by Dr. B. S. Flavel and Dr. F. Hennrich (116). 100 mg of CNT material was suspended in 100 ml H_2O with 2 wt% of SDS using the sonicator applied for 4 h at ~20% power, water cooled and centrifuged at 20,000 g over night. Gel filtration was performed using Sephacryl S-200 gel filtration medium. For the separation, 10 mL of CNT starting suspension was applied to the top of the column and a solution of 0.4 wt% SDS in H_2O as eluent was

[3] adapted from the Supplementary Information to (10) and (12), performed by Dr. F. Hennrich and Dr. B. S. Flavel.

pushed with the aid of an Agilent GPC system (30) through the column with a flow of ~ 1 mL/min.

The collected fractions of CNT suspensions demonstrated different length and chirality distribution (30,31,115). In most cases the first fractions of the suspensions were used as they contained the longest CNTs with the average length of 0.6 µm to 0.8 µm. In the Figure B.1 a typical AFM image of CNTs from suspension 2 along with the length statistics is shown.

The characteristics of CNT suspensions also slightly changed depending on the storage time so that preferentially fresh prepared suspensions were used.

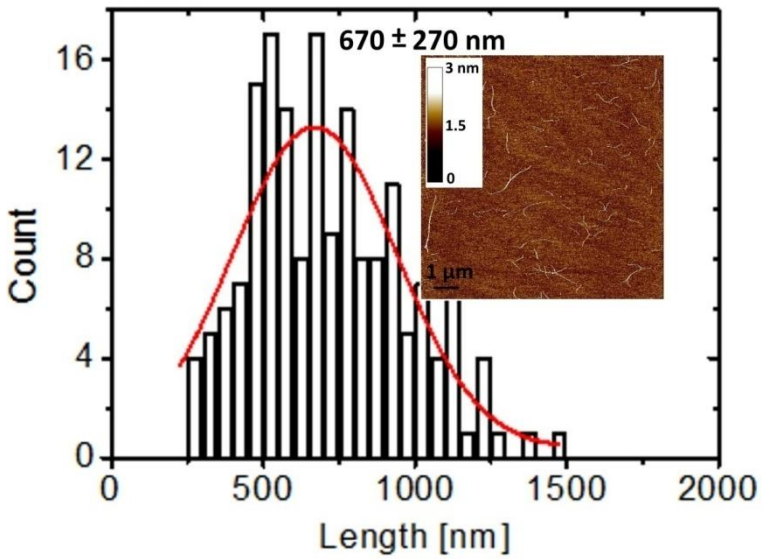

Figure B.1 | Length distribution of CNTs.

Length statistics extracted from AFM images (inset) of CNTs from suspension S2 (fraction 1).

C: Characterization of DCs Using Transmission Measurements[4]

In order to characterize the coupling behavior, DC-devices without CNTs were designed, as schematically shown in Figure C.1a. The characterization was performed with an external light laser source which was coupled into and out of a Mach-Zehnder-interferometer (MZI) by means of grating couplers (labeled *C1*, *C2*, *C3*). The MZI consisted of two waveguides split by a directional coupler (*DC1*) and then recombined (*DC2*).

Transmission measurements allow for an efficient determination of the optimal parameters of the DC with a 50/50 splitting ratio (170). The advantage of using a MZI is that it characterizes the coupler devices independent of any losses occurring at the grating coupler. In a MZI the original light beam is split at the *DC1* with a splitting ratio which depends on the wavelength. After a certain path difference both arms of the MZI approach each other at the *DC2*. Depending on the phase difference some wavelengths will interfere constructively while others will interfere destructively, an effect which leads to pronounced fringes in the spectrum as shown in Figure C.1b. The ratio between a maximum and its subsequent minimum is called the extinction ratio:

$$R_e = 10\ lg\left(\frac{P_{max}}{P_{min}}\right) \qquad \text{(C. 1)}$$

The higher R_e, the closer is the splitting ratio of the directional coupler to 0.5 for the specific wavelength range.

A series of MZI devices with fixed path length difference of 200 µm was realized. The interaction length L_i of both directional couplers in a device is varied around 23 µm and 5.5 µm. R_e was experimentally determined for various different L_i and wavelengths. For each device broadband light from a supercontinuum source was coupled into the device via grating port *C1*. The transmitted light at both ports *C2* and *C3* was recorded and analyzed with a spectrometer (Ando AQ-6315). Figures C.1c,d show the wavelength dependent R_e for devices fabricated with short and long L_i in the two directional coupler devices. The extinction ratio is color coded. Red implies the highest R_e approaching 17 dB. When the extinction ratio is high the intensity in both MZI arms

[4] adapted from (11), performed by R. Fechner.

is well balanced, indicating that the incoming power was evenly split. High reproducibility of results for devices with similar L_i was observed, attesting reliable fabrication. In agreement with the simulations L_i decreases at longer wavelengths (see Figures 3.17 and C.1c,d). In general, the highest R_e were achieved for devices with L_i being 1-3 µm shorter than it was simulated. The reason for this is the underestimation of L_i in the 2D simulation of the cross section of the directional coupler, because the coupling between both waveguides starts already while they are approaching each other.

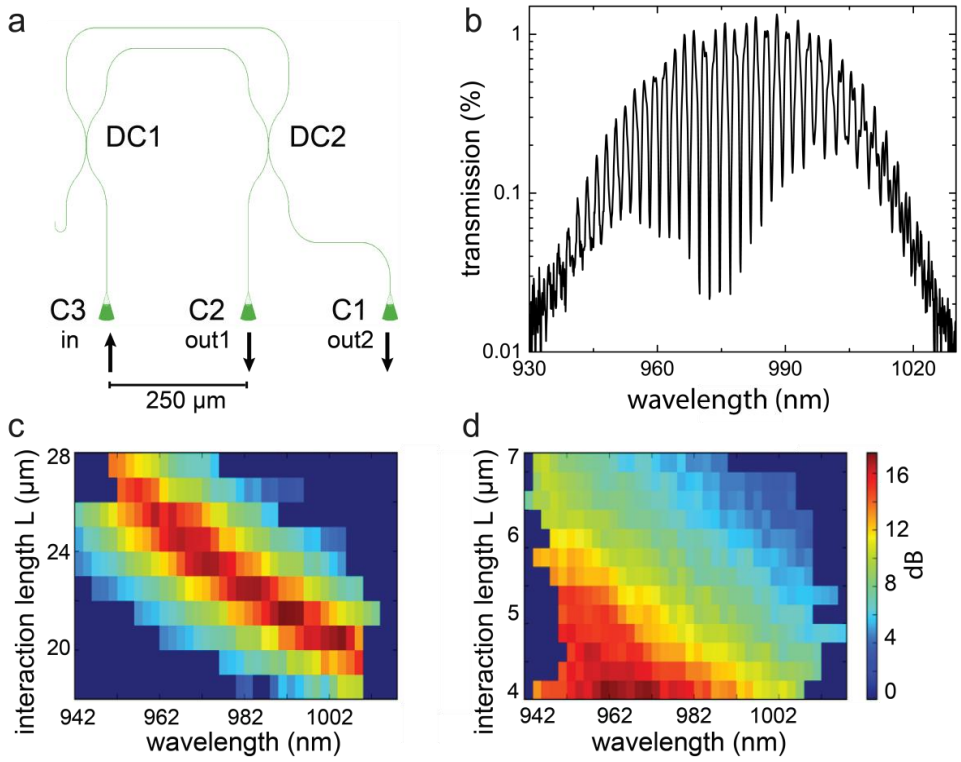

Figure C.1 | Characterization of directional couplers using transmission measurements.

(a) Schematic layout of a Mach-Zehnder-interferometer (MZI) device for determining the splitting ratio of the directional couplers (DCs). Two directional couplers *DC1* and *DC2* are used to realize the interferometer with a path length difference of $200\ \mu m$.
(b) Measured transmission spectrum of MZI device with two DCs with $L_i = 23\ \mu m$. The extinction ratio is the difference between the transmitted intensity maximum and the successive intensity minimum in dB.
(c,d) Color-coded measured extinction ratio R_e in dB vs wavelength and L_i. Shown are two measurement series for devices around a coupling length of $23\ \mu m$ and $5.5\ \mu m$. R_e is calculated from transmission measurements at port *C2*. The splitting ratios of the directional couplers are close to 50%, if R_e starts to diverge, thus indicating nearly perfect constructive interference (see Equation C.1). Wavelength regions with high R_e are colored red.

D: Simulations of Photonic Crystal Nanobeam Cavity Devices[5]

Numerical Simulations of PCNBC

The PCNBC exhibits several geometric parameters which critically affect the cavity mode and hence the coupling efficiency of the CNT light emission. For the computation of a photonic crystal band structure, a plane wave eigensolver method was used. The simulation was performed in three-dimensional space using the MIT Photonic Bands (MPB) software. A suitable waveguide geometry as well as the parameters for the modulated Bragg mirror (values for the width *w*, the period *a* and the PCH radius *r*) were calculated both for dielectric and air mode PCNBC-devices.

After determining the parameters for PCNBC the resulting cavity modes were analyzed by finite difference time domain (FDTD) simulations using the MIT Electromagnetic Equation Propagation (MEEP) software. The simulations were carried out full-vectorial in three dimensions using high grid resolution both for air and dielectric mode cavities. The CNT emitter was modeled as an elongated dipole source with dimensions corresponding to the real CNT emitters, placed in the center of the cavity. The transmission spectra (for external light source, Figures 3.23c and 3.24c) and the LDOS spectra (for internal light source with different locations, Figures 3.23f and 3.24f) were simulated. To alleviate the time requirements, the simulated structures had less mirror segments N_{PCH} than in the fabricated devices (24 and 30 for air and dielectric mode cavities instead of 40-50) resulting in reduced Q factors in the simulated spectra. Profiles of fundamental and second order modes were calculated (Figures 3.23a,b and 3.24a,b). The influence of the N_{PCH} and the distance to the metal contacts on the Q factor for different modes was investigated (Figures 3.26 and D.2a,b).

[5] adapted from (12), performed by V. Fütterling.

PCNBC Design and Band Structure Calculation

A suitable cavity, which targets a specific resonance frequency ω_{res}, can be designed by stringing together individual periods of different photonic crystals in such a way that a linear increase of the mirror strength γ with the period index n = 1, 2..., N is obtained, where N is the total number of periods on either side of the cavity (N_{PCH} = 2N). The mirror strength should be zero for the period with n = 1 at the cavity center, and maximized for the two terminating segments on both sides of the cavity with n = N. It has also been noted, that γ can be calculated from the band diagram of a photonic crystal (144):

$$\gamma = \sqrt{\frac{(\omega_2 - \omega_1)^2}{(\omega_2 + \omega_1)^2} - \frac{(\omega_{res} - \omega_0)^2}{{\omega_0}^2}} \qquad (D.1)$$

where ω_2, ω_1 and $\omega_0 = (\omega_2 - \omega_1)/2$ are the air band edge, the dielectric band edge and the mid-gap frequency, respectively, and ω_{res} is the resonance frequency of the cavity. Alternatively, γ can be obtained directly from FDTD simulations.

For the computation of a photonic crystal band structure the planewave eigensolver method was used, which solves the Maxwell eigenproblem of a periodic system, yielding the various frequency bands $\omega_{n,k}$ for a specific wave vector k. By sampling the first Brillouin zone (1.BZ) with a sufficiently large number of discrete wave vectors, a good approximation of the band structure was obtained and the band gaps became visible. Figure D.1a visualizes the basic geometry of the dielectric function in the unit cell and Figure D.1b visualizes the domain for the finite-difference time-domain (FDTD) simulation. In the following, the parameter search of an exemplary PCNBC is described for a target resonance frequency of $\omega_{res} = 306\,\mathrm{THz}$, corresponding to a wavelength of $\lambda_{res} = 0.98\,\mu\mathrm{m}$.

Since the photonic crystal cavity is a structure inside an air suspended waveguide, the first step was to find a suitable waveguide geometry, which only has a single guided transverse-electrical (TE) mode in the frequency range of interest. Preventing the scattering of light to higher order modes is important to increase the Q factor of the fundamental mode. Since the waveguide has continuous translational symmetry, its band structure can also be calculated with the plane wave solver by reducing the

problem to the cross section plane, effectively setting the period length to zero. Because the height of the material used in the experiments was fixed to 0.2 µm, only the width of the waveguide was adjustable. Accordingly, the waveguide band structure was determined for several widths only, and an adequate result was obtained for a width of $w = 0.6$ µm.

In the second step, the parameters for the modulated Bragg mirror were calculated. Considering a single segment of a one-dimensional photonic crystal inside a waveguide, there were basically three parameters that influenced its band structure. These parameters were the width w, the period a and the hole radius r, or more generally the filling fraction $ff = \pi r^2 / \omega a$.

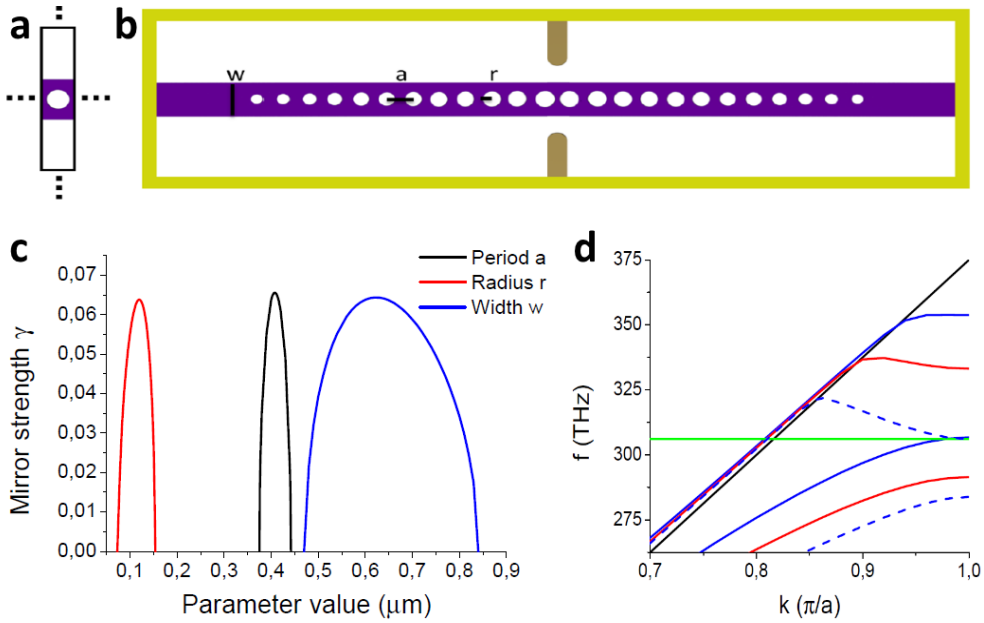

Figure D.1 | Cavity design and band structure calculation.

(a) Top view of the simulation domains for photonic crystal band structure simulation with MPB (supercell with periodic boundary conditions).
(b) Top view of the time domain simulation with MEEP. The yellow border represents an absorbing boundary condition (PML). Parameters width w, period a, and radius r are indicated.
(c) Mirror strength as a function of the hole radius r (red), the waveguide width w (blue) and the photonic crystal period a (black). The resonance wavelength is 0.98 µm, the base parameters are $r = 0.119$ µm, $w = 0.6$ µm and $a = 0.4$ µm.
(d) Band diagrams inside the 1.BZ for the inner (n = 1, blue lines) and outer (n = N, red lines) Bragg mirror segments. The inner segment can be either a dielectric segment (solid lines) or an air segment (dashed lines). The light line is indicated by the black line, and the target frequency by the green line.

Modifications of the height h would also affect the band structure, however from a fabrication point of view this would not be a practical approach because there is only one thickness available on a wafer. It is sufficient to vary only one of the parameters and keep the others fixed at their base values. The base values for h = 0.2 μm and w = 0.6 μm were predetermined by the waveguide, the values for the radius r = 0.119 μm and period a = 0.4 μm was chosen after some experimentation. By calculating the band structures for a reasonable range of parameter values and deriving the mirror strength with the help of Equation D.1 the result in Figure D.1c was obtained. The mirror strength γ has a certain parameter range in which it is different from zero, with a sharp rise at the boundaries and a maximum at the center.

It follows, that there are two ways to construct the modulated Bragg mirror, resulting in two different cavities, which are distinguished as air mode cavity and dielectric mode cavity. For the air mode cavity, the inner segment (n = 1) modulated parameter corresponds to the value just below the lower boundary, while for the dielectric mode cavity the value just above the upper boundary has to be used as the inner segment. The outer segment (n = N) is derived from the maximum mirror strength in both cases. Hence, in the case of a radius modulation, the air mode cavity has large radii at the outside and small radii at the inside, while the for the dielectric mode cavity the progression of the radii is reversed. The same principle applies to the modulation of the width and period parameters.

Figure D.1d illustrates the band diagram for the inner and outer Bragg mirror segments. The red band structure corresponds to the outer segment (n = N). The black line indicates the light cone, and the green line the target frequency, which is situated inside the bandgap of the outer segment. For the inner segment (n = 1) there are two band structures in blue, with solid lines for the dielectric mode and dashed lines for the air mode. For the dielectric mode, the dielectric band edge is located at the target frequency, while for the air mode the air band edge is located at the target frequency. The key observation is that for both cases the propagating mode of the inner segment is confined by the bandgap of the outer segment.

Mode Profiles for PCNBC Devices

In order to achieve strong coupling between the CNT and the cavity, the dipole of the CNT emission must be aligned to the polarisation of electric field (*E)* mode of the cavity and located at an antinode of the mode. By placing the CNT at the center of the cavity, oriented perpendicular to the waveguide (y-axis), the dominant longitudinally polarized emission of the CNT can couple to a symmetric transverse-electric (TE) cavity mode (E_x, $E_y \neq 0$), which has its strongest antinode at the cavity center. The transversely polarized component in the direction of the waveguide (x-axis) can also couple to the TE mode, however the coupling of out-of-plane emission (z-axis) is suppressed because $E_z \approx 0$. In the case an asymmetric TE mode, a field node is located at the center of the cavity, while the antinodes are shifted to the left and to the right, and the coupling is reduced.

Figure 3.23a depicts the E_y field pattern of the fundamental dielectric mode for $N_{PCH} = 50$. The center of the cavity is indicated by the black line, which obviously corresponds to the position of an antinode in the field pattern. In contrast, the E_y field pattern for the fundamental air mode (Figure 3.24a) is asymmetric with a field node located at the cavity center. Hence, a considerable reduction in the coupling strength to the CNT emission can be expected. However, the even symmetry of the second order air mode gives rise to an antinode at the cavity center as depicted in Figure 3.24b. Still, this mode is not optimal either, because despite the even symmetry, the envelope of the mode has a node at the cavity center, reducing the field intensity. For the second order dielectric mode in Figure 3.23b, the mode profile is even less suitable for CNT coupling, because both a field node and an envelope minimum are located at the cavity center. Thus, the best coupling strength can be expected from the dielectric fundamental mode.

Resonance Wavelength and Q Factor: Simulation and Experiment

Two the most important parameters of the PCNBC structures are the resonance wavelengths and Q factor. The resonance spectrum and the corresponding Q factors both for the air mode (w = 0.6 μm, a = 0.43 μm, ff_1 = 0.13, ff_N = 0.26, λ_{target} = 985 nm) and for the dielectric mode cavities (w = 0.6 μm, a = 0.39 μm, ff_1 = 0.2775, ff_N = 0.165, λ_{target} = 975 nm). The resonance wavelength λ_{res} of the fundamental mode and the corresponding Q factor are illustrated in Figure D.2a,b, as a function of the number of mirror segments N on either side of the cavity. As expected, the Q factor increases with N for both the dielectric mode and air mode cavity. The increase is exponential over a large range of N (linear on the logarithmic plot), deviating slightly for the smallest and largest number of mirror segments. A larger N reduces the waveguide losses because the evanescent field of the cavity mode decays over a longer distance before reaching the propagating part of the waveguide. Additionally, the change of the filling fraction from segment to segment is more gradual, reducing the high frequency components of the k-spectrum inside the light cone at the center of the 1.BZ which in turn reduces the radiation loss. While the dielectric mode exhibits a Q factor of about 10^6 at N = 30, the air mode reaches the same Q factor of about10^6 with 5 mirror segments less on either side of the cavity.

This difference can be attributed to two effects: First, the maximum mirror strength γ_N of the outer segment n = N is higher in the case of the air mode, resulting from a combination of larger period and higher filling fraction compared to the dielectric mode. If the same configuration was used for the dielectric mode, the required filling fraction ff_1 of the inner segment n = 1 would result in a hole diameter larger than a single period. Second, due to the significantly smaller filling fraction in the cavity center, the effective refractive index n_{eff} of the air mode is larger compared to the dielectric mode, leading to stronger confinement and reduced radiation loss.

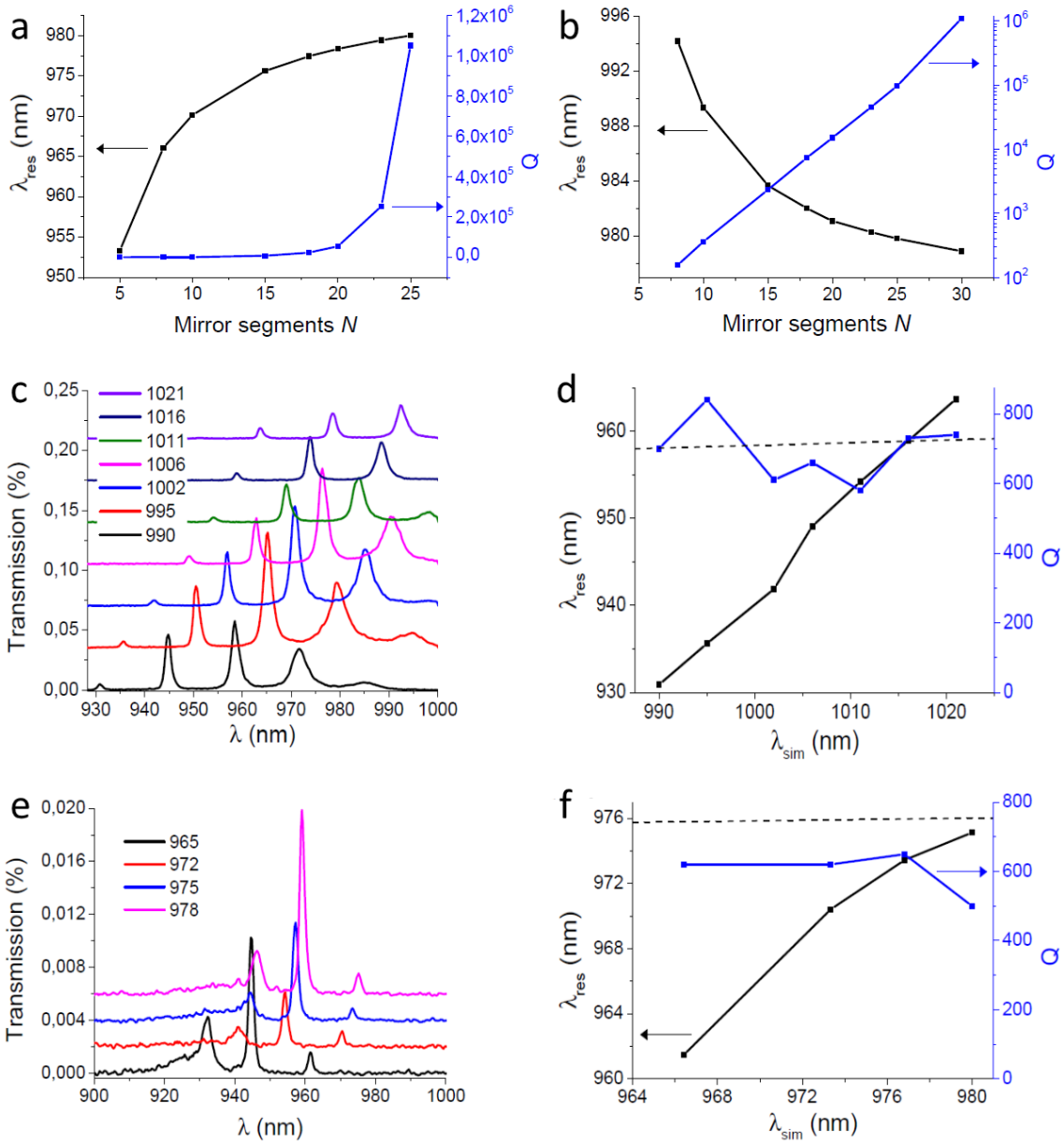

Figure D.2 | Resonance wavelength λ_{res} and Q factor.

(a) As function of N = NPC/2 for an air mode cavity.
(b) As a function of dielectric mode cavity.
(c) Comparison of dielectric mode PCNBC devices designed for 5 nm separation in the fundamental resonance wavelength λ_{sim} . Transmission spectra of the devices with the corresponding simulated resonance wavelength indicated in the inset, graphs are offset along the y-axis.
(d) Plot of the measured fundamental resonance λ_{res} and the corresponding Q factors as a function of the simulated value λ_{sim} for dielectric mode PCNBC devices. The dashed line indicates the Q factor corresponding to the detector linewidth.
(e) Comparison of air mode PCNBC devices designed for 5 nm separation in the fundamental resonance wavelength. Transmission spectra of the devices with the corresponding simulated resonance wavelength λ_{sim} indicated in the inset, graphs are offset along the y-axis.
(f) Plot of the measured fundamental resonance λ_{res} and the corresponding Q factors as a function of the simulated value λ_{sim} for air mode PCNBC devices.

Figure D.2a,b, also shows a systematic shift for the resonance wavelength λ_{res} between different N. For smaller N, λ_{res} shifts away from the bandgap towards smaller wavelengths for the air mode and towards larger wavelengths for the dielectric mode. For large N, λ_{res} asymptotically approaches the band edge of the inner segment n = 1. The explanation is that for small N, the cavity mode is more strongly located in the mirror region with a stronger γ, and thus in mirror segments with band edges more distant to the band edge of the inner segment. Accordingly, the mode shifts with the band edges. For large N, the mirror strength changes slower in the center of the cavity, the shift is reduced, and the result are two modes with a resonance at exactly 980 nm, even though the air mode has been targeted at 985 nm and the dielectric mode at 975 nm.

After fabrication process, the transmission through the samples is measured and the experimental values of resonance wavelength and Q factor can be achieved. Figure D.2c depicts the transmission spectra for 7 cavity designs (test sample without electrodes), offset along the y-axis. The spectra all appear qualitatively similar, with 5 clear resonances visible, except for the spectra shifted out of detector range at 1000 nm. The inset shows the time domain simulation results for the fundamental reference wavelengths. As can be seen, the shift between λ_{res} and λ_{sim} is around 60 nm due to reduced waveguide width and increased hole size with respect to the intended design parameters. However, shift between the spectra follows the intended design, which is confirmed by Figure D.2d, depicting λ_{res} as a function of λ_{sim}. For perfect agreement with the simulation, the line slope should be exactly one, which is true for the upper part of the line, but disturbed by an offset of the lower part. This discrepancy is within the range of fabrication variations, and the overall result confirms, that the design by bandgap simulation is quite successful also in experiment.

The Figure D.2d also shows the measured Q factors (obtained from Lorentzian fit) of the fundamental modes. The resolution of the used spectrometer is limited to 1.3 nm FWHM, corresponding to a Q factor as indicated by the dashed line. In the case of a high experimental Q factor, the measured resonance spectrum has the linewidth of the spectrometer, and the intensity of the peak is an indication of the true experimental Q factor. If two detector-limited resonance peaks are measured, the resonance with the distinctly higher true Q factor should have lower peak intensity, because the

spectrometer returns the convolution of the detector line profile with the true resonance shape, which results in a smaller value for higher Q factors. This case can be observed for all of the presented spectra in this section, by comparing the Q factors of the fundamental mode with the Q factor of the second order mode. The average Q factors for the spectra in Figure D.2c are almost equal, with $Q_1 \approx 700$ for the fundamental, and $Q_2 \approx 660$ for the second order mode (not shown), yet the peak intensity is significantly higher for the latter. The ratio Q_1/Q_2 obtained from the simulations is ≈ 10 on average, suggesting that the experimentally observed ratio is too small to be accurate, even considering loss from surface roughness and fabrication imperfections. This further indicates that the measurement results are spectrometer limited, at least for Q_1 but probably also for Q_2. Since the convolution of two Lorentzian peaks with linewidths γ_0 and γ_1 yields another Lorentzian with linewidth $\gamma_0 + \gamma_1$, a measured Q factor is already limited below the spectrometer limit. Only for Q factors well below this limit, the true value is approached in experiment. This can be observed for the fourth order peaks, which show Q factors in the range from 200 to 300, overlapping with the results from the simulations.

Returning back to Figure D.2d, the measured Q factors are all close to dashed limit. Since it is difficult to analyze resonance peaks significantly influenced by the spectrometer line profile, the discussion of the Q factors has to remain qualitative. The essence is that the true cavity Q factors are likely higher than the measurements indicate, and that the available measurement equipment is not sufficient for a quantitative analysis in the spectral range of interest.

Design of PCNBC-Samples

The sample contains more than 150 PCNBC devices arranged in 9 rows (Figure D.3). The design of the devices is crafted by the band structure simulation method with fundamental resonance wavelengths in the range of 975 nm to 1050 nm (dielectric mode cavities, rows **a, b, e**, **f**) or 965 to 1040 nm (air mode cavities, rows **c, d, g**, **h**) evenly separated by 5 nm. N_{PC} is either 40 (rows **a, c, e, g**) or 50 (rows **b, d, f, h**). Devices arranged in the row **i** have asymmetrical photonic crystal mirror geometry (20 holes in the shorter half and 35 holes in the longer half of the cavity, Figure 3.22b). The gap between metal contact and waveguide varies among 0.2 µm (rows **a, b, c, d**) and 0.3/0.4 µm (rows **e, f, g, h**), the waveguide width was 600 nm for all devices. The sample comprises even number of dielectric and air mode cavities with different fundamental resonance wavelengths designed in varying steps of 5 nm.

Row	Cavity mode	N_{PC}	Gap, µm
A	Dielectric	40	0.2
B	Dielectric	50	0.2
C	Air	40	0.2
D	Air	50	0.2
E	Dielectric	40	0.3-0.4
F	Dielectric	50	0.3-0.4
G	Air	40	0.3-0.4
H	Air	50	0.3-0.4
I	Both typs	40+15	0.2-0.3

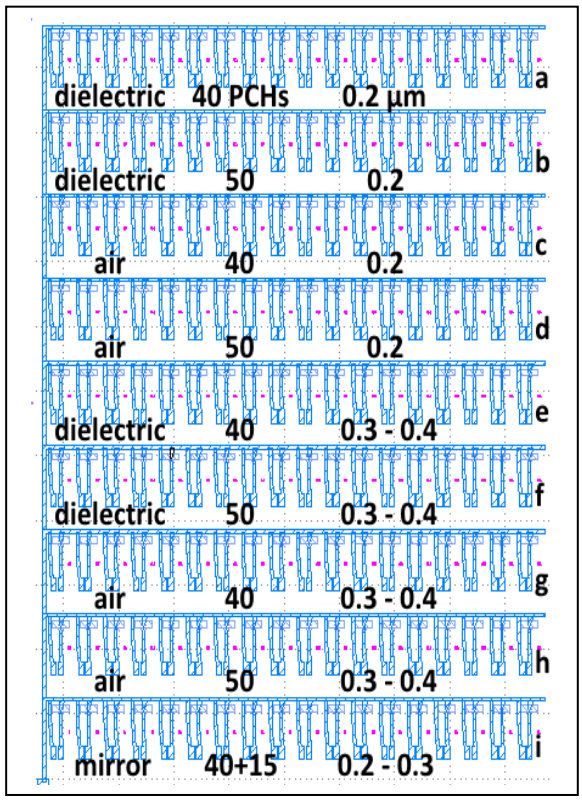

Figure D.3 | PCNBC device overview.

The devices differ in the cavity mode, NPCH and gap between metal contact and waveguide.

List of Figures

List of Abbreviations

ac (dc)	alternating (direct) current
AFM	atomic force microscopy
a.u.	arbitrary units
CMOS	complementary metal-oxide-semiconductor
CNT	(single walled) carbon nanotube
CVD	chemical vapour deposition
DC	directional coupler
DEP	dielectrophoresis
EL	electroluminescence
FDTD	finite-difference time-domain
FET	field-effect transistor
FSR	free spectral range
FWHM	full width at half maximum
LDOS	local density of states
MeCNT	metallic carbon nanotube
MZI	Mach-Zehnder interferometer
NIR	near-infrared
NPIC	nanophotonic integrated circuits
PC	photonic crystal
PCH	photonic crystal hole
PCNBC	photonic crystal nanobeam cavity
PL	photoluminescence
RIE	reactive ion etching
SCCNT	semiconducting carbon nanotube
SEM	scanning electron microscopy
SPD	single photon detector
TCSPC	time-correlated single photon counting
WINS	waveguide-integrated carbon nanotube light source

Bibliography

1. O'Mahony MJ, Politi C, Klonidis D, Nejabati R, Simeonidou D. Future optical networks. J Light Technol. 2006;24(12):4684–96.
2. Vlasov Y, Green WMJ, Xia F. High-throughput silicon nanophotonic deflection switch for on-chip optical networks. Nat Photonics. 2008;2:242–6.
3. Lipson M. Guiding, modulating, and emitting light on Silicon - challenges and opportunities: Lightwave Technology, J Light Technol. 2005;23(12):4222–38.
4. Kopp C, Bernabé S, Bakir BB, Fedeli JM, Orobtchouk R, Schrank F, et al. Silicon photonic circuits: On-CMOS integration, fiber optical coupling, and packaging. IEEE J Sel Top Quantum Electron. 2011;17(3):498–509.
5. Jewell JL, Lee YH, Harbison JP, Scherer A, Florez LT. Vertical-cavity surface-emitting lasers: Design, growth, fabrication, characterization. IEEE J Quantum Electron. 1991;27(6):1332–46.
6. McCall SL, Levi AFJ, Slusher RE, Pearton SJ, Logan RA. Whispering-gallery mode microdisk lasers. Appl Phys Lett. 1992;60(3):289–91.
7. Painter O, Lee RK, Scherer A, Yariv A, O'Brien JD, Dapkus PD, et al. Two-dimensional photonic band-gap defect mode laser. Science. 1999;284:1819-21.
8. Jorio A, Dresselhaus G, Dresselhaus MS. Carbon nanotubes. 2008.
9. Vijayaraghavan A, Blatt S, Weissenberger D, Oron-Carl M, Hennrich F, Gerthsen D, et al. Ultra-large-scale directed assembly of single-walled carbon nanotube devices. Nano Lett. 2007;7(6):1556–60.
10. Khasminskaya S, Pyatkov F, Flavel BS, Pernice WHP, Krupke R. Waveguide-integrated light-emitting carbon nanotubes. Adv Mater. 2014;26(21):3465–72.
11. Fechner RG, Pyatkov F, Khasminskaya S, Flavel BS, Krupke R, Pernice WHP. Directional couplers with integrated carbon nanotube incandescent light emitters. Opt Express. 2016;24(2):966–74.
12. Pyatkov F, Fütterling V, Khasminskaya S, Flavel BS, Krupke R, Pernice WHP. Cavity enhanced light emission from electrically driven carbon nanotubes. Nat Photonics. 2016;10:420–7.

13. Pyatkov F, Khasminskaya S, Kovalyuk V, Hennrich F, Kappes MM, Goltsman GN, et al. Sub-nanosecond light pulse generation with waveguide-coupled carbon nanotube transducers. Beilstein J Nanotechnol. 2017;8:38-44.
14. Alamgir IM, Pyatkov F, Riaz A, Dehm S, Hennrich F, Kappes MM, Krupke R. Near-infrared electroluminescence of large diameter carbon nanotubes (unpublished).
15. Khasminskaya S, Pyatkov F, Slowik K, Ferrari S, Kahl O, Kovalyuk V, et al. Fully integrated quantum photonic circuit with an electrically driven light source. Nat Photonics. 2016;10:727–32.
16. Iijima S. Helical microtubules of graphitic carbon. Nature. 1991;354(6348):56–8.
17. Monthioux M. Filling single-wall carbon nanotubes. Carbon. 2002;40(10):1809-23.
18. Balasubramanian K, Burghard M. Chemically functionalized carbon nanotubes. Small. 2005;1(2):180–92.
19. Meng L, Fu C, Lu Q. Advanced technology for functionalization of carbon nanotubes. Prog Nat Sci. National Natural Science Foundation of China and Chinese Academy of Sciences; 2009;19(7):801–10.
20. Blinder SM. “Carbon Nanotubes” from the Wolfram Demonstrations Project http://demonstrations.wolfram.com/CarbonNanotubes/.
21. Journet C, Maser WK, Bernier P, Loiseau A. Large-scale production of single-walled carbon nanotubes by the electric-arc technique. Nature. 1997;388:20–2.
22. Guo T, Nikolaev P, Thess A, Colbert DT, Smalley RE. Catalytic growth of single-walled manotubes by laser vaporization. Chem Phys Lett. 1995;243(1-2):49–54.
23. Kong J, Cassell AM, Dai H. Chemical vapor deposition of methane for single-walled carbon nanotubes. Chem Phys Lett. 1998;292(4-6):567–74.
24. Yang F, Wang X, Zhang D, Yang J, Luo D, Xu Z, et al. Chirality-specific growth of single-walled carbon nanotubes on solid alloy catalysts. Nature. 2014;510(7506):522–4.
25. Taczak MD. Controlling the structure and properties of carbon nanotubes. MITRE Corporations, the MITRE Nanosystems Group, www.mitre.org/tech/nanotech. 2007.

26. Lambert JM, Ajayan PM, Bernier P, Planeix JM, Brotons V, Coq B, et al. Improving conditions towards isolating single-shell carbon nanotubes. Chem Phys Lett. 1994;226(3-4):364–71.
27. Xu YQ, Peng H, Hauge RH, Smalley RE. Controlled multistep purification of single-walled carbon nanotubes. Nano Lett. 2005;5(1):163–8.
28. Nish A, Hwang J-Y, Doig J, Nicholas RJ. Highly selective dispersion of single-walled carbon nanotubes using aromatic polymers. Nat Nanotechnol. 2007;2(10):640–6.
29. Arnold MS, Green A a, Hulvat JF, Stupp SI, Hersam MC. Sorting carbon nanotubes by electronic structure using density differentiation. Nat Nanotechnol. 2006;1(1):60–5.
30. Flavel BS, Moore KE, Pfohl M, Kappes MM, Hennrich F. Separation of single-walled carbon nanotubes with a gel permeation chromatography system. ACS Nano. 2014;8(2):1817–26.
31. Hennrich F, Li W, Fischer R, Lebedkin S, Krupke R, Kappes MM. Length sorted, large-diameter, polyfluorene-wrapped semiconducting single-walled carbon nanotubes for high density short channel transistors. ACS Nano. 2016;10:1888–95.
32. Reich S, Thomsen C, Maultzsch J. Carbon nanotubes. Basis concepts and physical properties. WILEY-VCH. 2004.
33. Charlier JC, Blase X, Roche S. Electronic and transport properties of nanotubes. Rev Mod Phys. 2007;79(2):677–732.
34. Bachilo SM, Strano MS, Kittrell C, Hauge RH, Smalley RE, Weisman RB. Structure-assigned optical spectra of single-walled carbon nanotubes. Science. 2002;298(5602):2361–6.
35. Spataru CD, Ismail-Beigi S, Benedict LX, Louie SG. Excitonic effects and optical spectra of single-walled carbon nanotubes. Phys Rev Lett. 2004;92(7):4.
36. Matsunaga R, Matsuda K, Kanemitsu Y. Observation of charged excitons in hole-doped carbon nanotubes using photoluminescence and absorption spectroscopy. Phys Rev Lett. 2011;106(3):1–4.

37. Kataura H, Kumazawa Y, Maniwa Y, Umezu I, Suzuki S, Ohtsuka Y, et al. Optical properties of single-wall carbon nanotubes. Synth Met. 1999;103:1–4.
38. O'Connell MJ et al. Band gap fluorescence from individual single-walled carbon nanotubes. Science. 2002;297:593–6.
39. Fantini C, Jorio A, Souza M, Strano MS, Dresselhaus MS, Pimenta MA. Optical transition energies for carbon nanotubes from resonant raman spectroscopy: Environment and temperature effects. Phys Rev Lett. 2004;93(14):1–4.
40. Weisman RB, Bachilo SM. Dependence of optical transition energies on structure for single-walled carbon nanotubes in aqueous suspension: An empirical Kataura plot. Nano Lett. 2003;3(9):12355-8.
41. Flavel BS, Kappes MM, Krupke R, Hennrich F. Separation of single-walled carbon nanotubes by 1-dodecanol-mediated size-exclusion chromatography. ACS Nano. 2013;7(4):3557–64.
42. Hertel T, Himmelein S, Ackermann T, Stich D, Crochet J. Diffusion limited photoluminescence quantum yields in 1-D semiconductors: Single-wall carbon nanotubes. ACS Nano. 2010;4(12):7161–8.
43. Harrah DM, Swan AK. The role of length and defects on optical quantum efficiency and exciton decay dynamics in single-walled carbon nanotubes. ACS Nano. 2011;5(1):647–55.
44. Berger S, Voisin C, Cassabois G, Delalande C, Roussignol P, Marie X. Temperature dependence of exciton recombination in semiconducting single-wall carbon nanotubes. Nano Lett. 2007;7(2):398–402.
45. Schweiger M, Zakharko Y, Gannott F, Grimm SB, Zaumseil J. Photoluminescence enhancement of aligned arrays of single-walled carbon nanotubes by polymer transfer. Nanoscale. 2015;7(40):16715–20.
46. Ma X, Adamska L, Yamaguchi H, Yalcin SE, Tretiak S, Doorn SK, et al. Electronic structure and chemical nature of oxygen dopant states in carbon nanotubes. ACS Nano. 2014;8(10):10782–9.
47. Avouris P, Freitag M, Perebeinos V. Carbon-nanotube photonics and optoelectronics. Nat Photonics. 2008;2(6):341–50.
48. Misewich JA, Martel R, Avouris P, Tsang JC, Heinze S, Tersoff J. Electrically induced optical emission from a carbon nanotube FET. Science. 2003;300(5620):783–6.

49. Freitag M, Perebeinos V, Chen J, Stein A, Tsang JC, Misewich JA, et al. Hot carrier electroluminescence from a single carbon nanotube. Nano Lett. 2004;4(6):1063–6.
50. Mueller T, Kinoshita M, Steiner M, Perebeinos V, Bol A a, Farmer DB, et al. Efficient narrow-band light emission from a single carbon nanotube p-n diode. Nat Nanotechnol. 2010;5(1):27–31.
51. Kinoshita M, Steiner M, Engel M, Small JP, Green A a, Hersam MC, et al. The polarized carbon nanotube thin film LED. Opt Express. 2010;18(25):25738–45.
52. Hughes M a., Ohno Y, Mizutani T. Electroluminescence from an electrostatically doped carbon nanotube field-effect transistor. Nanosci Nanotechnol Lett. 2014;6(10):881–6.
53. Marty L, Adam E, Albert L, Doyon R, Menard D, Martel R. Exciton formation and annihilation during 1D impact excitation of carbon nanotubes. Phys Rev Lett. 2006;96(13):2–5.
54. Chen J, Perebeinos V, Freitag M, Tsang J, Fu Q, Liu J, et al. Bright infrared emission from electrically induced excitons in carbon nanotubes. Science. 2005;310(5751):1171–4.
55. Lefebvre J, Austing DG, Bond J, Finnie P. Photoluminescence imaging of suspended single-walled carbon nanotubes. Nano Lett. 2006;6(8):1603–8.
56. Tsyboulski DA, Rocha J-DR, Bachilo SM, Cognet L, Weisman RB. Structure-dependent fluorescence efficiencies of individual single-walled carbon nanotubes. Nano Lett. 2007;7(10):3080–5.
57. Stewart D a., Léonard F. Energy conversion efficiency in nanotube optoelectronics. Nano Lett. 2005;5(2):219–22.
58. Freitag M, Steiner M, Naumov A, Small JP, Bol A a, Perebeinos V, et al. Carbon nanotube photo- and electroluminescence in longitudinal electric fields. ACS Nano. 2009;3(11):3744–8.
59. Lefebvre J, Fraser J, Finnie P, Homma Y. Photoluminescence from an individual single-walled carbon nanotube. Phys Rev B. 2004;69(7):1–5.
60. Ma Z, Liang S, Liu Y, Wang F, Wang S, Peng L-M. On-chip polarized light emitters based on (6,5) chirality-sorted carbon nanotube aligned arrays. Appl Phys Lett. 2016;108(6):063114.

61. Liang S, Ma Z, Wei N, Liu H, Wang S, Peng L-M. Solid state carbon nanotube device for controllable trion electroluminescence emission. Nanoscale. 2016;8(12):6761–9.
62. Jakubka F, Grimm SB, Zakharko Y, Gannott F, Zaumseil J. Trion electroluminescence from semiconducting carbon nanotubes. ACS Nano. 2014;8(8):8477–86.
63. Mann DA, Kato YK, Kinkhabwala A, Pop E, Cao J, Wang X, et al. Electrically driven thermal light emission from individual single-walled carbon nanotubes. Nat Nanotechnol. 2007;2(1):33–8.
64. Liu Z, Bushmaker A, Aykol M, Cronin SB. Thermal emission spectra from individual suspended carbon nanotubes. ACS Nano. 2011;5(6):4634–40.
65. Pop E, Mann DA, Cao J, Wang Q, Goodson K, Dai H. Negative differential conductance and hot phonons in suspended nanotube molecular wires. Phys Rev Lett. 2005;155505:1–4.
66. Mori T, Yamauchi Y, Honda S, Maki H. An electrically driven, ultrahigh-speed, on-chip light emitter based on carbon nanotubes. Nano Lett. 2014;14(6):3277-83.
67. Wang X, Zhang L, Lu Y, Dai H, Kato YK, Pop E. Electrically driven light emission from hot single-walled carbon nanotubes at various temperatures and ambient pressures. Appl Phys Lett. 2007;91(26):3–5.
68. Hata K, Futaba D, Mizuno K, Namai T, Yumura M, Iijima S. Water-assisted highly efficient synthesis of impurity-free single-walled carbon nanotubes. Science. 2004;306(5700):1362–4.
69. Pop E, Mann DA, Wang Q, Goodson K, Dai H. Thermal conductance of an individual single-wall carbon nanotube above room temperature. Nano Lett. 2006;6(1):96–100.
70. Hepplestone SP, Ciavarella AM, Janke C, Srivastava GP. Size and temperature dependence of the specific heat capacity of carbon nanotubes. Surf Sci. 2006;600(18):3633–6.
71. Yao Z, Kane C, Dekker C. High-field electrical transport in single-wall carbon nanotubes. Phys Rev Lett. 2000;84(13):2941–4.
72. Bennett CH, Brassard G. Quantum cryptography: public key distribution and coin tossing. Int Conf Computers, Systems and Signal Processing, Bangalore, India. 1984.

73. Beveratos A, Brouri R, Gacoin T, Villing A, Poizat J-P, Grangier P. Single photon quantum cryptography. Phys Rev Lett. 2002;89(18):187901.
74. O'Brien JL, Furusawa A, Vučković J. Photonic quantum technologies. Nat Photonics. 2009;3(12):687–95.
75. Aspuru-Guzik A, Walther P. Photonic quantum simulators. Nat Phys. 2012;8(4):285–91.
76. Eisaman MD, Fan J, Migdall A, Polyakov SV. Single-photon sources and detectors. Rev Sci Instrum. 2011;82:071101.
77. Högele A, Galland C, Winger M, Imamoğlu A. Photon antibunching in the photoluminescence spectra of a single carbon nanotube. Phys Rev Lett. 2008;100(21):5–8.
78. Hofmann MS, Glückert JT, Noé J, Bourjau C, Dehmel R, Högele A. Bright, long-lived and coherent excitons in carbon nanotube quantum dots. Nat Nanotechnol. 2013;8(7):502–5.
79. Ma X, Hartmann NF, Baldwin JKS, Doorn SK, Htoon H. Room-temperature single-photon generation from solitary dopants of carbon nanotubes. Nat Nanotechnol. 2015;10(8):671–5.
80. Ma X, Roslyak O, Duque JG, Pang X, Doorn SK, Piryatinski A, et al. Influences of exciton diffusion and exciton-exciton annihilation on photon emission statistics of carbon nanotubes. Phys Rev Lett. 2015;115(1):1–6.
81. Endo T, Ishi-Hayase J, Maki H. Photon antibunching in single-walled carbon nanotubes at telecommunication wavelengths and room temperature. Appl Phys Lett. 2015;106(11):1–6.
82. Walden-Newman W, Sarpkaya I, Strauf S. Quantum light signatures and nanosecond spectral diffusion from cavity-embedded carbon nanotubes. Nano Lett. 2012;12(4):1934–41.
83. Sarpkaya I, Zhang Z, Walden-Newman W, Wang X, Hone J, Wong CW, et al. Prolonged spontaneous emission and dephasing of localized excitons in air-bridged carbon nanotubes. Nat Commun. 2013;4:2152.
84. Hofmann MS, Noé J, Kneer A, Crochet JJ, Högele A. Ubiquity of exciton localization in cryogenic carbon nanotubes. Nano Lett. 2016;16(5):2958-62.
85. Hambury Brown R, Twiss RQ. Correlation between photons in two coherent beams of light. Nature. 1956;177:27–9.

86. Javey A, Shim M, Dai H. Electrical properties and devices of large-diameter single-walled carbon nanotubes. Appl Phys Lett. 2002;80(6):1064–6.
87. Liu X, Lee C, Zhou C, Han J. Carbon nanotube field-effect inverters. Appl Phys Lett. 2001;79(20):3329–31.
88. Miura R, Imamura S, Ohta R, Ishii A, Liu X, Shimada T, et al. Ultralow mode-volume photonic crystal nanobeam cavities for high efficiency coupling to individual carbon nanotube emitters. Nat Commun. 2014;5(c):1–4.
89. Tans S, Verschueren A, Dekker C. Room-temperature transistor based on a single carbon nanotube. Nature. 1998;672(1989):669–72.
90. Bachtold A, Hadley P, Nakanishi T, Dekker C. Logic circuits with carbon nanotube transistors. Science. 2001;294(5545):1317–20.
91. Yeshua T, Lehmann C, Hübner U, Azoubel S, Magdassi S, Campbell EEB, et al. Nanodrawing of aligned single carbon nanotubes with a nanopen. Nano Lett. 2016;16(3):1517-22.
92. Penzo E, Palma M, Wang R, Cai H, Zheng M, Wind SJ. Directed assembly of end-functionalized single wall carbon nanotube segments. Nano Lett. 2015;15(10):6547–52.
93. Penzo E, Palma M, Chenet DA, Ao G, Zheng M, Hone JC, et al. Directed assembly of single wall carbon nanotube field effect transistors. ACS Nano. 2016;10(2):2975–81.
94. Pohl HA. The motion and precipitation of suspensoids in divergent electric fields. J Appl Phys. 1951;22(7):869–71.
95. Krupke R, Hennrich F, Kappes MM, Löhneysen H V. Surface conductance induced dielectrophoresis of semiconducting single-walled carbon nanotubes. Nano Lett. 2004;4(8):1395–9.
96. Krupke R, Hennrich F, Loehneysen H V., Kappes MM. Separation of metallic from semiconducting single-walled carbon nanotubes. Science. 2003;301(5631):344–7.
97. Hecht E. Optics. 4th edition. AddisonWesley Publishing Company. 2001.
98. Vahala KJ. Optical microcavities. Nature. 2003;424(6950):839–46.
99. Purcell E, Torrey H, Pound R. Resonance absorption by nuclear magnetic moments in a solid. Phys Rev. 1946;69(1-2):37–8.

100. Christofilos D, Blancon JC, Arvanitidis J, Miguel AS, Ayari A, Del Fatti N, et al. Optical imaging and absolute absorption cross section measurement of individual nano-objects on opaque substrates: Single-wall carbon nanotubes on silicon. J Phys Chem Lett. 2012;3(9):1176–81.
101. International Telecommunications Union. Optical Fibres, Cables and Systems. 2009.
102. Gaufrès E, Izard N, Le Roux X, Kazaoui S, Marris-Morini D, Cassan E, et al. Optical microcavity with semiconducting single-wall carbon nanotubes. Opt Express. 2010;18(6):5740–5.
103. Watahiki R, Shimada T, Zhao P, Chiashi S, Iwamoto S, Arakawa Y, et al. Enhancement of carbon nanotube photoluminescence by photonic crystal nanocavities. Appl Phys Lett. 2012;101(14):56–9.
104. Imamura S, Watahiki R, Miura R, Shimada T, Kato YK. Optical control of individual carbon nanotube light emitters by spectral double resonance in silicon microdisk resonators. Appl Phys Lett. 2013;102(16):100–3.
105. Noury A, Roux X, Vivien L, Izard N. Enhanced light emission from carbon nanotubes integrated in silicon micro-resonator. Nanotechnology. 2015;26(34):345201.
106. Jeantet A, Chassagneux Y, Raynaud C, Roussignol P, Lauret J-S, et al. Widely tunable single-photon source from a carbon nanotube in the Purcell regime. Phys. Rev. Lett. 2016;116:247402.
107. Xia F, Steiner M, Lin Y-M, Avouris P. A microcavity-controlled, current-driven, on-chip nanotube emitter at infrared wavelengths. Nat Nanotechnol. 2008;3(10):609–13.
108. Gaufrè E, Izard N, Noury A, Roux XL, Rasigade G, Beck A, et al. Light emission in silicon from carbon nanotubes. ACS Nano. 2012;6(5):3813–9.
109. Bodiou L, Gu Q, Guézo M, Delcourt E, Batté T, Lemaitre J, et al. Guided Photoluminescence from integrated carbon-nanotube-based optical waveguides. Adv Mater. 2015;27(40):6181–6.
110. Liu K, Sorger VJ. Electrically-driven carbon nanotube-based plasmonic laser on silicon. Opt Mater Express. 2015;5(9):1910.

111. Böhmler M, Hartmann N, Georgi C, Hennrich F, Green AA, Hersam MC, et al. Enhancing and redirecting carbon nanotube photoluminescence by an optical antenna. Opt Express. 2010;18(16):16443–51.
112. Ingvarsson S, Klein L, Au Y-Y, Lacey J a, Hamann HF. Enhanced thermal emission from individual antenna-like nanoheaters. Opt Express. 2007;15(18):11249–54.
113. Moss DJ, Morandotti R, Gaeta AL, Lipson M. New CMOS-compatible platforms based on silicon nitride and Hydex for nonlinear optics. Nat Photonics. 2013;7(7):597–607.
114. Hochberg M, Baehr-Jones T. Towards fabless silicon photonics. Nat Photonics. 2010;4(8):492–4.
115. Stürzl N, Hennrich F, Lebedkin S, Kappes MM. Near monochiral single-walled carbon nanotube dispersions in organic solvents. J Phys Chem C. 2009;113(33):14628–32.
116. Moshammer K, Hennrich F, Kappes MM. Selective suspension in aqueous sodium dodecyl sulfate according to electronic structure type allows simple separation of metallic from semiconducting single-walled carbon nanotubes. Nano Res. 2009;2(8):599–606.
117. Ohno Y, Iwasaki S, Murakami Y, Kishimoto S, Maruyama S, Mizutani T. Chirality-dependent environmental effects in photoluminescence of single-walled carbon nanotubes. Phys Rev B - Condens Matter Mater Phys. 2006;73(23):1–5.
118. Chen Z, Appenzeller J, Knoch J, Lin Y, Avouris P. The role of metal / nanotube contact in the performance of carbon nanotube field-effect transistors. Nano Lett. 2005;5(7):1497–502.
119. Marquardt CW. Elektrolumineszenz organischer Moleküle nach Kontaktierung mit Kohlenstoff-Nanoröhren. Universität Karlsruhe. 2009.
120. Klein LJ, Hamann HF, Au Y-Y, Ingvarsson S. Coherence properties of infrared thermal emission from heated metallic nanowires. Appl Phys Lett. 2008;92(21):213102.
121. Kim YD, Kim H, Cho Y, Ryoo JH, Park C-H, Kim P, et al. Bright visible light emission from graphene. Nat Nanotechnol. 2015;10(8):676–81.
122. Born M, Wolf E. Principles of Optics. Cambridge University Press, USA. 2009.

123. Liew KM, Wong CH, He XQ, Tan MJ.
Thermal stability of single and multi-walled carbon nanotubes.
Phys Rev B - Condens Matter Mater Phys. 2005;71(7):1–6.
124. Mehta CL. Coherence-time and effective bandwidth of blackbody radiation.
Nuovo Cim. 1963;28(2):401–8.
125. Pfeiffer MHP, Stürzl N, Marquardt CW, Engel M, Dehm S, Hennrich F, et al.
Electroluminescence from chirality-sorted (9,7)- semiconducting carbon nanotube devices. Opt Express. 2011;19:1184–9.
126. Mueller T, Xia F, Avouris P. Graphene photodetectors for high-speed optical communications. Nat Photonics. 2010;4:20.
127. Yu D, Wang S, Ye L, Li W, Zhang Z, Chen Y, et al. Electroluminescence from serpentine carbon nanotube based light-emitting diodes on quartz.
Small. 2014;10(6):1050–6.
128. Melchiorri M, Daldosso N, Sbrana F, Pavesi L, Pucker G, Kompocholis C, et al.
Propagation losses of silicon nitride waveguides in the near-infrared range.
Appl Phys Lett. 2005;86(12):121111.
129. Fujiwara M, Toubaru K, Noda T, Zhao H-Q, Takeuchi S. Highly efficient coupling of photons from nanoemitters into single-mode optical fibers.
Nano Lett. 2011;11(10):4362–5.
130. Eggleston MS, Wu MC. Efficient coupling of an antenna-enhanced nanoLED into an integrated InP waveguide. Nano Lett. 2015;15(5):3329–33.
131. Taillaert D, Bienstman P, Baets R. Compact efficient broadband grating coupler for silicon-on-insulator waveguides. Opt Lett. 2004;29(23):2749–51.
132. Liu J-M. Photonic Devices. Cambridge University; 2009.
133. Hansperger R. Integrated optics: Theory and technology. Springer; 2009.
134. Waldausl R, Schnabel B, Kley E, Brauer A. Efficient focusing polymer waveguide grating couplers. Electron Lett. 1997;33(7):623–4.
135. Horst F, Green WMJ, Assefa S, Shank SM, Vlasov Y a., Offrein BJ. Cascaded Mach-Zehnder wavelength filters in silicon photonics for low loss and flat pass-band WDM (de-) multiplexing. Opt Express. 2013;21(10):11652–8.
136. Foresi JS, Villeneuve PR, Ferrera J, Thoen ER, Steinmeyer G, Fan S, et al.
Photonic-bandgap microcavities in optical waveguides.
Nature. 1997;390(6656):143–5.

137. Akahane Y, Asano T, Song B. High-Q photonic nanocavity in a two-dimensional photonic crystal. Nature. 2003;425(October):944.
138. Gérard J, Sermage B, Gayral B, Legrand B, Costard E, Thierry-Mieg V. Enhanced spontaneous emission by quantum boxes in a monolithic optical microcavity. Phys Rev Lett. 1998;81(5):1110–3.
139. Agio M, Cano DM. Nano-optics: The Purcell factor of nanoresonators. Nat Photonics. 2013;7(9):674–5.
140. Barth M, Nüsse N, Löchel B, Benson O. Controlled coupling of a single-diamond nanocrystal to a photonic crystal cavity. Opt Lett. 2009;34(7):1108–10.
141. Yoshie T, Scherer A, Hendrickson J, Khitrova G, Gibbs HM, Rupper G, et al. Vacuum Rabi splitting with a single quantum dot in a photonic crystal nanocavity. Nature. 2004;432(7014):200–3.
142. Lund-Hansen T, Stobbe S, Julsgaard B, Thyrrestrup H, Sünner T, Kamp M, et al. Experimental realization of highly efficient broadband coupling of single quantum dots to a photonic crystal waveguide. Phys Rev Lett. 2008;101(11):1–4.
143. Lee K, Chen X, Eghlidi H, Renn A, Gotzinger S, Sandoghdar V. A planar dielectric antenna for directional single-photon emission and near-unity collection efficiency.
Conf Lasers Electro-Optics Eur 12th Eur Quantum Electron . 2011;5:166–9.
144. Quan Q, Deotare PB, Loncar M. Photonic crystal nanobeam cavity strongly coupled to the feeding waveguide. Appl Phys Lett. 2010;96(20):1–4.
145. Quan Q, Loncar M. Deterministic design of wavelength scale, ultra-high Q photonic crystal nanobeam cavities. Opt Express. 2011;19(19):18529–42.
146. Khan M, Babinec T, McCutcheon MW, Deotare P, Loncar M. Fabrication and characterization of high-quality-factor silicon nitride nanobeam cavities. Opt Lett. 2011;36(3):421–3.
147. Oskooi A, Johnson SG. Advances in FDTD computational electrodynamics: Photonics and nanotechnology.
Taflove A, Oskooi A, Johnson SG, Norwood: MA: Artech House; 2013.
148. Mori T, Yamauchi Y, Honda S, Maki H. An electrically driven, ultrahigh−speed, on−chip light emitter based on carbon nanotubes.
Nano Lett. 2014;14(6):3277−83.

149. Pop E, Mann DA, Goodson KE, Dai H. Electrical and thermal transport in metallic single-wall carbon nanotubes on insulating substrates. J Appl Phys. 2007;101(9):093710.
150. Reich S, Dworzak M, Hoffmann A, Thomsen C, Strano MS. Excited-state carrier lifetime in single-walled carbon nanotubes. Phys Rev B. 2005;71(3):033402.
151. Wang F, Dukovic G, Brus LE, Heinz TF. Time-resolved fluorescence of carbon nanotubes and its implication for radiative lifetimes. Phys Rev Lett. 2004;92(17):177401–1.
152. Perebeinos V, Tersoff J, Avouris P. Radiative lifetime of excitons in carbon nanotubes. Nano Lett. 2005;5(12):2495–9.
153. Jiang M, Kumamoto Y, Ishii A, Yoshida M, Shimada T, Kato YK. Gate-controlled generation of optical pulse trains using individual carbon nanotubes. Nat Commun. 2015;6:6335.
154. Yu D, Dai L. Voltage-induced incandescent light emission from large-area graphene films. Appl Phys Lett. 2010;96(14).
155. Marquardt CW, Dehm S, Vijayaraghavan A, Blatt S, Hennrich F, Krupke R. Reversible metal-insulator transitions in metallic single-walled carbon nanotubes. Nano Lett. 2008;8(9):2767–72.
156. Parzefall M, Bharadwaj P, Jain A, Taniguchi T, Watanabe K, Novotny L. Antenna-coupled photon emission from hexagonal boron nitride tunnel junctions. Nat Nanotechnol. 2015;10(12):1058–63.
157. Takahashi Y, Hagino H, Tanaka Y, Asano T, Noda S. High-Q photonic nanocavity with a 2-ns photon lifetime. Conf Quantum Electron Laser Sci - Tech Dig Ser. 2008;15(25):17206–13.
158. Upham J, Tanaka Y, Asano T, Noda S. Dynamic increase and decrease of photonic crystal nanocavity Q factors for optical pulse control. Opt Express. 2008;16(26):21721–30.
159. Goltsman GN, Okunev O, Chulkova G, Lipatov A, Semenov A, Smirnov K, et al. Picosecond superconducting single-photon optical detector. Appl Phys Lett. 2001;79(6):705–7.
160. Pernice WHP, Schuck C, Minaeva O, Li M, Goltsman GN, Sergienko AV, et al. High-speed and high-efficiency travelling wave single-photon detectors embedded in nanophotonic circuits. Nat Commun. 2012;3:1325.

161. Kahl O, Ferrari S, Kovalyuk V, Goltsman GN, Korneev A, Pernice WHP. Waveguide integrated superconducting single-photon detectors with high internal quantum efficiency at telecom wavelengths. Sci Rep. 2015;5:10941.
162. Ishii A, Yoshida M, Kato YK. Exciton diffusion, end quenching, and exciton-exciton annihilation in individual air-suspended carbon nanotubes. Phys Rev B. 2015;91(12):125427.
163. Miyauchi Y, Iwamura M, Mouri S, Kawazoe T, Ohtsu M, Matsuda K. Brightening of excitons in carbon nanotubes on dimensionality modification. Nat Photonics. 2013;7(9):715–9.
164. Zhang F, Hou P-X, Liu C, Wang B-W, Jiang H, Chen M-L, et al. Growth of semiconducting single-wall carbon nanotubes with a narrow band-gap distribution. Nat Commun. 2016;7:11160.
165. Franklin AD, Chen Z. Length scaling of carbon nanotube transistors. Nat Nanotechnol. 2010;5(12):858–62.
166. Cao C, Andrews JB, Kumar A, Franklin AD. Improving contact interfaces in fully printed carbon nanotube thin-film transistors. ACS Nano. 2016;10(15):5221-9.
167. Piao Y, Meany B, Powell LR, Valley N, Kwon H, Schatz GC, et al. Brightening of carbon nanotube photoluminescence through the incorporation of sp3 defects. Nat Chem. 2013;5(10):840–5.
168. Waldhäusl R, Schnabel B, Dannberg P, Kley EB, Bräuer A, Karthe W. Efficient coupling into polymer waveguides by gratings. Appl Opt. 1997;36(36):9383–90.
169. Bååk T. Silicon oxynitride; a material for GRIN optics. Appl Opt. 1982;21(6):1069.
170. Saleh BEA, Teich MC. Fundamentals of Photonics, 2nd Edition. Wiley. 2007.

Curriculum Vitae

Personal information

Name	Felix Pyatkov
Date of birth	24.12.1986
Citizenship	German

Education

04/2012 – 11/2016	Promotion:	TU Darmstadt "Waveguide-integrated electrically driven light-emitting carbon nanotubes" Dean Prize for Excellence in Research Supervisor: Prof. Dr. Ralph Krupke
10/2009 – 02/2012	Master of Science: Master thesis:	Physics, RWTH Aachen University „Inverstigation of charge transfer in oligopeptides on the level of individual molecules“
10/2006 – 09/2009	Bachelor of Science: Bachelor thesis:	Physics, RWTH Aachen University „X-ray diffraction from nanocomposite materials“
09/2005 – 06/2006	Studienkolleg:	RWTH Aachen University
09/1998 – 06/2004	Secondary school:	Gymnasium №12, Lipetsk, Russia

Professional experience

from 04/2012	Research assistant at Institute of Nanotechnology Karlsruhe Institute of Technology
11/2010 – 12/2011	Scientific assistant at Institute of Complex Systems (ICS-8) Jülich Research Centre
11/2009 – 08/2010	Scientific assistant at 2nd Institute of Physics B RWTH Aachen University

List of Publications

Publications in the course of this work

F. Pyatkov*, S. Khasminskaya*, V. Kovalyuk, F. Hennrich, M. M. Kappes, G. Goltsman, W. H. P. Pernice, R. Krupke,
Sub-Nanosecond Light Pulse Generation with Waveguide-Coupled Carbon Nanotube Transducers,
Beilstein Journal of Nanotechnology **8**, 38-44 (2017).

F. Pyatkov*, V. Fütterling*, S. Khasminskaya, B. Flavel, F. Hennrich, M. M. Kappes, R. Krupke, W. H. P. Pernice,
Cavity Enhanced Light Emission from Electrically Driven Carbon Nanotubes,
Nature Photonics **10**, 420–427 (2016).

S. Khasminskaya*, **F. Pyatkov***, K. Slowik, S. Ferrari, O. Kahl, V. Kovalyuk, P. Rath, A. Vetter, F. Hennrich, M. M. Kappes, G. Gol'tsman, A. Korneev, C. Rockstuhl, R. Krupke, W. H. P. Pernice,
Fully Integrated Quantum Photonic Circuit with an Electrically Driven Light Source,
Nature Photonics **10**, 727–732 (2016).

R. Fechner, **F. Pyatkov**, S. Khasminskaya, B. S. Flavel, R. Krupke, W. H. P. Pernice,
Directional Coupler with Integrated Carbon Nanotube Incandescent Light Emitters,
Optics Express **24**, 966–974 (2016).

A. Riaz, **F. Pyatkov**, A. Asiful, S. Dehm, A. Felten, V. S. K. Chakravadhanula, B. S. Flavel, C. Kübel, U. Lemmer, R. Krupke,
Light Emission, Light Detection and Strain Sensing with Nanocrystalline Graphene,
Nanotechnology **26**, 325202 (2015).

S. Khasminskaya*, **F. Pyatkov***, B. S. Flavel, W. H. P. Pernice, R. Krupke,
Waveguide-Integrated Light-Emitting Carbon Nanotubes,
Advanced Materials **26**, 3465–3472 (2014).

W. Li, **F. Pyatkov**, S. Dehm, B. S. Flavel, R. Krupke,
Deposition of Semiconducting Single-Walled Carbon Nanotubes Using Light-Assisted Dielectrophoresis,
Physica Status Solidi (b) **251**, 2475-2479 (2014).

Other publications

D. Xiang, **F. Pyatkov**, F. Schröper, A. Offenhäusser, Y. Zhang, D. Mayer,
Molecular Junctions Bridged by Metal Ion Complexes,
Chem. Eur. J., **17**, 13166-13169 (2011).

D. Xiang, Y. Zhang, **F. Pyatkov**, A. Offenhäusser, D. Mayer,
Gap Size Dependent Transition from Direct Tunneling to Field Emission in Single Molecule Junctions,
Chemical Communications **47**, 4760-4762 (2011).

* these authors contributed equally to this work.

List of Conferences

International Symposium on Carbon Nanotube 2016 – CNT25
Tokyo (Japan), November 2016
Oral presentation: *"Fully Integrated Quantum Photonic Circuit with an Electrically Driven CNT Light Source"*

International Conference on the Science and Application of Nanotubes (NT16)
Vienna (Austria), August 2016
Poster presentation: *"Sub-Nanosecond Light Pulse Generation with Waveguide-Coupled Carbon Nanotubes Transducers"*

Statussymposium on Macroscopic Functional Systems (Volkswagen Foundation)
Hannover (Germany), May 2016
Poster presentation: *"Sub-Nanosecond Light Pulse Generation with Waveguide-Coupled Carbon Nanotubes Transducers"*

International Winterschool on Electronic Properties of Novel Materials (IWEPNM)
Kirchberg (Austria), February 2016
Poster presentation: *"Sub-Nanosecond Light Pulse Generation with Waveguide-Coupled Carbon Nanotubes Transducers"*

International Conference on the Science and Application of Nanotubes (NT15)
Nagoya (Japan), June-July 2015
Oral and poster presentation: *"Waveguide-Integrated Light-Emitting Carbon Nanotubes"*
Winner of Poster Award

International Workshop on Nanotube Optics and Nanospectroscopy (WONTON),
Kloster Banz (Germany), June 2015
Poster presentation: *"Waveguide-Integrated Light-Emitting Carbon Nanotubes"*
Winner of Poster Award

Graphene and Nanotubes: Science and Applications (GDR-I GNT)
Strasbourg (France), September 2014
Oral presentation: *"Waveguide-Integrated Light-Emitting Carbon Nanotubes"*

European Materials Research Society (E-MRS) Fall Meeting
Warsaw (Poland), September 2014
Oral presentation: *"Graphene-Based Light-Emitting Nanostructures"*

European Materials Research Society (E-MRS) Fall Meeting
Warsaw (Poland), September 2014
Oral presentation: *"Waveguide-Integrated Light-Emitting Carbon Nanotubes"*

Summer School of German-Japanese Universities Alliance (HeKKSaGOn)
Karlsruhe (Germany), September 2014
Poster presentation: *"Waveguide-Integrated Light-Emitting Carbon Nanotubes"*

International Winterschool on Electronic Properties of Novel Materials (IWEPNM)
Kirchberg (Austria), March 2014
Poster presentation: *"Waveguide-Integrated Light-Emitting Carbon Nanotubes"*

Acknowledgements

First of all, I would like to thank my supervisor Professor Ralph Krupke for the offer to work on this exciting topic, for his support and guidance during my PhD. He helped me a lot with the understanding and analysis of my results. Thank you, Ralph, for all the discussions and inspiration!

I am grateful to Dr. Benjamin S. Flavel and Dr. Frank Hennrich for preparation of sorted CNT suspension and for their support in writing our scientific papers.

Results shown in this thesis would not have been possible without the close collaboration with the Integrated Quantum Optics and Optomechanics group of Professor Wolfram H. P. Pernice, at the Center for Nanotechnology (CeNTech), Physikalisches Institut, University of Münster. I thank Wolfram for the great cooperation we have had with his group on planning, producing and characterization of WINS-devices. In particular, Wolfram's PhD student Svetlana Khasminskaya that has become a very good friend of mine was helpful, competent and dependable co-worker during all the years of my PhD. We spent great time together in and out of the lab!

I thank master students Imteaz Md. Alamgir, Randy Fechner, Valentin Fütterling for very productive teamwork on electroluminescent CNTs, as well as on CNT integrated in directional couplers and photonic crystals, respectively.

Thanks to Simone Dehm and Stefan Kolenda for all the technical help in the laboratory and with device fabrication. Many thanks to Asiful Alam, Vadim Kovalyuk, Wenshan Li and Adnan Md. Riaz helping me with the sample characterization. I am also very thankful to Dr. Romain Danneau, Dr. Benjamin S. Flavel and Asiful Alam for proofreading of this thesis.

I am grateful to the members of our research unit and other friendly co-workers for their help and cheerful atmosphere during my PhD: Dr. Christian Benz, Renjun Du, Dr. Michael Engel, Dr. Alexandre Felten, Simone Ferrari, Marco A. Giambra, Nico Gruhler, Daniel Gürlich, Ihteaz Hossain, Dr. Oliver Kahl, Murtaza Ali Khan, Alexandra Kirchhoff, Rainer Kraft, Dr. Sergei Lebedkin, Dr. Jens Mohrmann, Dr. Matti Oron-Carl,

Anna Ovvyan, Martin Pfeiffer, Moritz Pfohl, Patrik Rath, Pranauv B. Selvasundaram, Matthias Stegmaier, Dr. Cornelius Thiele, Ailine Trometer, Dr. Daniel Tune and Rana Yekani.

I wish to acknowledge the financial support from the DFG – Center for Functional Nanostructures (CFN) and Volkswagen Foundation.

At last I would like to thank all my friends outside the institute, my student organization "RuSKa" and my big family, supported me all the time throughout my studies. I dedicate this thesis to my wife, Elena, for her endless love, support and inspiration.